© Copyright 2021

Paul Nguyen

Micro-focus ARPES of operating 2D devices

Paul Nguyen

A dissertation

submitted in partial fulfillment of the

requirements for the degree of

Doctor of Philosophy

University of Washington

2021

Reading Committee:

David H. Cobden, Chair

Xiaodong Xu

Lukasz Fidkowski

Program Authorized to Offer Degree:

Physics

University of Washington

Abstract

Micro-focus ARPES of operating 2D devices

Paul Van Nguyen

Chair of the Supervisory Committee:
Professor David H. Cobden
Department of Physics

With the advent of two-dimensional (2D) materials came a library of new systems that not only individually host novel states of matter but are naturally suited to being stacked into heterostructures – a virtually limitless space of possible geometries for study. The incorporation of electrical contacts transforms these heterostructures into 2D electrical devices wherein electronic behavior can be simultaneously probed and tuned by locally applied electric fields. This thesis presents pioneering studies of the electronic band structure in such devices *in-operando* using sub-micrometer angle-resolved photoemission spectroscopy (μ-ARPES), a surface-sensitive technique already perfectly suited to probe the electronic states in these 2D systems made more powerful by the addition of *in-situ* control of carrier densities and local electric fields.

Following a brief background review of 2D materials and ARPES, I will show how with careful sample design and preparation μ-ARPES was applied for the first time to artificially stacked structures of prototypical 2D materials, graphene and atomically thin semiconducting transition metal dichalcogenides (TMD). From there, I will demonstrate how in-situ control of an electrostatic back gate voltage alleviates a fundamental limitation of ARPES as a probe of only occupied states and study the electronic landscape in two-terminal TMD field-effect transistor devices as a function of applied electric field and doping. I will then take a detour to discuss the possible effects of relative crystallographic alignments in heterostructures on the μ-ARPES spectra, which ultimately stem from a combination of moiré effects and electron diffraction. I will then turn to gated devices with monolayer WTe_2 and study the bands as a function of doping and temperature to shed light on the of its unusual insulating state below 100K which interplays with topologically insulating and superconducting behavior recently shown in transport measurement. Finally, I will conclude with a brief discussion of the outlook for μ-ARPES of 2D materials in devices under operation.

TABLE OF CONTENTS

LIST OF FIGURES

LIST OF TABLES

ACKNOWLEDGEMENTS

Before and above all else, my gratitude must go to my loving parents. Without their support and infinite patience with my seemingly interminable journey I would certainly not have made it. I remember fondly the countless times my father, with his long winding life's worth of stories and experiences, helped take my mind off of troubling times, or gave me a new perspective on a problem at hand. Admittedly our worldviews differ drastically - understandably so as we are products of so incomparable of environments. Nonetheless I'd like to think our disagreements have helped us both better understand our respective generations. Our conversations will stay with me always and I can only hope that I live half as interesting a life as his. Certainly I am motivated to try to make the world less *interesting* than the one he and my mother had to survive. Speaking of mom, her utterly unconditional love has been the most important thing motivating me all these years. Her down to earth perspective and pure concern for my wellbeing have crucially moderated my sometimes reckless work/eating/living habits. I shudder to think of how many (more) gray hairs I would be facing without her reminders to take care of myself.

Next to thank must of course my advisor, Prof. David Cobden. I've known Dave (or "Hey, You", as he once advised us to call him) for ten years now, and I can't begin to imagine how my graduate career might have gone with anyone else. His patience, curiosity, humor, and unflinching confidence in the physics he loves have made for such a singular experience that I hate to imagine leaving the lab or the sort of work we do. One only hopes I have returned the favor, though fortunately I have the next many months as a post-doc to make up any remaining balance. In that time, I would be so lucky as to also pick up just a bit of his intuition and perspective on the state of physics and academics.

Naturally I cannot discuss the impact Dave has had on me without mentioning the group that he maintained throughout these years. Even as a dejected, multiply-rejected post-Bachelor volunteer in the lab, the grad students and undergrads alike were all just so supportive of me and helped me complete the research opportunities/experiences I needed to fill out my next attempt to get into grad school. For making bright what could have easily been the darkest year of my life I owe so much to (in no particular order) the then-undergrads Joe Varnum Finney, Denise Schmitz, Jon Hag, and Frank McKay; and then-grad students Jae Park and Serkan Kasirga. Similar debts I also owe the other grad students in the lab at the time, Boris Dyzubenko and Zaiyao Fei, who would become my colleagues and mentors when I did make it to grad school. Other colleagues joined along the way: Joshua Kahn, Bosong Sun, Wenjin Zhao, Elliott Runburg, Arnab Manna, Eric Lester, post-doc Tauno Palomaki, and visiting Professor Jennifer Heath. All together their daily company made the lab a productive yet relaxed place to come every day. I can't say how important it was for my sanity that we could always turn to each other to chat as much about physics as about our nonacademic interests and concerns. Though many of us may not see each other again for a long time, I think I can speak for everyone when saying that we will be friends always. Undoubtedly for all involved, a particular bond of trust was formed over a certain fishy, Rick's-y dinner that will never be broken. I also must acknowledge the couple of undergraduates I've had the privilege of mentoring, whose relatively youthful curiosity helped me better appreciate my own journey as a physicist.

Outside of our well-lit enclave up on the third floor are naturally the innumerable other students in the department that played irreplaceable roles in my time as a graduate student. Be it in the lab, in their labs, or even outside over a drink/board game, chitchatting with them has been the source of just so much inspiration. To name just a few, these wonderful folks included

Genevieve Clark (my CVD-commiserator); Kyle Seyler, Pasqual Rivera, Nathan Wilson, Kyle Hwangbo and Heonjoon Park (my local ARPES-coconspirators); as well as Marie Scott, Sanfeng Wu, and Essance Ray (sometimes reluctant board gamers).

It can't be missed that all of these other-lab-people are from the Xu lab. Indeed, it was a distinct boon to work so closely with a lab full of such talented and driven people. It is unmistakable that the group reflects its advisor, Prof. Xiaodong Xu. As a coauthor on all of my academic works, Xiaodong's drive and perspective have helped me elevate my output in so many ways I cannot begin to list. Another PI who shares blame/credit for essentially all of my academic efforts is Prof. Neil Wilson at the University of Warwick. Also once a student of Dave, Neil has a particular view of ARPES and physics itself that has proven central to the works discussed in this thesis. Without a doubt the time he and his students, Natalie Teutsch, Xue Xia, Abigail Graham, and James Marsden, have spent at synchrotrons measuring the meagre devices I put together has generated up my greatest debt averaged over the last seven years. Similar debt is owed to Cheng Chen, whose help over the last few years helped us finally make progress with WTe_2.

Of course, I must thank the rest of my committee: Lukasz Fidkowski, Jason Detweiler, and Ting Cao. Lukasz and Jason have just been such wonderful younger members of our department and I can't thank either of them enough for helping make our small community a better place with their presence. As for Ting, not only did he heroically accept a last minute appointment to my committee as a GSR, but his genuine interest in my project has been a highlight of my exams. I hope we can continue talking and collaborating in the future.

Lastly, are the people of Seattle itself where I have spent nearly my entire life. The folks I've had the honor of growing up with made me the person I am today. I cherish every memory, every moment spent with them. Hopefully, we will make more memories together in the future.

DEDICATION

To my parents, who have lived many lives so that I could live mine.

Chapter 1. INTRODUCTION

The reduced dimensionality of van der Waals materials exfoliated down to their two-dimensional (2D) limit presents a deep well for novel physics and technological applications. Stacking these 2D crystals into van der Waals-bonded heterostructures multiplies the already wide (and ever-growing) variety of available *individual* material properties to generate a virtually limitless space of possible engineered electronic environments exhibiting emergent *hybridized* electronic behavior. Due to their 2D nature, atomically thin samples can be affected throughout by the application of local electric fields; this presents a powerful parameter for tuning the electronic properties of our 2D systems. The ability, then, to directly monitor the states of electrons in such structures, especially whilst e.g., applying a local electrostatic gate voltage, could transform the understanding of underlying physics and device function. This dissertation will show that such direct study of the electronic bands is possible using sub-micrometer angle-resolved photoemission spectroscopy via discussion of pioneering experiments performed at state-of-the-art synchrotron-based beamlines.

The rest of this chapter is an introduction to ARPES, reviewing some of its fundamental theory, applications, and the state of high-spatial resolution ARPES, as well as a primer on 2D materials and 2D fabrication. Along the way, we will review some experimental techniques that complement ARPES and are referenced later in this thesis, such as atomic force microscopy (AFM), photoluminescence spectroscopy (PL), and piezo-response microscopy.

In the following chapter, we will show how with careful sample design and preparation, μ-ARPES can produce high resolution spectra from artificially stacked heterostructures of graphene and TMDs. From these spectra we can extract key band parameters, determine the evolution of the

valence bands with decreasing thickness down to a TMD monolayer (ML), and reveal unexpectedly strong band hybridization in crystalographically-aligned TMD heterobilayers, which we show is the result of commensuration.

We then review the μ-ARPES of TMDs in operating two-terminal devices, wherein a longstanding limitation of ARPES (which probes only occupied states) is bypassed via the in-situ application of voltage to a graphitic back gate to controllably and reversibly populate conduction band states and thereby allow direct measurement of the band gaps of these semiconductors. Notably, this study demonstrated doping-dependent band gap renormalization in monolayer WSe_2, indisputably confirms its direct-gap nature, and revealed field-dependent band alignment shifts at the contact region in these effectively field-effect transistors between the semiconducting TMDs and its overlapping graphene grounding electrode.

Next, we will discuss ongoing μ-ARPES study of heterostructures where the crystallographic twist between certain proximal layers produces folded replica bands in the apparent spectra. In the case where the twist is between monolayer boron nitride and a TMD, we will argue that the band replication is the result of trivial electron diffraction. In contrast, we will argue that in the case of graphene on a TMD (or a TMD heterostructure), the observed folding is the result of moiré effects.

In the final chapters, we will show μ-ARPES measurements of the bands in monolayer WTe_2 as a function of both electrostatic doping and temperature to try to shed some light on the nature of its unusual insulating state below 100K which interplays with topologically insulating and superconducting behavior recently shown in transport measurements. We will conclude with a brief discussion of the outlook for μ-ARPES of 2D materials in devices under operation.

1.1 Angle Resolved Photoemission Spectroscopy

Angle-resolved photoemission spectroscopy, or ARPES, has its roots in the photoelectric effect: the ejection of electrons from the surface of a material under illumination by light of sufficient frequency with the electron energies independent of the intensity of the light. It was for his theoretical explanation of this phenomenon – that light is quantized into photons each carrying a unit of energy that must exceed the minimum energy binding electrons to a given material to free an electron – that Einstein won his Nobel prize in 1921. Illumination by photons of energy greater than this minimum generates an excitation energy-dependent distribution of energies of the photoemitted electrons. Such photoemission spectroscopy (PES) can uniquely identify the material under study. This is of course a direct application of energy conservation and lies at the core of such techniques as X-ray photoelectron spectroscopy, two-photon photoelectron spectroscopy, and of course ARPES. As we shall see below, ARPES adds momentum conservation to the equation, allowing direct mapping of the band structure in a crystalline solid.

1.1.1 *Fundamentals*

The theory behind ARPES naturally starts at the basic principle from solid state physics that an electron subject to a periodic potential, say from a crystalline lattice, has Bloch states as eigensolutions to Schrodinger's equation. These Bloch states are each the product of a plane wave, $e^{i\,\boldsymbol{k}\cdot\boldsymbol{r}}$, with a function with the same period as the potential. The plane wave component introduces the wavevector $\boldsymbol{k}$ which is reciprocal to the real space position. Any value of $\boldsymbol{k}$ is allowed for these stationary states and so the space of eigenstates spans a continuum of allowed quantum numbers $\boldsymbol{k}$. For a given $\boldsymbol{k}$ there will be a discrete, indexable spectrum of solutions and eigenenergies. To each index n is a corresponding continuum of energy eigenvalues $E_{\boldsymbol{n},\boldsymbol{k}}$; this forms a continuous

band of states in $E - \boldsymbol{k}$ space. Thus, the full space of solutions is the spectrum of these electronic bands: the band structure.

Naïve insertion of the Bloch states into Schrodinger's equation reveals that $\hbar\boldsymbol{k}$ acts as a momentum, and for this $\boldsymbol{k}$ can be referred to as crystal momentum. The real-space periodic lattice has an equivalent reciprocal lattice, and the Bragg law of diffraction for plane waves on a periodic lattice forces $\boldsymbol{k}$ to be only uniquely defined within a primitive cell of the reciprocal lattice, conventionally taken to be a Brillouin zone. The first Brillouin zone is the Voronoi cell about the origin of the reciprocal space. A value beyond this range is equivalent to one mapped back to the first Brillouin zone by a linear combination of the reciprocal lattice vectors.

A way to think of how bands are formed is in terms of hybridization between the orbitals of the lattice's constituent atoms. As similar orbitals overlap, they hybridize and split apart in energy to lift the degeneracy. In the continuum limit of an infinite crystal with infinitely many copies of a given orbital, this hybridization generates a continuum of hybridized states. Core electron states are tightly bound to the atoms, overlapping little and thus producing nearly nondispersive bands referred to as core levels.

These core levels are, however, still sensitive to their chemical environments and, for example, can distinguish possible oxidation states[1–3]. The number of states in a band is equal to the number of orbitals hybridizing to produce it, i.e., twice (for spin-degeneracy) the number of primitive cells in the lattice. As fermions, the electrons in the crystal at $T = 0$ then fill these bands up starting from the lowest energy states (the core levels). The energy of the last filled state (relative to that of the first) is the Fermi energy E_{F}[*].

[*] While this nomenclature is strictly for zero temperature, it is often used interchangeably with the analogous energy at finite temperature, the energy of the Fermi *level.* This work will follow the latter convention.

The band structure is important as it determines fundamental properties of a material and the electrons in it. For example, in a metal the Fermi energy lies in the middle of a band; in an insulator or semiconductor it lies in between bands. Additionally, the curvature at each point along a band defines the effective mass of the electrons occupying those states, thus affecting the response of those electrons to say, an applied electric potential. In a semiconductor, the gap – the energy difference between the highest energy filled state (in the valence band) and the lowest energy empty state (in the conduction band) – determines its conductivity (if undoped), and the energy at which it can absorb or emit light in an LED/photovoltaic. The efficiency of such light absorption/emission is greatly enhanced if the gap is direct, i.e., the two states have the same $\boldsymbol{k}$. The bands themselves may carry topologically nontrivial properties, with consequences we will briefly describe later in this thesis. This is a woefully incomplete list of the consequences of the band structure, and an understanding of it in a material under study is of manifest utility. In the following subsection we will review how ARPES provides a uniquely powerful tool for directly probing band structure.

1.1.2 *ARPES: kinematics, application, and interpretation*

Consider an electron of binding energy E_{B} below the Fermi energy, which is itself some energy W below the energy of a free electron at rest (the work function). Absorption of a photon of frequency ν produces a photoelectron of kinetic energy E_{kin} that satisfies energy conservation:

$$E_{\mathrm{kin}} = h\nu - W - E_{\mathrm{B}}. \tag{1.1}$$

This is provided that the electron is not scattered before leaving the solid or afterwards by gas molecules. For this (and another) reason, high resolution (AR)PES must be done in ultra-high vacuum (UHV).

Of course, in-plane momentum must also be conserved. The photoemitted electron escapes the material at some polar and azimuthal angles, θ and ϕ, relative to the sample surface, thereby carrying away some finite in-plane momentum $\boldsymbol{p}_{||}$. The original electron state had some in-plane crystal momentum $\boldsymbol{k}_{||}$ which as previously discussed is equivalent to ordinary momentum save for only being uniquely defined within a Brillouin zone. Typical ARPES photon energies involved are < 200 eV; such photons have total momenta < 0.1 Å^{-1}, which is negligible. Thus, our momentum conservation equation reads:

$$\boldsymbol{k}_{||} = \frac{1}{\hbar}\boldsymbol{p}_{||} \cong \frac{1}{\hbar}\sqrt{2m_e E_{\text{kin}}}\,(\sin\theta\cos\phi\,, \sin\theta\sin\phi). \tag{1.2}$$

Note that the out-of-plane component of momentum $\boldsymbol{k}_{\perp}$ is not conserved as there is a nontrivial, abrupt potential change (partly W) at/away from the surface, though it is possible to approximate by estimating the so-called inner potential[4]. From this one can assess the 2D (surface-bound) nature of a band which should not disperse[5,6].

Thusly we have described the kinematics of ARPES and how the addition of angle-resolution allows the inference of the original electron energy and momenta in a solid of interest, schematically shown in Figure 1.1. Energy resolution is most commonly achieved by using a hemispherical deflection analyzer (Figure 1.3**A**), a hemispherical capacitor which electrostatically

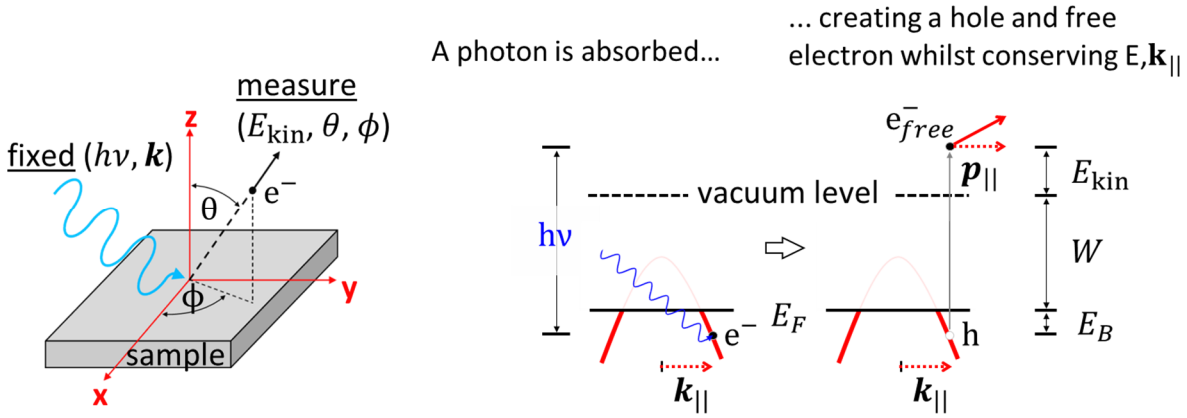

Figure 1.1. Kinematics of photoemission.

deflects electrons entering through a narrow aperture according to their E_{kin}. Those electrons not deflected into either hemisphere (i.e., within a narrow range of energies centered on the pass energy, E_{pass}) reach the other side and can be counted by an electron detector, or 1D array of detectors.

The addition of electron optics ahead of the aperture serves two primary roles: electrostatic retardation of the electrons entering the analyzer and focusing of the photoelectrons (Figure 1.3**B**). The latter is clearly to maximize angular resolution. The former allows tuning of the E_{kin} that are detected for a fixed E_{pass}. Additionally, it can be shown[7] that the energy resolution (read: uncertainty) of a hemispherical detector of average radius R_0 is given by

$$\Delta E = E_{\text{pass}}(\omega/R_0 + \alpha^2/4), \text{ where } \omega\text{: slit width, and } \alpha\text{: acceptance angle.} \qquad (1.3)$$

In principle then, energy resolution improves as E_{pass} is decreased. As the E_{kin} of the photoemitted electrons depends on the excitation energy (which should be tuned to maximize photoemission intensity and angular resolution, as will be discussed below), this can only directly set to equal E_{pass} by means of the electron optics. In practice, however, increasing either E_{pass} or

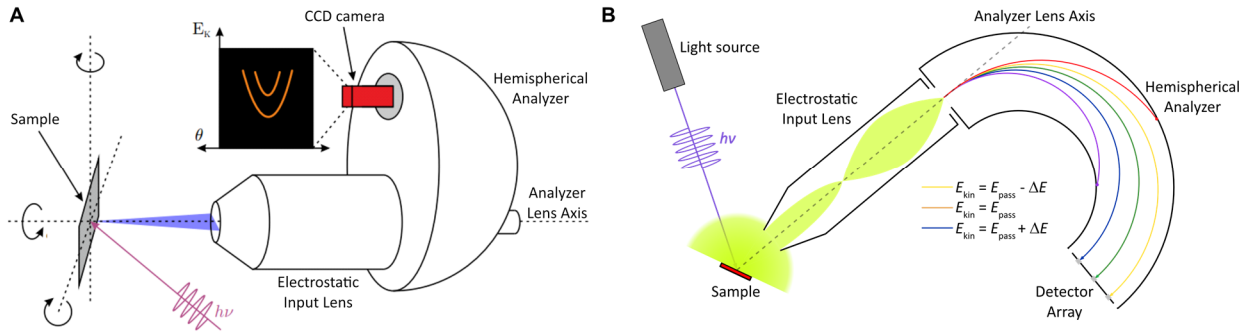

Figure 1.2. Schematics of ARPES measurement. **A**, schematic of a typical ARPES measurement geometry. **B**, cross-section of **A** showing cloud of photoemission from the sample (yellow) being collected and focused by electrostatic lenses. The electrons entering the hemispherical analyzer are split up by their energies (color coded). Adapted from J. Mudd, thesis (2014), University of Warwick.

ω increases the number of electrons reaching the detector and thereby can improve the signal-to-noise ratio. The latter does this by allowing more electrons to enter, the former by widening the energy window of electrons reaching the end of the analyzer, which scales as $E_{\text{pass}}/(E_{\text{kin}} - E_{\text{pass}})$. As the analyzer has finite spatial width, this maps a larger range of electron energies to each unit length of the detector(s). This has the added benefit of widening the range of energies over which a 1D array of detectors can simultaneously measure.

The simplest approach to angle resolution involves rotation of an electron spectrometer with small acceptance angle about the sample to capture spectra at a collection of angles and so sample the band structure along an interesting line in momentum space[8], or even over a large volume of $E - \boldsymbol{k}$ space by sampling over the entire hemisphere[9]. A more modern approach is made more time efficient by measuring a range of energies and angles simultaneously in a single positioning of the detector, so-called "multidimensional acquisition". This is commonly achieved by replacing the originally narrow angular aperture on the analyzer with a well-defined entrance slit which we will take to be vertical for ease of discussion. Electrons of appropriate energies now reach the detector displaced along two different axes by their energies and entrant angles. A 2D electron detector (e.g. a microchannel plate detector on a phosphor screen and CCD) can then be used to record this 2D energy-angle snapshot.

A combination of rotation of the sample under a fixed excitation/detector, and rotation of the detector itself then permits measurement over a volume of $E - \boldsymbol{k}$. Sample rotation can be achieved by rotating the sample stage itself (typically on a goniometer), or by swapping between sample mounts machined with incrementally different surface normals. Rotating the detector is challenging as hemispherical analyzers are large by design to improve the energy resolution (see Eq. 1.3). A recently developed method to sidestep this problem is to augment the electron lens

system with additional electrostatic deflectors[10,11] which allow sweeping of the azimuthal angle of electrons incident on the analyzer entrance slit by ~$\pm$15°. However, as we shall see in the next subsection, the ability to move the detector is critical for efficiently studying 2D heterostructures.

Having established the experimental background of ARPES, we must address the interpretation of the ARPES spectra, specifically that of the photoemission process producing it beyond the simplified kinematic picture. A rigorous description of the photoemission process is given by the one-step model[12–14], which considers the quantum mechanical optical transition directly from the original Bloch state to the final excited state (a damped plane wave propagating out from inside the solid leaving behind a hole). Critically, this model must simultaneously capture within the Hamiltonian appropriate boundary conditions and internal scattering by other states to connect the nontrivial final state and the unknown initial state.

This is challenging in practice, and so a standard alternative is to break up the photoemission process into three parts – the three-step model[15]. These steps are:

1. Absorption of a photon by an electron,
2. its propagation to the sample surface,
3. and escape through the surface potential into the vacuum.

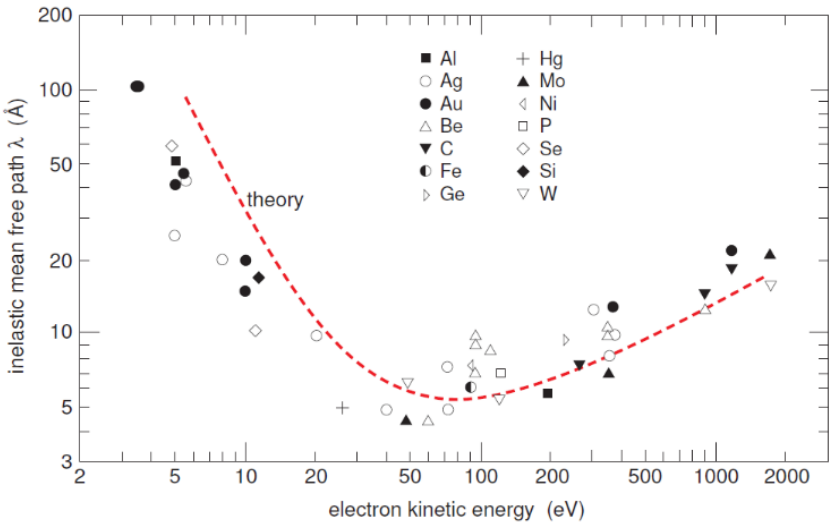

Figure 1.3. Universal curve of photoemission. Reproduced from Sean, M, *et al*., *Surf. Interface Anal*. **1** 2-11 (1979).

The third step kinematically constrains the photoelectron final state momentum. In the second step, the photoelectron travels some effective mean free path and either makes it to the surface or undergoes some inelastic scattering. Such scattering events produce a continuous background. This sets the effective penetration depth of ARPES which famously follows the so-called universal curve[16] (Figure 1.3). This curve shows that only electrons within a few atomic layers of the surface can be effectively probed; therefore, the resolution achievable in ARPES is severely limited by the surface cleanliness. This is optimized with bulk crystals by cleaving them *in-situ* immediately before measurement. UHV is required to minimize gas adsorption, with pressures below 10^{-9} Torr necessary for maintaining an already clean surface[17]. Interestingly, a uniform adsorption of a dipolar gas can cause adsorption geometry dependent band shifts in 2D materials[18].

The first step encodes the probability of an optical transition from the original state of N-electrons. Two approximations can be made here: the sudden approximation, and the dipole approximation. To apply the sudden approximation, one assumes that the electron is instantaneously photoemitted (which does not hold for low energy photoelectrons) and so relaxation processes can be neglected. That is, the final state is the antisymmetric product of the photoemitted electron wavefunction ϕ_{f} and the excited state of N-1 electrons, $\Phi_{\mathrm{f}}^{\mathrm{N}-1}$, given by the Slater determinant of the N-1 wavefunctions. The initial state is simply the antisymmetric product of the states of a single particle ϕ_{i} and the remaining N-1 electrons, $\Phi_{\mathrm{i}}^{\mathrm{N}-1}$. The photoemission probability ω_{fi} follows from Fermi's Golden rule:

$$\omega_{\mathrm{fi}} = \frac{2\pi}{\hbar} \left| < \phi_{\mathrm{i}} \Phi_{\mathrm{i}}^{N-1} \middle| H_{\mathrm{int}} \middle| \phi_{\mathrm{f}} \Phi_{\mathrm{f}}^{N-1} > \right|^2 \delta((E_{\mathrm{f}}^{\mathrm{N}-1} + E_{\mathrm{kin}}) - (E_{\mathrm{i}}^{\mathrm{N}-1} + \varepsilon_{\mathrm{i}}) - h\nu) \quad (1.4)$$

Thus the photoemission intensity distribution $P(\boldsymbol{p}, E_{\mathrm{kin}}) = f(E,T) \sum_{\mathrm{fi}} \omega_{\mathrm{fi}}$ is

$$P(\boldsymbol{p}, E_{\mathrm{kin}}) = f(E,T) \sum_{\mathrm{fi}} \left| < \phi_f \, |H_{\mathrm{int}}| \phi_{\mathrm{i}} > \right|^2 |c_{\mathrm{fi}}|^2 \delta\left(\boldsymbol{k} + \boldsymbol{G} - \frac{\boldsymbol{p}}{\hbar}\right) \delta(E_{\mathrm{f}} - E_{\mathrm{i}} - h\nu), \quad (1.5)$$

where $f(E,T)$ is the Fermi-Dirac distribution, $|c_{\mathrm{fi}}|^2 = \left|< \Phi_{\mathrm{f}}^{\mathrm{N}-1}|\Phi_{\mathrm{i}}^{\mathrm{N}-1} >\right|^2$is the one-particle spectral function, which captures the self-energy $\Sigma(\boldsymbol{k},E)$ of the excited N-1 state originating from correlations, and the interaction Hamiltonian is $H_{\mathrm{int}} = \frac{e}{mc}\boldsymbol{A}\cdot\boldsymbol{p}$ via the dipole approximation. This applies for excitation wavelengths larger than the atomic spacing, i.e. $h\nu < 3000\ eV$.

The $\left|< \phi_f\ |H_{\mathrm{int}}|\phi_{\mathrm{i}} >\right|^2$ term is often referred to as the matrix element term. It encodes such effects as the excitation energy-dependent absorption cross section, dependence on the excitation polarization, and possible interference effects. The first effect makes tunable excitation energy a particularly powerful capability. The last produces such interesting effects as the dark corridor in graphene, where the photoemission channels from the two equivalent sublattice sites interfere destructively along a particular final state momentum direction at each Dirac point[19].

The one-particle spectral function can be taken as the following Lorentzian[1],

$$|c_{\mathrm{fi}}|^2 = \frac{-\Sigma\prime(\boldsymbol{k},E_{\mathrm{kin}})}{\pi((E_{\mathrm{kin}}-\varepsilon_{\mathrm{i}}-\Sigma'(\boldsymbol{k},E_{\mathrm{kin}}))^2+(\Sigma''(\boldsymbol{k},E_{\mathrm{kin}})^2)}, \text{ with } \Sigma(\boldsymbol{k},E) = \Sigma'(\boldsymbol{k},E) + i\Sigma''(\boldsymbol{k},E). \quad (1.6)$$

In a system without correlations, the self-energy $|\Sigma(\boldsymbol{k},E)| = 1$ and Eq. 1.6 reduces to a delta function in energy. This follows from having the initial unexcited N-1 state matching exactly one of the possible final excited states. The presence of correlations renormalizes the quasiparticle energy, and the photoemission spectrum is broadened in energy. This follows from a having a finite lifetime for the excited states. Different models for $\Sigma(\boldsymbol{k},E)$ have been established in the literature[20] and can be appropriately applied to extract these lifetimes and many body effects.

To assess the contributions of these terms, typically line traces of the ARPES spectra through a feature of interest are fit to Eq. 1.5. The two possible types of line cuts are constant in energy (momentum distribution curves, or MDCs) and in momentum (energy distribution curves, EDCs). MDCs have the advantage of uniform contributions from the Fermi function and the

inelastic scattering background. If these two terms are manageable, however, EDCs can be more useful as they more directly show quasiparticle peaks[1].

Most commonly, ARPES facilities are lab-based and rely on bench-top light sources such as gas discharge lamps, and lasers. These sources produce reliable light at fixed, typically low energies. This carries the dual benefits of operating in the more tunable end of the universal curve (thereby leaving the option of enhanced sensitivity to the bulk) and enhanced momentum resolution[1]. Laser frequency multiplication can be used to generate higher harmonic light, leading to exceedingly impressive resolution[21,22]. Laser-based ARPES has the added advantage of compatibility with pulsed, time-resolved measurements. This opens the door to studying dynamics of transient excitations, such as excitons in monolayer WSe_2[23].

The other conventional ARPES facilities are synchrotron-based. Modern synchrotrons are purpose built to produce exceptionally high brilliance light and can generate essentially arbitrary photon energies limited by the insertion devices feeding the beamline with the ARPES endstation. Variable excitation energy allows fine-tuning to maximize the photoemission cross-section. In addition, it enables resolution of perpendicular momentum dependence which is typically done by sweeping through photon energy. With using higher energies comes a larger accessible momentum space $\sim\sqrt{E_{kin}}$. This can be especially useful as the matrix element term may be enhanced in a higher order Brillouin zone (with fixed sample-excitation geometry).

1.1.3 *Micro-focus ARPES, optics and synchrotrons*

Most existing ARPES systems were designed to study the surfaces of conventional, bulk systems. Such samples typically present surface areas that are a few millimeters across. Consequently, hypothetical problems of excitation beam spot-size and relative beam spot drift due

to sample rotation (to resolve angle) are not of especial priority. For example, ARPES spot sizes themselves typically measured in millimeters.

These conditions are of course unsuitable for studying either nonuniform, or simply small samples. Over the past decade, efforts[11] have been made to address this deficiency and demonstrate ARPES leveraging highly focused beams. To date, (sub-)micrometer-scale spot sizes have been achieved in at least four commissioned synchrotron beamlines using specialty optics with dedicated focusing mirrors[11]. By also incorporating fine sample translation capabilities, these systems are capable of a form of spectro-microscopy. Discussed in detail below are the two beamlines where the experiments presented in the body of this thesis were performed.

At the aptly named Spectromicroscopy endstation at the Elettra Sincrotrone Trieste, the light is focused ultimately down to a spot diameter of ~600 nm using Schwarzschild objectives[24]. These objectives use specialty multilayer coatings that provide high reflectivity albeit at fixed frequencies. Spectromicroscopy has three sets of these objectives tuned for high flux at 27, 74, and 95 eV. This micro-focusing is paired with a custom compact hemispherical analyzer (radii 60 and 20 mm). The analyzer's slit axis is fixed, but it is mounted to a goniometer that can move the whole analyzer about the sample to resolve photoemission angle. The sample mounting system is compatible with the addition of up to three electrical contacts to the sample plate which then contact leads inside the measurement chamber to which external voltages can be applied and currents measured by a connected sourcemeter.

At the MAESTRO beamline at the Advanced Light Source (ALS) synchrotron, there are two ARPES end-stations, "micro-ARPES" and "nano-ARPES", that can access energies between 20 and 1000 eV. Both systems use Scienta R4000s, large hemispherical analyzers that nevertheless are routinely rotated about the sample space. This is supplemented with deflector capabilities on

both systems. Additionally, the analyzer can be rotated in place by hand, allowing snapshot measurements along arbitrary lines. “Micro-ARPES” (“micro”) achieves a minimum spot size of ~10 um by simply using Kirkpatrick-Baez mirror pairs and tunable slits. “nano-ARPES”(“nano”) in contrast has additional access to both Fresnel zone plates[11] and capillary mirror optics[25]. With the former, diffractive selection of the beam can produce a spot size of ~0.12 microns, though a substantial amount of light is lost in the focusing process. With the latter, the spot size can be as small as ~1 micron across, while achieving similar fluxes as typical in the “micro” line. “nano” also has the benefit of having eight available electrical leads integrated into the sample mounting “puck”. Recently facile temperature control was incorporated via closed-loop cryocoolers connected to the sample stages of both systems by long, vibrationally-isolated cold fingers, very recently demonstrating stable 17K base temperatures.

1.2 Layered (van der Waals) materials

The history of layered materials traces back to before antiquity when two naturally occurring examples, graphite and molybdenite (MoS_2), were so known for their similar softness, friability, and utility as a blackener to a common lead ore, PbS, that the three shared a name to the ancient Greeks: *molybdos*. In the case of graphite and MoS_2, this softness and ease of application by friction originates from their layered crystal structures, which comprise effectively 2D atomic sheets with strong in-plane atomic bonds. These sheets however are held together by only weak van der Waals bonding which offers little resistance to in-plane forces. Thus, they can slide easily over each other when laterally pushed. A modern application of this property is so-called dry lubrication, a critical alternative to conventional lubricants in certain extreme conditions, e.g., at high temperature, or with high contact pressures.

That such layered materials can be cleaved to produce flat and pristine surfaces free of surface dangling bonds was scientifically relevant before the first monolayer crystal was ever isolated. An example is the use of graphite surfaces as atomically smooth substrates onto which gas atoms can adsorb[26,27]. If the amount of gas introduced to a closed system containing graphite is carefully accounted for, then the relationship between pressure, temperature, and adsorbed fraction reveals properties of the adsorbed gas as it condenses into a monolayer on the graphite surface – an ironically early study of isolated quasi-2D states of matter.

However, it would be more than fifty years before graphene, a monolayer of graphite, would be experimentally treated, in part due to an argument of Peierls in 1934[28] predicting that divergent fluctuations in two-dimensions would destroy any monolayer crystal, as well as the no-go argument[29] and subsequent theorem[30] of Mermin and Wagner forbidding non-vanishing Fourier components in two-dimensions in the thermodynamic limit. The practical applicability of these arguments would be called into question over the following decades, both on theoretical grounds[31,32] and in experiments, including the aforementioned adsorption studies inferring the existence of monolayer adsorbed rare gas films, as well as photoemission[33] and inverse-photoemission studies[34] of epitaxial monolayer graphene films. In these experimental works, however, interactions between the substrates and the monolayer films left it unclear if 2D physics were truly at play.

It would not be until 2004[35] that a 2D crystal would be found to be effectively decoupled from its substrate and exhibit unambiguously 2D physics. This was achieved by micro-mechanical exfoliation of bulk graphite onto a SiO_2/Si substrate to produce flakes of few-layer graphite (FLG) and even graphene. The choice of substrate generated contrast in a standard optical microscope for the exfoliated flakes without substantially interacting with them. Transport measurements on the

FLG exhibited Shubnikov-de Haas oscillations with frequency linearly dependent on the carrier density – a hallmark of electrons confined to two dimensions. This landmark result launched the field of 2D materials, and its methodology for producing atomically thin samples remains the predominant technique in the field. To date, the library of 2D materials contains 2D analogs of virtually any condensed matter phenomenon in three dimensions, from strange metals, superconductors, magnets, and topological insulators[36]. The following subsections will present background on graphene and the other van der Waals materials relevant to the experiments reviewed in the rest of this thesis.

1.2.1 *Graphene and hexagonal boron nitride*

Graphene is a sheet of sp^2-bonded carbon atoms on a honeycomb lattice. The first theoretical treatment of graphene was in 1947[37], when it was shown using the tight binding approximation that the Bloch Hamiltonian on a monatomic honeycomb lattice with only nearest neighbor hopping is given by:

$$H = \begin{pmatrix} 0 & f(\boldsymbol{k}) \\ f^*(\boldsymbol{k}) & 0 \end{pmatrix} \text{ where} \tag{1.7}$$

$$f(\boldsymbol{k}) = -t(e^{-ik_x a} + 2e^{\frac{ik_x a}{2}}\cos(\frac{k_y a\sqrt{3}}{2})), \text{ and } t\text{: hopping parameter which yields} \tag{1.8}$$

$$E_{\pm} = \pm t\sqrt{3 + 2\cos(\sqrt{3}k_y a) + 4\cos\left(\frac{\sqrt{3}k_y a}{2}\right)\cos(\frac{3k_x a}{2})} \text{ as eigenenergies.} \tag{1.9}$$

This dispersion crosses zero energy at exactly the corners of the hexagonal Brillouin zone, $\boldsymbol{k}$ = **K**, **K'**, where a low energy expansion yields the now-familiar linear, massless Dirac dispersion,

$$E_{\pm}(\boldsymbol{k}) = \pm\hbar v_{\mathrm{F}}|\boldsymbol{k}|. \tag{1.10}$$

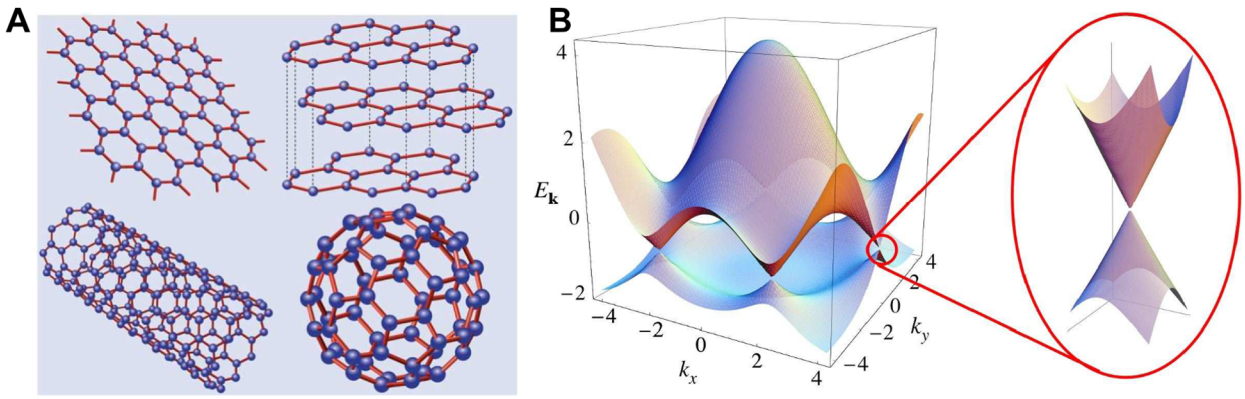

Figure 1.4. Graphene crystal and band structure. **A**, polytopes of hexagonally bonded carbon, including graphene (top left) and graphite (top right). **B**, tight-binding band structure of graphene, with zoomed in image of Dirac dispersion at a zone corner. Reproduced from Castro Neto, *et al.*, "The electronic properties of graphene", Reviews of Modern Physics **81** 2009.

Following their seminal work discussed above where they presented an image of monolayer graphene but data from FLG, Geim and Novoselov showed in 2005[38] the first direct evidence of unique behavior in graphene through the observation of the half-integer quantum Hall effect, a direct consequence of the predicted linear dispersion. In contrast, bilayer graphene (BLG) exhibited the integer quantum Hall effect expected from ordinary materials with parabolic bands and massive quasiparticles. This work earned Geim and Novoselov the 2010 Nobel prize.

It goes without saying that a stupendous variety of experiments on graphene followed in the wake of this work, such as ARPES studies revealing modulations of the Dirac dispersion due to electron-plasmon interactions[39], and the observation of specular Andreev reflection at the interface of graphene, and a superconductor[40]. For the purposes of the experiments at the heart of this thesis, graphene serves as a prototypal 2D system with which to benchmark pioneering work, as well as a conveniently air-stable single layer conductor. More recently graphene launched a mini-revolution in the field when it was observed[41] that graphene stacked with itself at a critical,

'magic' relative angle exhibits unconventional insulating and even superconducting states as a result of moiré physics converting the Dirac dispersion from the constituent layers into nearly non-dispersive flat bands at the Fermi energy. As the bandwidth sets the electron kinetic energy, this results in strong correlations and exotic phases can emerge[41–44]

These latter results (amongst many others) would not have been possible without another 2D material hexagonal boron nitride (hBN). Also known colloquially as white graphite, it is structurally very similar to graphite, with a honeycomb lattice of alternating boron and nitrogen atoms and a lattice constant mismatch of only ~1.8% relative to graphite. It was shown 2010 that hBN, an insulator, serves as a superior substrate for graphene by providing an atomically flat dielectric support largely free of defects and charge traps. Taking the additional step of fully encapsulating graphene (or any other 2D flake of interest) with hBN above and below when possible generically improves sample quality as the van der Waals interactions on either side of the region of interest naturally acts to maximize the direct interfacial area, squeezing any surface contaminations together and sequestering them into isolated bubbles[45]. Full encapsulation with hBN has the additional benefit of protecting a chemically air or water sensitive flake by forming a relatively tight van der Waals seal all around it. Additionally, few- and monolayer hBN can serve as a tunneling barrier[46] or as an inert spacer[47]. While it predominantly plays a supportive role in 2D material research, hBN has exhibited interesting physics, including hosting single photon emitter sites[48], forming a moiré superpotential with graphene[49], and exhibiting unconventional ferroelectricity[50].

1.2.2 *Semiconducting transition metal dichalcogenides*

The family of layered transition metal dichalcogenides is a large one; with chemical formula MX_2, where M (= Ti, Nb, Mo, W, Re, etc.) is a transition metal and X (= S, Se, Te) a

chalcogen, there are at least thirty combinations with layered allotropes[51]. Some pairings support multiple (meta-)stable monolayer structures[52]. This diversity in turn spans a wide range of electronic classifications including insulators (HfS_2), semiconductors (MoS_2, WSe_2), semimetals ($TiSe_2$), polar metals (few-layer WTe_2[53]), and true metals ($NbSe_2$). In addition, many have been shown to superconduct (e.g., WS_2[54], $MoSe_2$[55], and $NbSe_2$).

We have already touched on MoS_2, which belongs a small branch of the family that also includes $MoSe_2$, WS_2, and WSe_2. The bulk forms of these four combinations are naturally found with the 2H structure, comprising quasi-honeycomb lattices stacked with adjacent layers rotated by 180° relative to one another. An individual sheet consists of an alternating pattern of a M atom bonded to two X atoms, one above and one beneath, arranged with trigonal prismatic coordination. Looking at the resultant structure from above Figure 1.5 reveals the hexagonal symmetry in the monolayer shared with graphene. Compared to graphite, however, these materials in are well known to be semiconducting[56–59] and therefore easily optically addressable, a property that persists down to their monolayer form[60].

This fact, along with its air-stability and natural occurrence made MoS_2, and subsequently its family members, very attractive for early 2D research looking beyond graphene[61]. This interest persists to present day, as these materials continue to reveal new and exotic facets for study, such as spin-valley coupling[62], unconventional ferroelectricity[63], and moiré trapping of excitons[64]. Naturally, the interpretation and future development of these experiments can be greatly aided by direct knowledge of their monolayer band structures, and of the band alignments between them. To this end, most of this thesis will be focused on ARPES studies of these materials, and as the only other transition metal dichalcogenide discussed here will be WTe_2, we will refer to the family of semiconductors as the TMDs for short.

Many early probes of the nature of the semiconducting gaps in these materials using ARPES[65] and optical studies[66] demonstrated that they are all indirect, with the extrema of the valence (VBM) and conduction band (CBE) at the **Γ** and **Q** points, respectively. That the system remains gapped in the monolayer limit can be seen via its structural similarity to graphene. Expanding the graphene Bloch Hamiltonian, Eq. 1.7, about the **K**-points yields

$$H(\boldsymbol{k}) = v_{\mathrm{F}}(\tau\sigma_x k_x + \sigma_y k_y), \text{ where} \tag{1.11}$$

$$v_{\mathrm{F}}\text{: Fermi velocity, } \tau = \pm 1\text{: valley index, and } \sigma_i\text{: Pauli matrices.} \tag{1.12}$$

This dispersion lacks a σ_z term as this would index states by sublattice site. As the TMDs have broken sublattice symmetry, such a term is allowed. In fact, it can be shown[62] via $\boldsymbol{k}\cdot\boldsymbol{p}$ theory that the equivalent Hamiltonian for a monolayer TMD takes the form

$$H(\boldsymbol{k}) = at\left(\tau\sigma_x k_x + \sigma_y k_y\right) + \frac{\Delta}{2}\sigma_z. \tag{1.13}$$

The added term here manifestly opens a gap Δ at the **K** and **K'** points, which are now inequivalent. These band edges we will sometimes refer to as the **K/K'** valleys, or collectively as the **K** point if the measurement is not spin- or polarization-resolved.

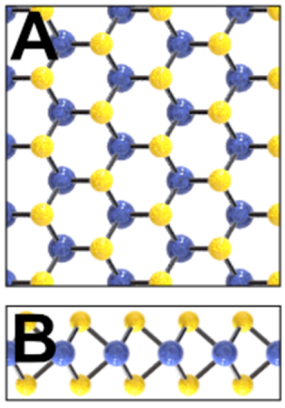

Figure 1.5. Hexagonal transitional metal dichalcogenide crystal structure. **A**, top-down and **B**, cross-sectional view of ML TMD 2H structure. Metal atoms are blue, chalcogen atoms are yellow.

Furthermore, the broken inversion symmetry and the presence of the heavy transition metal atoms introduce strong spin-orbit coupling (SOC) from the metal d-orbitals, which further

modifies the Hamiltonian[62] by lifting the spin degeneracy at the **K/K'** points in both the valence and conduction bands. As the monolayer has reflection symmetry with mirror plane through the metal atoms, this splitting must distinguish only the out-of-plane spins. The application, then, of time-reversal symmetry swaps both valleys and spins. For this to leave the Hamiltonian unchanged, the spin-splitting must be opposite at opposite valleys.

Theoretical calculations that include SOC predict large splitting of the valence band in excess of ~0.15 eV in MoX_2 and ~0.45 eV in WX_2 monolayers[62,67,68]. The splitting of the conduction band is expected to be only on the scale of a few (MoS_2) to tens of meV, the result of the SOC vanishing to leading order for the dominant orbital (coming from the metal) composing the conduction band valley[69]. Interestingly the sign of the conduction band splitting is opposite in MoX_2 monolayers vs. in WX_2. This is because the only first order SOC contribution comes from the minor orbital composition from the chalcogen which competes with the second order contribution from the dominant metal orbital.

It should be noted that this approximation is local to the valleys and is of limited predictive value for the rest of the monolayer band structure. A better qualitative picture can come from a theoretical analysis of the band structure of the bulk forms. For example, density functional theory (DFT) reveals that the VBM at the **Γ** point is mostly of out-of-plane orbital character (specifically, M d_{z^2} and X p_z orbitals)[69]. Consequently, we would expect the band structure in the vicinity of **Γ** to be sensitive to thinning to a monolayer and resultant reduction in amount of interlayer coupling. The local valence band extrema (VBE) at the **K/K'** are, in contrast, largely of in-plane character (M $d_{x^2-y^2}$ & d_{xy}) and thus should be relatively insensitive to number of layers. This opens the possibility that the global VBM momentum can shift between these two edges in the ML limit.

The argument for the conduction band is a bit more nuanced. Here, the expected conduction band extrema (CBE) at **K** and **Q** have at least some out-of-plane character, with majority orbital compositions of M d_{z^2} at **K** and minority orbital compositions of M $d_{z^2}$and X p_z for the **Q** CBE. Consequently, both CBE should be at least somewhat sensitive to changes in thickness. However, the interlayer overlap of the X p_z orbitals should be larger than that of the M d_{z^2} orbitals[69] and so plausibly the CBM could also shift from **Q** to **K/K'** on sample thinning.

Indeed, it is possible for first-principles calculations to predict such shifting for either of the band maxima for any/all of the TMD monolayers. Such predictions however, if unmoored by experimental parameters such as the lattice constants, have produced conflicting results[69] regarding the CBM momentum even when performed within the same theoretical framework, e.g., GW calculations for MoS_2[70,71]. It has been noted that the inclusion of certain orbitals (Mo $4s$ or W $5s$) in the calculation can reliably produce a direct gap[72]. A consequence of these gaps being direct is that low energy excitations would be localized to the **K/K'** point, strengthening the applicability of these monolayers in spin- and valley-tronic applications[62].

On the experimental side, even the earliest optical studies of monolayer samples were consistent with all four gaps becoming direct, for example by observing dramatic increases in photoluminescence upon thinning from two to single layer[61]. Early experiments using scanning tunneling spectroscopy (STS), a powerful technique capable of probing the local density of states (LDOS), struggled to produce a consensus for the band gap sizes[73–75] for comparison to candidate theoretical models/methods. This is in large part due to the STS tunneling probability of a given state in the material exponentially decaying with its in-plane momentum $\mathbf{k}_{||}$, reducing STS' sensitivity to far flung band edges relative to a band edge with no in-plane momentum, to wit our **K/K'** and **Γ** valleys, respectively.

One report[76] used variable-height (constant current) STS in combination with conventional constant-height measurements to also measure the energy dependence of the tunneling probability coefficient and therefrom infer changes in the $|\mathbf{k}_{||}|$ of the CBE's as they contribute shoulders/peaks to the measured LDOS of monolayer $MoSe_2$ and WSe_2. For the former, it was found that the gap was direct and at **K/K'**. However, the gap was found to be indirect in the latter, with the CBM at **Q** which was 0.08 ± 0.06 eV lower energy than observed CBE at **K/K'**. It was suggested that this discrepancy with the expectation from PL resulted from the large direct exciton binding energy in monolayer TMDs (~ 0.5 eV)[69] allowing for efficient optical transitions at the nearly energy-degenerate direct gap. It should be noted, however, that STS of semiconductors is prone to so-called tip-induced band bending[77], the shifting of observed voltages of spectral features due to spatially-variable voltage drops across the semiconductor between the rounded STS probe tip and the underlying metallic substrate. Such modulations may nontrivially impact the assumptions used here on the tip-sample distance dependence of the tunneling.

ARPES studies of these gaps were in accordance with the other experiments regarding the VBM shifting to the **K/K'** point in the monolayer limit[78–82]. Spin-resolved measurements[83] directly evinced the spin-valley locking phenomenon already expected from polarization-dependent optical measurements[84,85] However, as we will discuss in Chapter 3, attempts to access the ML TMD conduction band in ARPES have until recently necessarily introduced complications to interpreting the observed gaps relative to those of other experiments.

1.2.3 *WTe_2, a monolayer topological insulator*

The remaining material of interest in this thesis is another transition metal dichalcogenide, tungsten ditelluride (WTe_2). What sets WTe_2 apart from the semiconducting TMDs is that it was predicted[86] to not minimize its structural energy with a hexagonal lattice. Rather, it was the only

compound of the six combinations considered to fully stabilize the T_d structure, a distorted form of the tetragonal structure 1T. In the latter, each metal atom is octahedrally coordinated with its nearby six chalcogen atoms, resulting in ABC stacking with the P3m1 space group. 1T has been shown to be generically metallic[87]; however it is unstable to the formation of metal-metal bonds. Such bonding distorts the lattice, generating the T_d structure which consists of one-dimensional zigzag metal chains and inequivalent Te sites. The T_d structure is shown in Figure 1.6.

Whereas the hexagonal phase generically produces a gapped band structure, the low symmetry, chain-like T_d structure uniquely accessible to WTe_2 combined with the strong SOC it shares with TMDs can exhibit a wide range of exotic phenomena. For example, it has been shown that bulk WTe_2 is a type-II Weyl semimetal with 'large' non-saturating magnetoresistance stemming from its so-called perfect compensation[88], a balance between the electron and hole pocket sizes. The nonlinear anomalous Hall effect was observed in few-layer samples, the result of a nonzero dipole moment of the Berry curvature arising from layer polarized Dirac fermions[89]. Remarkably, it has also been shown that such few-layer samples are polar metals[63], sustaining a switchable polarization that is not screened by the mobile electrons via the stacking order[90].

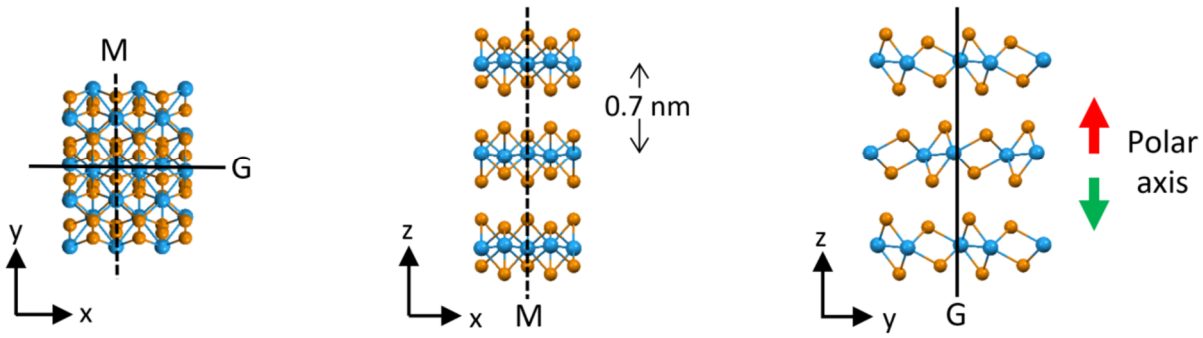

Figure 1.6. Crystal structure and symmetries of Td WTe2. M and G are the y-z mirror plane and x-z glide plane respectively. Te atoms are shown in orange, W in blue. The multilayer polar axis is shown by the green and red arrows. Reproduced from Zhao, W., thesis. University of Washington (2020).

The monolayer limit is perhaps the most interesting: it is only known single layer 2D topological insulator (2DTI). The 2DTI state has a bulk gap with a helical bands localized to the edges. These bands support topologically protected helical edge modes with resultant quantized edge conduction at low doping[91,92]. This property alone opens the door to a variety of both novel phenomena and technological applications[93]. This is especially true when combining this topologically protected state with other 2D materials, such as magnets.

Another path to exotic physics traces from the origin of the 2DTI state itself. The topological edge states come from an inversion of the low energy bands, which are all at the **Γ** point. Ordinarily, the orbital character of bands appears in the same order as the textbook orbital ordering (s, p, d, etc…). However, sufficiently strong orbital overlaps can cause the bands themselves to overlap and cross. There the bands can hybridize and anti-cross, producing a gap. This causes segments of the original conduction and valence bands to be effectively cut out and stitched onto the rest of the opposite bands. A consequent inverted band structure is topologically distinct from the ordinary ordering in vacuum. Continuity of the electronic states requires that the states of opposite character (starting at opposite sides of the bulk gap inside the 2DTI) must cross at the 2D crystal edge to swap order in vacuum. First-principles calculations have shown that the (inverted) valence band consists of W d_{yz} and d_{xy} orbitals, while the conduction band mainly consists of Te p_y orbitals[94].

Band inversion and the formation of edge states alone does not a 2DTI make, as the gap formed from the bands anti-crossing can still be negative to produce a semimetal rather than an insulator. The original theoretical work predicted this would be the case for ML WTe_2 in contrast to the other transition metal dichalcogenides considered (the semiconductors and $MoTe_2$) which would host a band insulator in the 1T' phase (the monolayer limit of T_d). Within that context the

apparent insulating state in ML WTe_2 at low temperatures[91] is suggestive of correlations affecting the band overlap. Low temperature ARPES[95,96] measurements have evinced this insulating state, showing a positive gap of ~50 meV, with the excitation-polarization dependence of the spectra consistent with the predicted band inversion. Measurements of the 2D bulk conductivity using a specialized contact geometry further suggest a highly nontrivial nature of the insulating state. Monolayer WTe_2 has also demonstrated a superconducting state[97] that competes with this insulating state, with their balance tunable by doping at levels achievable with an electrostatic gate.

A 2D semimetal with massive carriers can be unstable to the formation of a many-body ground state due to electron-electron correlations. If the densities of electrons and holes are equal the ground state could be an excitonic insulator, a hypothesized electronic ground state that has not yet been unambiguously observed. The 2D insulating state of monolayer WTe2 has unusual characteristics that make it a prime candidate for being hosting an excitonic insulator state[98]. The capability to determine its electronic spectrum using ARPES as a function of doping and temperature offered may allow unravelling of the nature of this state and observe possible spectral reconstruction that occurs as it forms as will be discussed in Chapter 5.

1.3 2D fabrication, and relevant other experimental techniques

A cornerstone of 2D materials research is the ability to stack individual 2D flakes into arbitrary heterostructures. Another is that the workflow for preparing these structures and devices, from exfoliation, isolation, and selection of appropriate flakes; to the stacking methods; to the patterning and addition of electrical contacts; is reasonably common across the field despite the sheer variety of materials. The author points the reader to a thorough treatment of this process in a colleague's recent dissertation, ref.[99]. This section will provide a briefer overview of this

workflow as relevant to the devices discussed in the remaining chapters, along with some additional comments. Experiment-specific details will be given in the corresponding chapters.

1.3.1 *Sample isolation*

Naturally, we start the discussion of 2D fabrication with the matter of preparing the constituent 2D flakes. The prevalent method is largely unchanged from the micromechanical exfoliation technique pioneered by Geim and Novoselov, though there is certainly site-to-site variation. Relatively up-to-date local exfoliation protocols can be found in the aforementioned ref.[99] and I will only expand on certain key points here.

Also known as the Scotch tape method, the technique starts with the careful addition of bulk crystals to and flush with the adhesive face of a piece of tape. By careful doubling of the tape onto crystals and pulling the tape back apart, the crystals can be repeatedly cleaved to leave new flat and unbroken crystal surfaces. As cleaving approximately halves the thickness of the original crystal, it is critical to avoid cleaving any patch too often.

If the original bulk crystal is of exceptional size (> 3mm across), then this procedure should be adjusted to prioritize the integrity of the cleaved crystals over the overall coverage on the tape. This is because the typical size of the exfoliated flakes scales with the effective contiguous surface areas of the crystals and the self-duplication protocol requires bending the tape under the crystals which can cause them to fracture. However, the resultant cleaved crystals are generally still very thick. Thus it is good practice to copy the tape as a whole by placing a fresh tape on top of it, lightly pressing the tapes together, and then peeling them apart. This can be repeated as necessary.

This author found it sometimes useful to not apply pressure against the tapes when copying in this manner, and to instead rapidly rip the new tape away (horizontally along the tape long-axis) shortly after placing it onto the original. Provided that the original tapes' crystals are large and

relatively thick, this violent process may serve to generate islands of isolated few-/mono-layers in the middle of and decoupled from the open crystal faces on the copy.

With a tape prepared, we turn to the target substrate. The traditional substrate of choice is degenerately doped Si with a grown film of SiO_2 on top which generates differential optical contrast between the substrate and exfoliated crystals of different thickness via thin film interference. Generally speaking, ~285 nm thick oxide is functional (if not optimal) for most 2D materials, with ~90 nm a better choice when trying to acquire monolayer hBN[100], among others. A relatively recent development regarding the substrate is oxygen plasma treatment immediately before usage, which removes surface organic contamination and leaves the SiO_2 surface hydrophilic and clean, save potentially for an atomically thin film of adsorbed water. While it has been argued[101] that the presence of the water layer during exfoliation can aid in the production of thin flakes, its continued presence can cause degradation in exfoliated flakes of especially water-sensitive materials, such as MBT[102]. Exfoliating such materials demands first baking out the freshly cleaned substrate in a dry environment. It should also be noted that such chemically unstable materials must be prepared and kept in inert environments, typically inside gloveboxes filled with an inert gas such as N_2 or Ar. While the former is more economical, the latter has the advantage of displacing water vapor and O_2 and has proven critical in preserving the topologically nontrivial properties of MBT.

Other common substrates include conductors, e.g. degenerately doped TiO_2[ref] and bare (doped) Si[103], which are useful for electron-depleting experiments, and sapphire [ref] which is optically transparent. However, these substrates lack the optical contrast provided by the SiO_2. Note that such contrast can be approximated by first depositing a thin film of a polymer, e.g., the

resist PMMA, of appropriate thickness onto the substrate. This has historical significance we will discuss in the next subsection.

With an appropriate tape in hand, it is inverted, placed onto the substrate, and brought into good contact by systematically rubbing the surface with soft-tipped tweezers taking care to not generate air bubbles. The tape & substrate are heated on a hotplate at a temperature of roughly 100-130° C for up to five minutes[101], then taken off and allowed to cool before the tape is peeled off slowly (< 1mm/sec). The angle the tape makes with the substrate surface as it is peeled off qualitatively affects the exfoliation, with high angles (~90°) exfoliating more total surface area of flakes which are skewed to higher thickness, and low angles (~15°) generally exfoliating less overall but with relatively more few-layer flakes. Near-instant exfoliations can also produce large areas of few-layer flakes, though they tend to have wrinkles. As mentioned, the exfoliations are then manually examined in an optical microscope and flakes of desirable thickness, shape, and approximate degree of cleanliness can be identified by color contrast. Ultimately, typical usable exfoliated flakes are between five and a fifty microns across.

Notably, alternatives to Scotch tape with less sticky adhesive, e.g. dicing tape, have anecdotally been better for the exfoliation of few- and monolayer flakes, though it is yet unclear if the residue left by such tapes on the exfoliated flakes is as routinely manageable by the rest of the sample fabrication process as that of conventional Scotch tape.

Though it was not used for any of the results discussed later in this thesis, a related exfoliation technique deserves mention as it is able to produce macroscopically large (>0.5 mm across) monolayer flakes of chalcogenides by placing the bulk flake into contact with either gold[104], or AlO_2. These have relatively strong attractive interactions with chalcogens and thus can tear away the entire monolayer surface from a bulk crystal.

A relatively common alternative to exfoliation for isolating few- or monolayer samples is physical or chemical vapor deposition (PVD/CVD). These processes involve the volatilization of relevant solid source materials upstream from a target substrate held at a high temperature in a tube furnace under vacuum. The source vapors are carried downstream by gas flow, which may include reactants for the crystal growth[105], and some fraction is deposited onto the hot substrate on which it is semi-mobile and is able to react and grow individual crystals (which are typically nucleated around surface contaminants or imperfections). While PVD/CVD can grow macroscopic films of graphene and monolayer hBN on copper[106,107], and >100 μm islands of single crystal, monolayer TMDs of high quality[108], their use in 2D heterostructure research is relatively limited. This is because the grown crystals are generally well adhered to their substrates, complicating their removal therefrom and integration into a vertically stacked device. One research direction in which PVD is critical, however, is the study of lateral heterostructures wherein two or more materials of relatively similar lattice constants are grown sequentially and contiguously as a single crystal[109]. The regions of different materials are separated by 1D heterojunctions where, for example, a staggered band alignment can cause excitons to comprise laterally localized electrons and holes.

In any case, candidate flakes are carefully characterized for thickness, uniformity, and surface cleanliness by atomic force microscopy (AFM). In brief, AFM works by measuring atomic-scale forces between a surface and a sharp probe at the end of a long cantilever. Probe vertical position adjustments needed to maintain constant force as a function of in plane position reflect the surface topography, modulo position-dependent changes in the force-distance curve. Changes in properties of the cantilever can be used as a proxy of the force on the probe; notable examples include static cantilever deflection (contact mode) while the probe in the Pauli-repulsive regime, the cantilever's oscillatory motion if it is externally driven near resonance (non-contact,

or "Tapping™" mode), and its peak quasi-static deflection if it is driven well below resonance (pulsed-force, or "Peak Force Tapping™").

Flake characterization and validation is typically done in non-contact mode with amplitude-feedback which can give relatively accurate height maps without potentially having the probe perturb the sample surface. However, it does not typically yield accurate measurements of the height difference from SiO_2 onto few- or monolayer flakes, possibly due in part to the difference in adsorbed water on the different surfaces. With this AFM mode, the relative phase between the drive and cantilever response is sensitive to the surface mechanical properties[110] and so mapping it simultaneously with topography can provide contrast between different materials, e.g. between the crystal and any surface contaminants.

Additional characterization can be done by optical studies such as photoluminescence spectroscopy (PL), Raman spectroscopy, and second harmonic generation (SHG). PL can be used to probe optically active materials like monolayer TMDs. The optical quality of a given sample can be determined by analysis of the width of expected luminescence peaks and from the absence of defect peaks[111]. A prevalence of atomic defects is often endemic to an entire batch of bulk crystals and is generally not immediately observable by AFM (though they can become apparent with time as they can nucleate degradation), so typically a batch of crystals grown by collaborators is first quickly exfoliated and validated in PL before general use.

Raman spectroscopy and second harmonic generation are both sensitive to the local symmetries and so can be used to identify when a particular symmetry is broken. For example, a Raman spectrum reflects the phonon modes in the crystal and so can identify a monolayer which would not produce a Raman peak associated with, for example, an interlayer breathing mode. Similarly, linearly-polarized SHG (lin-SHG) is forbidden in centrosymmetric systems[112] and so

can disambiguate the parity of the number of layers in a flake with a hexagonal lattice. In odd-thickness flakes (with honeycomb lattices), centrosymmetry is broken and so the SHG is nonzero with its intensity vs co-linear polarization following a six-fold pattern. The intensity is maximized when the polarization is aligned to an armchair axis of the honeycomb lattice[113]. Critically this measurement allows different flakes, say TMD monolayers, to be crystalographically aligned modulo 60°.

However, the two elements in a TMD or hBN occupy alternating sites on an armchair, thus orienting the armchair axes. This distinguishes 0° ("AA-like") from 60° ("AB-like") alignment between honeycomb monolayers which, as we will see in Chapter 2, may have different properties. A technique for determining the (relative) armchair orientations in two flakes is phase-resolved lin-SHG[114–116] (phase-SHG) wherein pulsed lin-SHG excitation is first passed through a reference z-cut quartz crystal which generates its own co-lin-SHG. This reference SHG and the excitation travel to the flake (with an armchair axis aligned to the incident polarization) where the excitation generates SHG and the reference is back-reflected. When two SHG pulses arrive at the detector, they will be time delayed from each other due to the dispersive optics in the system upstream of the sample. This temporal displacement can be Fourier transformed to reveal a spectral fringe pattern at the detector, the phase of which depends on the pulses' phase difference. The phase of the sample lin-SHG depends on the armchair orientation, and so two flakes will have identical armchair orientations relative to the lin-SHG polarization axis if their phase-SHG interference patterns have the same fringe phase.

1.3.2 *Heterostructure assembly*

With flakes in hand, the next step is of course to design and assemble the heterostructure. Even more so than in the previous section, dissertations predating this one such as ref.[99] have

already gone in great detail on this topic. Rather than rewriting the wheel, this section will aim to add some details specific to the samples discussed in the rest of the thesis and present some recent developments.

We start with some historical context. The original method for van der Waals stacking is the so-called wet transfer technique. This involves first exfoliating using a substrate, say Si, coated with thin films of PMMA on PVA, a water soluble polymer. Once a usable flake is identified, the substrate is broken down to a ~4×4 mm square centered on it which is then placed flake side-up in clean water. This dissolves the PVA leaving the flake-on-PMMA-film floating on the water surface. The film can then be scooped up with a flat wire loop, aiming to have the flake's open side facing away from the loop. This is then transferred onto a target flake or stack using a micromanipulator system with the PMMA ripped away from the loop and left on the substrate until cleaned away using the standard PMMA cleaning procedures laid out in other works[99]. A more complex heterostructure is built thusly one layer at a time.

This method is by most metrics strictly inferior to the various methods of dry transfer, as it requires the use of water (which precludes water-sensitive materials), exposes nearly every interface to PMMA contamination, and is much less controllable as the free-standing PMMA film tends to vibrate during transfer. This leads to both poor control over alignment and substantial air/contaminants trapped in bubbles between the flakes. It should be noted, however, that a variation on this is still commonly used to transfer PVD/CVD grown crystals where rather than dissolving PVA with water, either the copper or SiO_2 is etched away chemically. In addition, most of the problems mentioned above are largely irrelevant when not transferring to form a 2D heterostructure. In fact, that wet transfer requires virtually no downward pressure on the substrate can be critical, e.g. when placing a sample onto a TEM grid.

Turning now to the currently standard family of techniques for van der Waals stacking, collectively referred to as dry transfer (relative to wet transfer, which involves water). These techniques use ‘stamps’ to sequentially pick-up the heterostructure on layer at a time. Generally, they involve using cured poly-dimethylsiloxane (PDMS), a thick, elastic, transparent, and chemically/thermally inert polymer as a soft and flexible support placed on a glass slide. Most dry-transfer methods have a thin film of polymer on top of the PDMS which has finite adhesion to and thus able to pick-up 2D flakes under certain polymer-specific conditions.

The version predominantly used by this author, which has polycarbonate (PC) as its polymer film of choice, has the advantages of being generally reliable, providing high control over where and in what manner the polymer (and accompanying flake or stack) comes into contact with the substrate/exfoliation, and compatibility with transferring at temperatures above 100° C (which correlates with higher quality interfaces with fewer bubbles). However, PC generally requires high temperatures (>165° C) to melt down and complete a heterostructure, which may be incompatible with especially temperature sensitive materials[102]

A small difference between the protocol detailed in ref.[99] and that used in the primary works presented below is that immediately before melting a heterostructure down, the author finds it useful to use a sharp needle to poke a hole in the film ~100 um away from the region where the stamp had been touching the substrate during previous transfers. As the film must be delaminated around the hole, this area can help delaminate the film as whole which is a key step for melting down. The remaining (large) difference between this work and the reference is that here, once the stamp is down and the flakes/stack are brought together on the substrate, the system is usually first heated to ~155° C. It is then allowed to cool to ~110° C before the stamp is continually retracted at a low speed (~.5 um/sec) by the micromanipulator z-motor. This process takes the PC above its

glass transition temperature (~147° C) to the point where it is able to flow and thus conform to everything underneath it, including the target flake. This greatly enhances the interaction between the PC film and the flakes on the substrate. PC used this way will generally pick everything up if it is able to pick-up anything at all. Exceptional cases include PVD/CVD grown crystals[†], MBT and $NbSe_2$ which adhere extremely strongly to SiO_2[117], and thin-bulk of $NiPS_3$ [REF], which is relatively brittle and self-cleaves during pick-up. The lift-up temperature of ~110° C is a compromise between being cool enough that the film is not too attracted to the substrate, and not requiring so much cooling that the resultant relative thermal contraction between stamp and substrate causes the film/substrate interface to move erratically during lift-up.

A recently introduced polymer for dry transfer is polycaprolactone (PCL), which has an abrupt melting transition at ~60° C. PCL has been found to have an exceptionally strong attraction to most van der Waals materials[117]. Taken above its melting point, it also behaves very similarly to PC taken above 150° C, becoming able to entirely conform to anything underneath it. It recrystallizes with some hysteresis, typically solidifying at around 40° C. However, compared to PC, solid PCL is very hard and adheres poorly to SiO_2. This may contribute to its superior ability to pick-up flakes by itself compared to the other common polymers, PC and poly-propylene carbonate (PPC), as it will tend to flex less after being conformally molded around a flake and thus be less likely to bend away and lose contact with it anywhere. A distinct disadvantage of PCL compared to PC, however, is that its solid thin-film form has micron-scale grains which are translucent (resembling grains of frost) rather than transparent, reducing visibility to the point of making isolated graphene very nearly invisible on the stamp.

[†] PVD grown TMDs can be loosened from the growth-SiO_2 by submersion of the entire substrate in water, or a 1:1 solution of water:IPA. The flakes can then be dry-transferred as normal and devices made this way have shown reasonable transport characteristics[203], and ARPES spectra as shown in the previous subsection.

A brief summary of the transfer procedure with PCL is as follows:

1. A new PCL stamp must first be taken through a dry run of the following steps on a clean substrate (ignoring steps involving flakes/alignment). This serves to smoothen the PCL film surface, which when freshly made is rough due to the crystal domains.
2. After the touchdown point of the stamp is adjusted as desired, the substrate is heated to ~50° C. At this temperature, the stamp left hovering but nearly touching over it should not be visibly affected by the heat.
3. Flakes are aligned as necessary, à la with PC.
4. The stamp is brought down into contact, stopping ~10-20 um shy of bringing the flakes/heterostructure together.
5. The micromanipulator motor is used to slowly and smoothly bring the stamp down and the heterostructure together.[‡] Typical speed is ~0.5 um/sec.
6. Once the heterostructure is entirely on the substrate, heat to 60° C to melt the PCL.
7. The heating can be turned off and the stage allowed to cool to below 30° C at any desired rate. However, the film/stamp should not be allowed to meaningfully move vertically away from the substrate/stage in this step. Either the motor is set to an appropriate speed and made to constantly move the stamp towards the stage as it thermally contracts during cooling, and/or adjustments to the stage height/stamp position are made manually. It is key that the boundary where the film leaves the substrate surface is not allowed to kink and stretch too much. This would manifest as a deep shadow at the boundary.

[‡] If the goal is to pick a flake up and it has clearly been "pulled up" by the heterostructure due to van der Waals attraction before the stamp has been lowered onto where the flake used to be (resulting in a color change of the flake to ~grey where it would otherwise still be on the substrate and thus be non-greyscale), then one can skip to step 8.

8. Below 30° C, the manipulator can be set to a low speed and set to retract the stamp from the substrate. If the boundary was not allowed to stretch too much, the film will eventually lose contact there and begin to leave the substrate as the stamp retracts. Continue until the stamp is entirely off the substrate. If the adjustments in step 7 were insufficient, the stamp will instead abruptly snap away from the substrate.

It is possible to exfoliate directly onto the PDMS and use a sufficiently large flake on it to overlap and pick up the subsequent layers of the heterostructure, though care must be taken not to allow the stack to wholly come into contact with the SiO2 substrate lest the whole stack be dropped off upon retraction of the PDMS 'stamp'. This is because the PDMS-flake adhesion is weaker than that of any of the flakes to SiO2, which is in turn weaker than the van der Waals attraction between the flakes. This procedure has the benefits of not involving a polymer that must be dissolved away (which requires solvent exposure and nearly always leaves surface contamination) and leaves an avenue for "flipping" of the stack by picking it up from the PDMS using another stamp. This is useful in cases where it is impossible/implausible to pick-up what should be the top-most layer first, so it is instead picked-up last at the end of a heterostructure built from the bottom up[118], though there are other means of achieving this so-called flip-chip technique using PPC[119]. Finally, it is also possible to simply exfoliate most of the materials on PDMS and build the heterostructure by dropping off each layer one at a time.

An additional notable recent development is so-called tear-and-stacking[120]. Using any of the dry-transfer methods, one relies on the van der Waals attraction between flakes to pick-up only a part of a large few-/monolayer flake by bringing only that part into contact with a stack-on-stamp at low temperature, then retracting the stamp away and tearing the target flake. The rest of the flake can then be picked up underneath. The purpose of this is to achieve high precision in the

relative angle between the flake halves, which is critical for studying critical-twist-angle phenomena such as "magic angle" graphene physics. A refinement of this technique involves using AFM-electrochemical cutting[121] to define isolated patches of graphene, possibly with additional features meant to prevent the stacked layers from slipping and rotating away from the desired angle. Though this cutting has also been demonstrated with TMDs, the underlying electrochemical reaction requires the presence of water and is therefore incompatible with water-sensitive materials.

1.3.3 *Heterostructure processing and related characterization*

The previous sections have covered how to prepare arbitrary all-2D heterostacks which in principle can then be placed onto arbitrary substrates. However, without the presence or addition of macroscopic electrical leads, e.g., deposited metal films, these structures would be floating and wanting for perhaps one of the powerful tools in the 2D arsenal – tunability by local electrostatic fields. The addition ("patterning") of such metal features is most commonly done via electron-beam lithography to define the desired features into a thin film of a resist (typically PMMA) atop the entire substrate, followed by a deposition of the desired metals. Standard techniques for the deposition include electron-beam evaporation, sputtering, and thermal evaporation. The designed pattern emerges from the uniformly deposited metal surface when the excess resist (and the metal on it) is removed, typically by solvent treatment ("lift-off"). Again, the most relevant of these processes are exquisitely detailed in the referred dissertation[99].

A noteworthy alternative to these techniques is shadow masking, where a thin physical mask with holes with the shapes of the desired features is placed atop the substrate (aligned as necessary) before metal deposition to produce the pattern. This method suffers from relatively low

resolution (limited by the aspect ratio of the mask's features) but can be done relatively quickly and without the use of a resist.

As a result of the fabrication process, heterostructures are often coated in a thin layer of polymer residue. This is especially the case following patterning as generally resists are known to not clean especially well by standard solvents. PMMA is among the cleanest standard resists, but AFM topography can show a flake from which only PMMA has been added and dissolved by long baths in acetone (24 hours) followed by dichloromethane (48 hours) reveals a nearly uniform, rough coating of polymer residue with occasional gaps down to the BN flake.

Many experiments, such as transport and PL, are insensitive to the surface of the device provided the material/layer of interest is isolated from it due to, for example, encapsulation from above by hBN. Surface-sensitive techniques like ARPES, in contrast, are by definition going to suffer from the addition of surface contamination. Furthermore, some devices must be made with multiple stacking-deposition-patterning steps, potentially introducing nontrivial contamination into the device. For example, a device demanding metal contacts in the middle of the stack usually starts with hBN placed onto graphite to form a back gate. Onto this gate the desired contacts are patterned. The rest of the device is then stacked and then placed atop the back gate and contacts – note that the material to which contact is being made must go directly onto the patterned, polymer-contaminated surface.

The standard method for handling such contamination is by annealing at temperatures above 200° C to thermally degrade and volatilize the organic residue. Higher temperatures are generally more effective. The annealing environment can be open-air, (ultra-high) vacuum, or under gas flow of O_2, H_2, Ar, or any mixture thereof. The environment is chosen to maximize reactivity with/removal of the contamination at the high temperature. The combination of

temperature and environment required to fully clean a surface of course depends on the nature of the contamination. Tape and PCL residue, for example, readily anneal off at less than 400° C in 95% Ar/5% H_2. PPC interestingly anneals away at 250° C in vacuum, even out from under a heterostructure. PMMA residue, however, requires at least 500° C in an O_2/Ar environment, and to the author's knowledge the complete thermal removal of PC has not yet been demonstrated.

However, one is limited by the stability of the sample as whole. While Si/SiO_2, hBN, and graphene are all certainly stable in a low O_2 environment up to at least 500° C, exposed TMDs can degrade if annealed in UHV above ~400° C. Furthermore, very thin-films of metal (<10 nm) will undergo Ostwald ripening and become discontinuous if kept above 250° C for too long. Even greater care must be taken with less stable 2D materials such as WTe_2 or CrI_3, even when encapsulated. MBT has been known to lose its topological properties if taken above ~75° C even in an inert atmosphere.

A consequence of these limitations is that the surfaces of devices that either involve PC, intermedial contacts, or a final step of patterning can only be partially cleaned by annealing, if at all. To fully remove surface contamination, we turned to mechanical means – AFM cleaning. As discussed previously, contact-mode AFM involves the rastering of the sharp probe tip over a surface while it is in the repulsive regime, i.e., in contact. As the polymer residue is soft relative to the out-of-plane strength of 2D materials, it is possible to nanomechanically push the residue around on our devices' surfaces while using only relatively low forces (<100 nN, typically). With line-spacing smaller than the probe tip radius, a scan can systematically sweep an area free of contamination which accumulates at the sides and end of the scan area.

Care must be taken when scanning in contact mode across the edge of a few- or monolayer flake, as the force of the tip combined with an entrained hard piece of contaminant can tear into

the relatively weak edge and cut or even mangle the flake [FIG]. For this reason, it is useful to first scan with Peak-Force Tapping™ (PFT), or a similar pulsed-force AFM mode. PFT has the probe sinusoidally come into contact with surface, stop when a set force is reached, and retract with a period of ~1 ms. While the contact time is relatively brief (~.1 ms typical), this still represents a substantial fraction of the duty cycle. If the scan surface velocity is, say, 50 um × 0.4 Hz ~ 20 nm/s, the probe traverses a mere 20 pm laterally each cycle. This allows PFT scanning to move most contaminants with small pushes of finite lateral force. With care, it is even able to use the probe body to push away large particulates with PFT, e.g. unfortunate dust particles [FIG]. However, unless the surface velocity is set very low, PFT struggles to fully clean a surface. Thus it is generally still necessary to finish a clean using contact-mode. When the area is essentially free of large particulates, contact mode cleaning can have the added effect of pushing out trapped bubbles at the interfaces when scanning over an edge, provided the force is sufficiently high and the bubble sufficiently close to the surface.

As mentioned in a previous subsection, an effective means to remove organic residue is oxygen plasma treatment. However, the high energy plasma also etches even the relatively-chemically inert faces of hBN and graphite. Consequently, its usage is limited to cleaning substrates, and patterned hBN back gates (with very short exposure time, < 20 seconds, typical).

Following the completion of a heterostructure or device, it can be useful to do preliminary characterizations. Many of the previously discussed methods for characterizing exfoliated flakes can be used, of course. The most natural and facile methods of these is perhaps AFM, by which one can naively characterize the overall cleanliness of the interfaces from the distribution of bubbles of trapped contamination. In addition, AFM can show some features of the ultimate geometry of the device at higher resolution than optical microscopy, potentially revealing where

certain layers were, say, inadvertently shorted together. Mapping of the AFM feedback signal itself (e.g. the deflection signal with contact mode AFM) with a cleaned surface can reveal even a monolayer step buried in a stack under tens of nanometers of other flakes. Furthermore, that certain AFM signals are surface-material sensitive can help disambiguate the position of a thin layer at the top of the stack from confounding features from other layers.

Another preliminary characterization that will be of use later is piezo-response microscopy (PRM). A cousin of AFM, PRM is a probe microscopy which typically follows the surface topography using contact-mode AFM feedback. The signal of interest is the sinusoidal force on the probe tip by the surface's piezo-response to an AC voltage applied either to the sample itself with the probe grounded or vice versa. Notably, conventional PFM uses frequencies well below the mechanical resonance of the cantilever to minimize mechanical coupling to the PRM signal. However, it is possible to operate close to the contact resonance of the cantilever (which is typically ~10× the free-space resonance) which offers higher signal sensitivity at the cost of mechanical coupling[122]. It was recently shown[119] by contact-resonant PRM that moiré superlattices can relax to maximize the areas of the domains with energetically favorable stacking, separated by regions where centrosymmetry is broken. It is at these boundaries that piezo-response becomes possible, though the response is predominantly in-plane. As this relaxation leaves the overall moiré period intact, and the moiré pattern is function of the layers' relative angles and lattice constants, this measurement can be used to determine the exact relative angle modulo 60° and if there are, say, long-range strain gradients which will stretch the moiré pattern [FIG].

Chapter 2. μ-ARPES OF 2D HETEROSTRUCTURES

A variety of 2D structures have generated substantial research interest including graphene/hBN[123]; graphene/graphene[44,124]; graphene/TMD[125] and TMD/TMD[126–128] for efficient photocurrent generation; and graphene/hBN/TMD for light-emitting diodes[129]. In TMD heterobilayers, ultrafast charge transfer[130] and formation of layer-polarized interlayer excitons[131] have been observed. Such heterobilayers are also predicted to host rich valley physics[132] and valley polarization of the interlayer excitons has been seen[84] in aligned (small twist angle) heterobilayers of WSe_2 and $MoSe_2$[133]. Understanding and exploiting the physics in this exemplar system and potentially others hinges on knowing the band structure and properties of interlayer excitations.

Although optical and transport studies successfully probed many facets of the underlying physics in the TMD/TMD system, many critical questions cannot be directly answered by these techniques alone. These include: Does a semiconductor heterobilayer have a direct bandgap at the K points? To what extent do the orbitals hybridize? Can one regard the bands at K as simply being those from isolated monolayers? What are the band offsets, which govern the nature and binding energy of interlayer excitons? And are the layers in the heterobilayer commensurate?

ARPES has the potential to answer these questions. Conventional ARPES has been used extensively to determine 2D band structures in large-area van der Waals structures[78–80,83,134–136]. However, 2D heterostructures are generally limited to a few microns in size, necessitating the use of μ-ARPES techniques, and lack naturally clean surfaces as fabricated, impacting ARPES resolution[81,82,137]. This chapter will explore the introduction of a sample design affording spectrometer resolution-limited μ-ARPES measurements of artificially stacked heterostructures, as reported in Wilson, N. R.*; **Nguyen, P. V.*** *et al.* Determination of band offsets, hybridization, and exciton binding in 2D semiconductor heterostructures. *Sci. Adv.* **3**, e1601832 (2017)[138].

2.1 ARPES of 2D materials

To contextualize this work, we will first briefly review its predecessors. The introduction has already discussed the pioneering ARPES studies of graphene that quickly followed the initial report[35]. These works achieved high resolution by studying large-area, pristine graphene films grown *in-situ* by graphitization of (0001) SiC[39]. ARPES of TMDs, however, were initially limited to bulk studies. An inventive approach[78] for realizing ARPES-compatible 2D samples deposited potassium onto the freshly cleaved surface of bulk MoS_2. The potassium intercalated in between the two topmost layers, simultaneously doping and separating them spatially. The resultant quasi-freestanding ML was shown to be direct-gapped, as anticipated by prior optical and transport studies. However, this technique requires substantial doping ($n_{2D} \approx 3.8 \times 10^{13}$ cm^{-2}), which complicates quantitative comparison of its derived band properties to other measurements. For example, comparison of observed band gap of $E_g \approx 1.8$ eV to PL[70] implies an exciton binding energy of less than 0.1 eV, which is substantially less than expected[75].

Conventional ARPES measurements of atomically thin TMDs probed films grown by either molecular-beam epitaxy on SiC[79], or CVD onto silicon[139]. These techniques produce scalable large samples that are suitable for technological application, but incompatible with heterostructure fabrication. Nevertheless, they produced spectra of sufficiently high quality to, for example, cleanly resolve the ~100 meV spin-orbit splitting at the **K**-valley in MoS_2.

μ-ARPES has been applied to few- and monolayer TMD samples prepared both by CVD growth[81] and exfoliation[82,137]. Though these works were largely in qualitative agreement with the literature, e.g., observing a clear indirect-to-direct gap transition on thinning to single layer, they failed to resolve fine details such as the **K**-valley splitting. As will be shown below, this is not a fundamental limitation of μ-ARPES and can be improved upon with appropriate sample design.

2.2 Proving approach and sample design via WSe_2

To illustrate our approach and demonstrate its effectiveness, we first study the effect of hybridization between monolayers of WSe_2. The optical image in Figure 2.1**A** shows a heterostructure with an exfoliated WSe_2 flake that naturally has monolayer (1L), bilayer (2L) and multilayer (bulk) regions. Figure 2.1**B** is a schematic cross-section. Using PC-based dry-transfer, the flake is partly capped by a graphene monolayer (G). The graphene protects the TMD, and distances it from surface polymer contaminants. It rests on a thin graphite flake, exfoliated directly onto a p-doped silicon chip to serve as an atomically flat conducting substrate. Contamination trapped between the layers during transfer collects in blisters which consolidate on annealing to leave the remainder of the interfaces atomically clean[140]. The PC is removed by standard solvent treatment followed by thermal annealing in an Argon (95%)/Hydrogen (5%) atmosphere at 400 °C for 2 hours. To ease coarse optical alignment, the Si substrate is scribed from an edge to within ~0.5 mm away from the sample.

μ-ARPES was performed at the Spectromicroscopy beamline, with linearly polarized radiation focused to a ~0.6 μm diameter spot by a Schwarzschild objective[24] and incident at 45° with respect to the sample. The energy and momentum resolution of the hemispherical electron analyzer were ~50 meV and ~0.03 $Å^{-1}$ respectively. Scanning photoemission microscopy (SPEM) maps were acquired over the energy range of the fixed detector (~3.5 eV at the pass energy used), integrating over its angular range of ~15° (at 70 eV this is ~1.1 $Å^{-1}$). The sample temperature during the measurements was 110 K. Before measurement, the sample was annealed in UHV in a preparation chamber for several hours at up to ~400° C to remove adsorbates. It is best to ramp the anneal temperature slowly, allowing the pressure to fall and recover before increasing the target. Annealing at higher temperatures, or well after pressure is minimized can damage the sample.

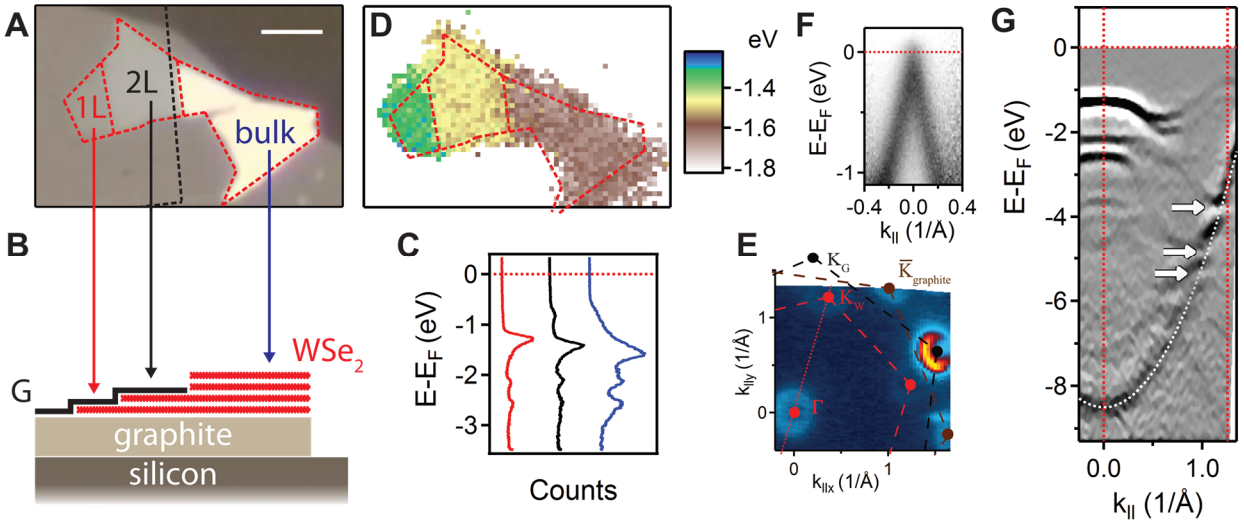

Figure 2.1. Bands in graphene-encapsulated WSe2 measured by μ-ARPES. **A**, Optical image and **B**, schematic cross-section of an exfoliated WSe_2 flake with monolayer (1L), bilayer (2L) and bulk regions (red), partially capped with monolayer graphene (G, black) and supported by a graphite flake on a doped silicon substrate. **C**, Angle-integrated spectra from regions in **A**. **D**, Map of the energy of peak emission, showing contrast between 1L, 2L and bulk regions. **E**, Momentum slice through the graphene **K**-point showing that E_F is at the Dirac point. **F**, Momentum slice along **Γ** – **K** (WSe_2) in the 1L region. The intensity is twice differentiated with respect to energy. Anti-crossings between the graphene valence band (white dotted line) and the monolayer WSe_2 bands are indicated by white arrows.

The sample is located by SPEM using a ~1 μm beam spot at 74 eV photon energy. Figure 2.1**C** shows momentum-integrated spectra taken at points in each region of the WSe_2 flake. The highest intensity peak shifts downwards monotonically in energy as the number of layers increases. A SPEM map of the peak energy vs location (Fig. 2.1**D**) therefore shows contrast between 1L, 2L and bulk. All spectra were highly consistent within each region, with no spatial variations that would signal fixed charges from contamination or in the substrate, and no drift due to charging resulting from photoemission was detected. From momentum-resolved energy slices we could determine the orientations of the WSe2 flake, graphene cap and graphite support (Fig. 2.1**E**). Figure 2.1**F** shows a momentum slice through the graphene **K**-point in the 1L region. E_F is

determined by fitting the edge of the graphene dispersion. The Dirac point energy E_D coincides with E_F (red dotted line) to within the measurement accuracy of <50 meV, implying minimal charge transfer to the graphene. This implies there is not a significant density of defect states in the gap of the WSe_2. Figure 2.1**G** shows the second derivative of a momentum slice along **Γ**-**K** of WSe_2 in the 1L region. The valence band of the capping graphene is marked by a white dotted curve. It hybridizes with the WSe_2 bands producing avoided crossings (white arrows) similar to those seen in graphene on MoS_2[80]. These features are less than 3 eV below E_F and the important WSe_2 bands nearer E_F[140] are not affected.

Figure 2.2 presents **Γ** - **K** slices showing the important features within 4 eV of the Fermi level for the 1L, 2L and bulk WSe2 regions, along with their second derivatives. All features of the upper bands are well resolved. The spectra are consistent with expectations based on the

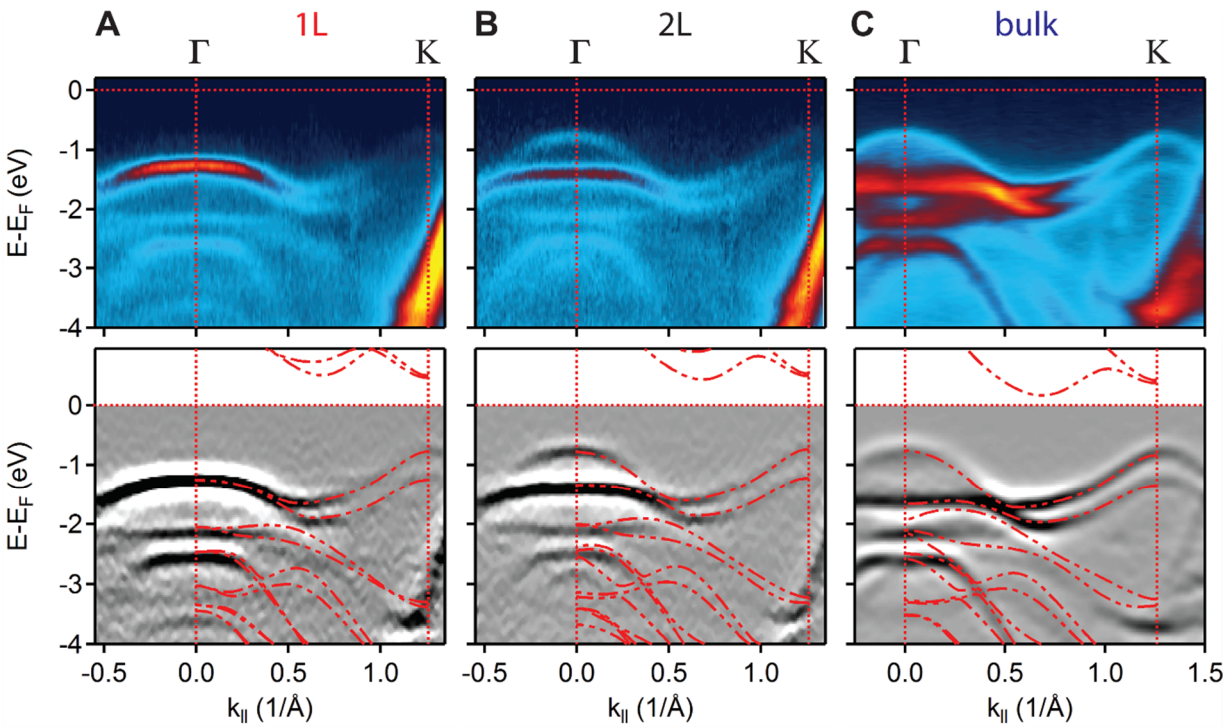

Figure 2.2. Layer-dependent band hybridization in WSe2. **A-C**, Momentum slice of unprocessed (above), and twice-differentiated ARPES (below) along **Γ** − **K** of WSe_2 in the 1L (**A**), 2L (**B**), and bulk (**C**) regions. Rigidly shifted DFT calculations are overlaid (red dashed lines).

literature[141] and density functional theory (DFT, overlaid red dashed lines) reproduces the upper valence band well with no adjustable parameters other than an energy offset chosen to match the uppermost measured band at **Γ**. The bands near **K** are almost unchanged from monolayer to bulk[142,143]due to their in-plane orbital character (W $5d_{xy}$ and $5d_{x^2-y^2}$), and in the monolayer[69,141] the valence band edge is at **K**. On the other hand, there are strong hybridization effects on the bands near **Γ** due to their out-of-plane orbital character (Se $4p_z$ and W $5d_{z^2}$). In the bilayer and bulk, the valence band splits at **Γ** with a higher-mass band 0.25 eV below that in the monolayer and lower-mass band 0.50 eV higher. In the bilayer, the valence band edge is still at **K**, while it moves to **Γ** in the bulk.

2.3 $MoSe_2/WSe_2$ heterostructures, band alignments and hybridization

Having demonstrated a sample preparation paradigm capable of producing high quality spectra, we turn to semiconductor heterobilayers. Figure 2.3**A** is an optical image of a sample with an $MoSe_2$ monolayer partially overlapping a WSe_2 monolayer forming a heterobilayer region (H). The monolayers were aligned during transfer by identifying the crystal axes using polarization-resolved second-harmonic generation[112,144,145]. As before we included a protecting graphene cap and a graphite support. Figure 2.3**B** shows angle-integrated photoemission spectra from one point in each region. The largest peak is ~200 meV lower in the $MoSe_2$ monolayer than in the WSe_2 monolayer, while in the H region there are two peaks that are shifted relative to the monolayer peaks. As a result, a map of the energy where the intensity is highest vs position (Fig. 2.3**C**) shows contrast between monolayer and H regions. In constant-energy slices the **K**-points of the monolayers coincide in momentum space (Fig. 2.3**D-E**), confirming a twist angle less than 1° and consistent with lattice constants differing by <1%.

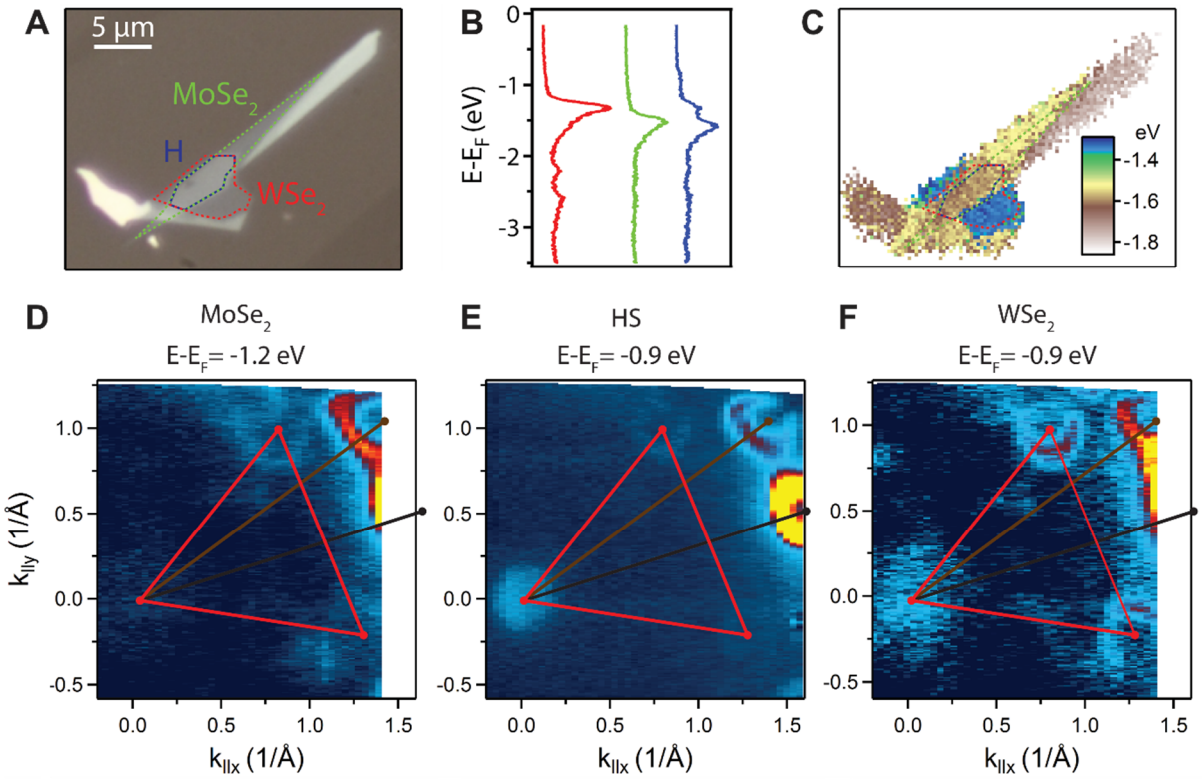

Figure 2.3. ARPES of a 2D heterostructure. **A**, optical image showing 1L $MoSe_2$ (green) and WSe_2 (red) sheets which overlap, with $MoSe_2$ on top, in an aligned heterobilayer region (H, blue). **B**, angle-integrated spectra in the three regions. **C**, map of the energy of maximum emission. **D-F**, constant energy slices with highlighted TMD **Γ** and **K** points (red circles connected by lines), graphene **K** point (black circle connected by line) and graphite K point (brown circle connected by line) from: the $MoSe_2$ flake (**D**); the heterostructure (**E**); and the WSe_2 (**F**). the TMD **Γ** and **K** points were found by fitting line profiles and coincided to within a rotation of 1° and a relative reciprocal spacing of 1%.

The variation in band structure across the heterojunction is seen in the **Γ − K** momentum slices in Figure 2.4**A-C** for 1L $MoSe_2$, 1L WSe_2, and the heterobilayer, respectively. The upper valence bands in the monolayer regions are again well matched by DFT (green and red dashed lines). The spin-orbit splitting at **K** is much smaller in the $MoSe_2$ than the WSe_2 and the valence band edge is substantially lower. In the heterobilayer, the bands near **K** are very similar to the bands in the monolayers, implying weak interlayer hybridization near **K** as was the case for the

WSe_2 homobilayer. On the other hand, the bands at **Γ** are substantially different from those in the monolayers, implying significant hybridization, again as in the WSe_2 homobilayer. Nevertheless, the valence band edge remains at **K**. This is important for the electrical and optical properties.

Interestingly, we clearly see three bands within 0.5 $Å^{-1}$ of **Γ**, not just two as would be expected from homogeneous hybridization of one band from each monolayer. We note however that the third band resembles the upper band in the WSe_2 homobilayer (Fig. 2.2**B**), in which the layers are perfectly commensurate having the bulk 2H stacking. We also recall that when

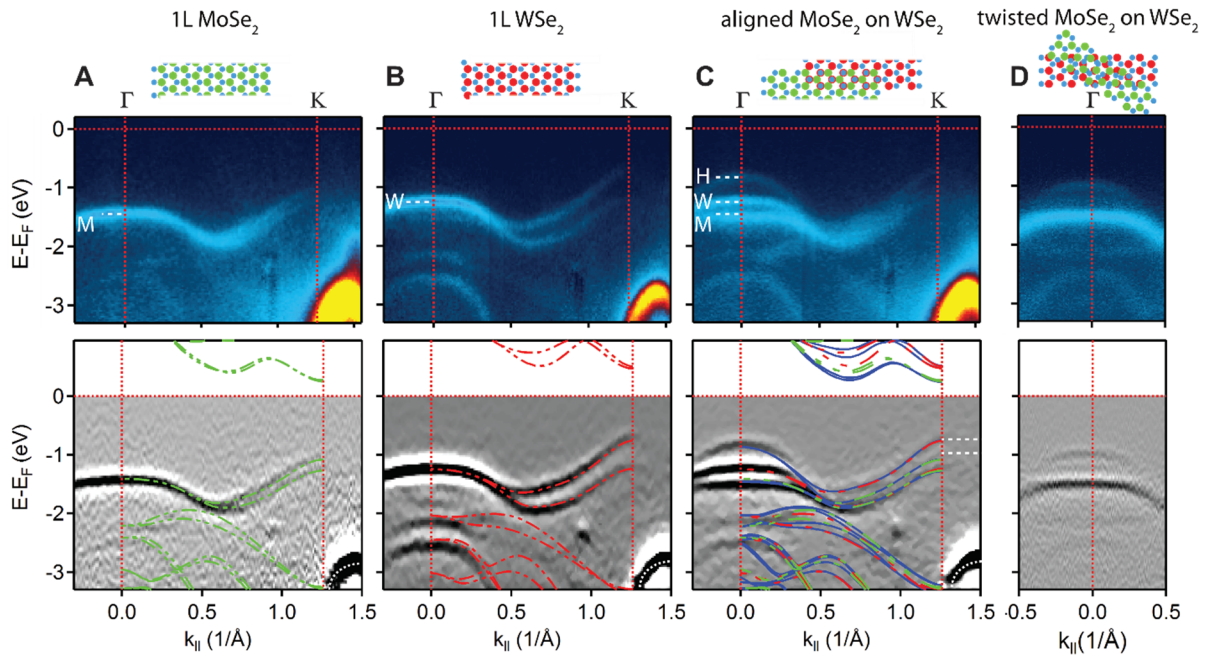

Figure 2.4. Bands in a 2D heterostructure. **A-D**, momentum slices along **Γ − K** in the three regions, (above) unprocessed and (below) twice differentiated, with cartoons of the structures above. Superposed dashed colored lines are DFT calculations for $MoSe_2$ (green), WSe_2 (red), and an aligned heterostructure (blue). The graphene valence band is indicated by a white dotted line. The white dashes in the lower panel of **C** indicate the valence band maxima in the monolayer $MoSe_2$ and WSe_2, and hence the valence band offset. The white dashed lines in the upper panels mark the valence band maxima in the isolated regions (W, M), and in the aligned heterobilayer (H). **D**, a momentum slice near **Γ** in another heterobilayer intentionally misaligned by about 30°. Here only two bands are seen, indicating that the third band near **Γ** in the aligned heterobilayer (**C**) arises from commensurate domains.

monolayers with mismatched lattice constants are stacked, elastic energy considerations will ensure that any commensurate domains have finite size. This has been demonstrated for graphene on hBN[146]. For zero twist angle the scale of the domains is $a^2/\delta a$, where a is the lattice constant and δa is the difference. Here this scale is ~100 nm, less than the X-ray spot size. The spectrum of the heterobilayer could thus be interpreted as a superposition of spectra from a mixture of incommensurate domains in which hybridization is weak and commensurate domains in which hybridization is similar to that in the homobilayer.

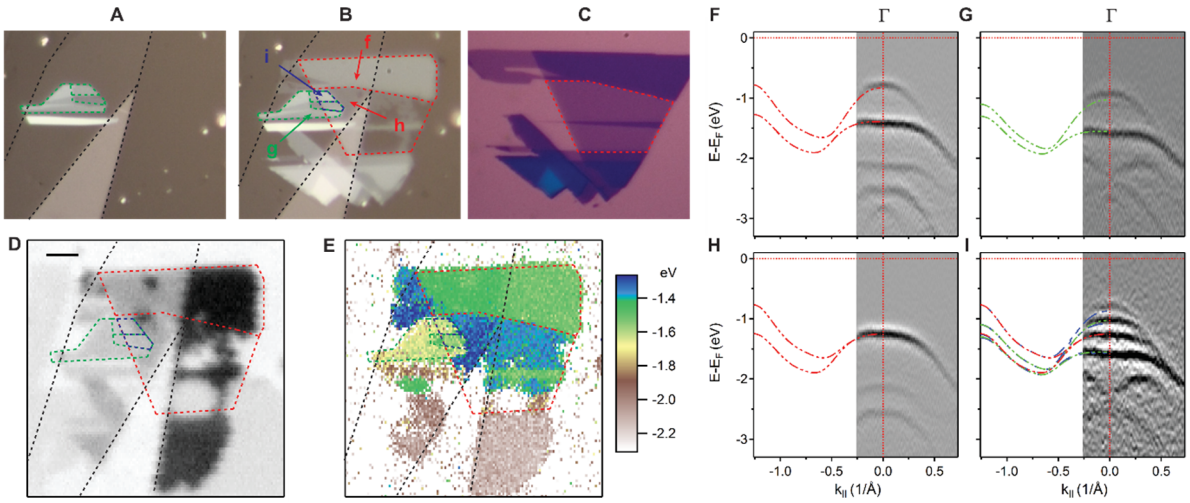

Figure 2.5. Bands in a 2D multi-layer heterostructure. **A-C**, optical images of: (**A**) $MoSe_2$ (outlined by dashed green line) on graphene (dashed black line) on the stamp; (**B**) WSe_2 (dashed red line), $MoSe_2$ and graphene on the stamp (heterostructure region outlined in blue), and (**C**) the exfoliated WSe_2 flake on SiO_2 prior to transfer. **D**, integrated SPEM map at **Γ** near E_F; scale bar is 5 μm. **E**, corresponding map of the energy of maximum emission. **F-I**, the dispersion around **Γ** from points in the bilayer WSe_2, bilayer $MoSe_2$, monolayer WSe_2, and the hetero-trilayer (bilayer $MoSe_2$ on monolayer WSe_2) regions respectively (labeled in **B**) with corresponding DFT calculations overlaid: for the hetero-trilayer the independent layers (monolayer WSe_2 red dashed, bilayer $MoSe_2$ green dashed) and commensurate hetero-trilayer (blue dashed) are both shown. These dispersions are not along high symmetry directions as sample drift during acquisition was too quick to acquire full $\boldsymbol{E-k}$ spectra in each region.

In support of this interpretation, first, DFT simulations of the commensurate heterobilayer reproduce the uppermost band at **Γ** (blue lines in Figure 2.4**C**) and the slightly downward shifted lower band. Adding the hybridized bands of the isolated $MoSe_2$ and WSe_2 monolayers (green and red respectively) reproduces the three apparent bands in H fairly closely. The remaining small discrepancy can be accounted for by shifts of order 100 meV in the incommensurate case, roughly independent of twist angle[147], as predicted by linear-scaling DFT. Additionally, in an intentionally misaligned (by ~30°) $MoSe_2/WSe_2$ heterobilayer, where no commensuration is expected, we saw only two bands near **Γ**. This is illustrated in Figure 2.4**D**. The band shifts in the twisted heterobilayer are well matched by DFT predictions for incommensurate layers. Furthermore, in a sample with an aligned bilayer of $MoSe_2$ on a monolayer of WSe_2 we observed four bands at **Γ** rather than three (Figure 2.5). The combined evidence is therefore compelling that aligned heterobilayers comprise mixtures of incommensurate and commensurate domains.

The values of key parameters extracted from the μ-ARPES measurements are summarized in Figure 2.6. They were consistent across multiple samples and showed no dependence on the orientation of the graphene cap or graphite substrate. The spin-orbit splitting, Δ_{SO}, at **K** is 0.49 ± 0.03 eV in WSe_2 and 0.24 ± 0.03 eV in $MoSe_2$, in agreement with the literature[141] as are the effective masses of holes at **Γ** and **K**. In monolayer WSe_2 we find $E_K - E_\Gamma = 0.50 \pm 0.03$ eV, consistent with scanning tunneling spectroscopy results[148]. In monolayer $MoSe_2$ we find $E_K - E_\Gamma = 0.44 \pm 0.03$ eV. We also record here the valence band width, D, which is useful for comparison with band structure calculations[141]. As is well known, in both monolayer species the valence band edge is at **K** whereas in the bulk it is at **Γ**. In the heterobilayer we find that the valence band edge is also at **K** and is higher than the maximum at **Γ** by 0.14 ± 0.03 eV. We measured a valence band offset between the WSe_2 and $MoSe_2$ monolayers of $\Delta_{VBO} = 0.30 \pm 0.03$ eV. Since

the bands at **Γ** in H (Figure 2.4**C**) align well with those in the separate monolayers, we infer that this value is an intrinsic parameter of the heterojunction, and that any charge transfer between the layers has negligible effect on the measurement.

Since we cannot probe the conduction band in these samples, we show the conduction band edges at **K** (red dashed line) and **Q** (blue dashed line) calculated by DFT. Although DFT

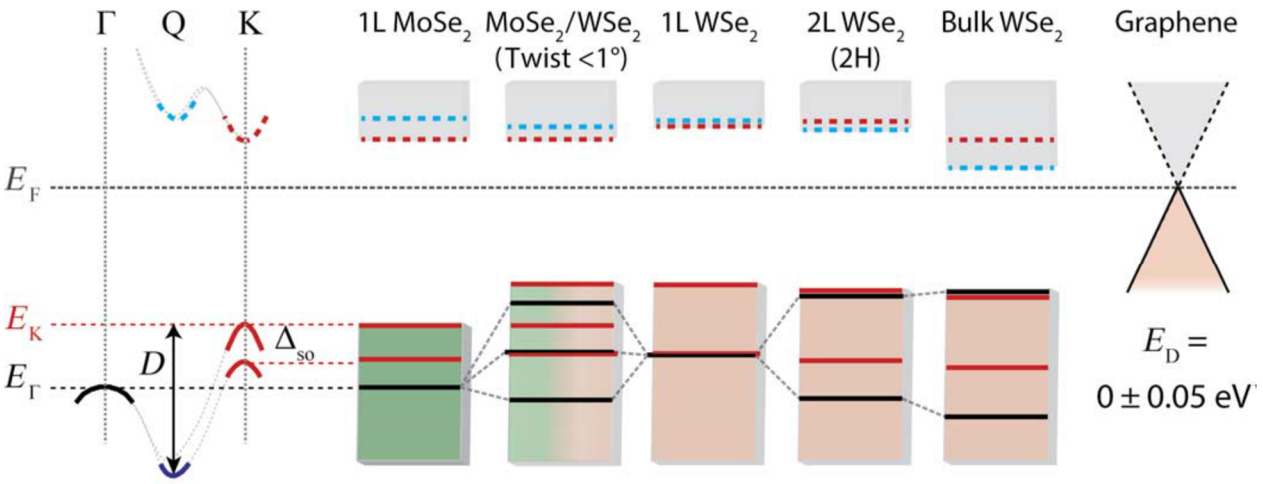

E_K (eV)	−0.99	−0.70	−0.70	−0.74	−0.79	±0.05
$E_K - E_\Gamma$ (eV)	0.44	0.14	0.50	0.04	−0.04	±0.03
Δ_{so} (eV)	0.24	–	0.49	0.50	0.50	±0.03
D (eV)	0.90	1.25	1.24	1.20	1.24	±0.03
m^*_K / m_0	–	0.4	0.4	0.5	0.4	±0.1
m^*_Γ / m_0	4.2	1.2	2.8	1.9	0.9	±0.2

Figure 2.6. Summary of measured band parameters. Left: schematic defining parameters applicable for monolayers and aligned bilayers. Solid lines signify measured quantities, dotted lines DFT calculations. Main: graphical illustration of the positions of homologous band edges and hybridization effects. In both 2L WSe_2 and heterobilayer $MoSe_2/WSe_2$, hybridization is almost undetectable at **K** (red) but much larger at **Γ** (black). Below: table of quantities determined by fitting the μ-ARPES spectra shown in Figure 2.2 and Figure 2.4. Energies are from Lorentzian fits to the second-derivative curves. The effective masses, which within the accuracy of the fits are isotropic, are obtained from weighted parabolic fits to the above band positions in symmetric windows about **K** and **Γ** of width 0.08 $Å^{-1}$ and 0.15 $Å^{-1}$ respectively.

underestimates these energies, the predictions of variations within the family of materials and across the Brillouin zone are more reliable[69,141]. The conduction band edge in H is predicted to remain at the **K**-point, which taken with our measurements implies that the band gap in H is direct.

2.4 Interlayer exciton binding energy

We can gain important insights into exciton binding by combining these results with optical measurements. Photoluminescence measurements were performed using ~30 μW of 532 or 632.8 nm continuous-wave laser excitation in reflection geometry, with the signal collected by spectrometer and Si CCD. Figure 2.7**A** shows a photoluminescence spectrum from an aligned $WSe_2/MoSe_2$ heterobilayer sample at room temperature. Below it is a plot of the peak positions for 13 similar samples. There are three peaks, whose origins are indicated schematically in Fig. 4B. X_{M} and X_{W} are the intralayer excitons formed by an electron and a hole in bands from the same layer, either $MoSe_2$ or WSe_2, respectively. Their energies $\hbar\omega(X_{\mathrm{M}})$ and $\hbar\omega(X_{\mathrm{W}})$ are almost coincident with the corresponding valley excitons in the isolated monolayers, consistent with the observation that the band-edge states near the K-points hybridize little. This implies that the binding energy of intralayer excitons in one layer is insensitive to the presence of the other layer. The third peak is the interlayer exciton, X_{I}. The small (~2%) variation of $\hbar\omega(X_{\mathrm{I}})$ between samples could be due to variations in substrate doping or twist angle.

According to Figure 2.7**B**, the energy difference between the intra- and interlayer excitons has two contributions: the difference in their binding energies, $\delta E_{\mathrm{b}} = E_{\mathrm{b}}\,(X_{\mathrm{M}}) - E_{\mathrm{b}}\,(X_{\mathrm{I}})$; and the valence band offset, such that $\hbar\omega(X_{\mathrm{M}})$ and $\hbar\omega(X_{\mathrm{W}}) = \Delta_{\mathrm{VBO}} - \delta E_{\mathrm{b}}$. The uniformity of $\hbar\omega(X_{\mathrm{I}})$ is consistent with Δ_{VBO} being an invariant parameter of the heterojunction. Hence, by combining optical and ARPES measurements made at the same temperature, we can deduce the magnitude of $\delta E_{\mathrm{b}} = \hbar\omega(X_{\mathrm{I}}) - \hbar\omega(X_{\mathrm{M}}) + \Delta_{\mathrm{VBO}}$. Averaging over the samples we get $\hbar\omega(X_{\mathrm{I}}) - \hbar\omega(X_{\mathrm{M}}) = 0.22$

± 0.02 eV, at 300 K. At 105 K it is slightly larger, by about 0.03 eV. Then using $\Delta_{VBO} = 0.30 \pm 0.03$ eV from above gives $\delta E_b = 0.05 \pm 0.04$ eV. That the X_I is more weakly bound than X_M is not surprising because the electron and hole in different layers are on average further apart. The values of E_b found in similar monolayers in the literature range from ~0.3 to 0.7 eV[74,75,149–154],with a report of 0.55 eV for $MoSe_2$[74]. We deduce that the interlayer binding energy $E_b(X_I) = E_b(X_M) - \delta E_b$ is at least ~0.2 eV. This is an order of magnitude larger than the binding energy of spatially indirect excitons in GaAs/AlGaAs double quantum wells.

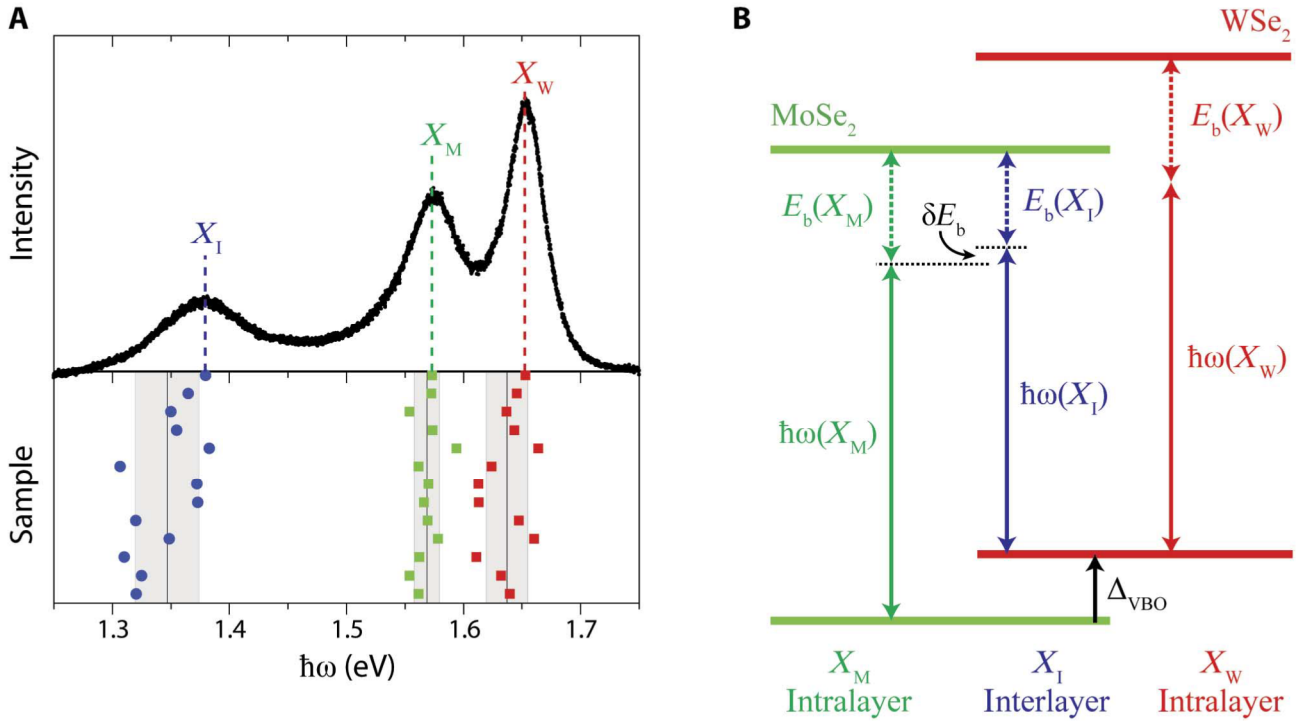

Figure 2.7. Photoluminescence and exciton binding in aligned heterobilayers. **A**, Above: representative PL spectrum showing peaks due to intralayer (X_M and X_W) and interlayer (X_I) excitons (2.33 eV excitation at 20 μW). Below: peak positions for 13 samples, implying that the energy of X_I is 220 ± 20 meV below that of X_M. **B**, Energy diagram showing the connection between the three exciton energies and the levels derived from the $MoSe_2$ and WSe_2 conduction and valence bands at the **K** points.

2.5 Discussion and summary

The results described above establish the key electronic parameters of $MoSe_2$-WSe_2 heterobilayers. The hybridization effects at **Γ** provide the first evidence for commensurate domains in such heterostructures, suggesting the possibility of band engineering by layering similar to that discussed in the context of graphene on hBN. Confirmation of this explanation will however require further research, such as higher resolution ARPES measurements showing the absence of hybridization of bands from the spatially separated domains. The observations that the valence band edge remains at the **K**-point and that the band alignment is type II are both significant for electronic and optoelectronic applications.

Electron doping is required to probe the conduction band of insulators by ARPES. The samples discussed here are undoped but as we shall discuss in the next chapter, the sample design used offers the possibility of gate doping in-situ in the ARPES chamber. In cases where the bands of the graphene cap may obscure features near the Fermi energy the graphene can be replaced with monolayer hBN, which is equally effective but both harder to prepare and to work with.

It is thus clear that the technique of μ-ARPES combined with careful sample design provides invaluable information for realizing the potential of 2D semiconductor heterostructures. It will also enable determination of the local electronic structure and chemical potential in all manner of other 2D materials and devices.

Chapter 3. ELECTROSTATIC GATING EFFECTS IN 2D HETEROSTRUCTURE DEVICES

Having established a sample fabrication protocol to overcome an apparent limitation in spectral resolution of μ-ARPES with 2D heterostructures, it is prudent to tackle another, more fundamental limitation: ARPES probes only occupied electron states. A semiconductor sample must therefore be electron-doped to produce a signal from the conduction band. This is usually achieved by depositing electropositive atoms such as alkali metals[6–8,13] on the surface. This process cannot be controlled accurately and can only be reversed by high temperature annealing. Moreover, it chemically perturbs the electronic structure and introduces disorder through the random distribution of dopants. An alternative is pump-probe measurement, where electrons are excited to previously-unoccupied states before photoemission[155]. While this technique can probe conduction band states, for example, with effectively zero net doping, it fundamentally studies nonequilibrium states.

A unique facet of 2D research is that with the addition of appropriate metal electrodes, 2D heterostructures become 2D devices wherein local electric fields can be applied to the entirety of a layer of interest to, for example, controllably and reversibly dope it. If the sample design discussed in Chapter 2 could be adapted to make μ-ARPES-compatible devices, effects of doping and of the applied electric field itself on band structure throughout the device could be directly visualized without the disadvantages of the conventional doping techniques.

This chapter will demonstrate exactly this, reprinting work from **Nguyen, P. V.** *et al.* Visualizing electrostatic gating effects in two-dimensional heterostructures. *Nature* **572**, 220–223 (2019)[156]. Also to be discussed is more recent work from Teutsch, N. C.*, **Nguyen, P. V.***, *et al.* Field-dependent band-structure measurements in two-dimensional heterostructures (in prep.).

3.1 Proving approach and sample design via gating graphene

We first demonstrate and validate the technique using monolayer graphene, which has an exquisitely well understood band structure even when doped. In our graphene devices, a graphene sheet is capped by monolayer hBN, supported on a BN flake over a graphite gate (Fig. 3.1**A**), and located in a gap between two platinum electrodes on an SiO_2/Si substrate chip (Fig. 3.1**B**, **C**). The gate is contacted to the smaller electrode, and the graphene to the larger electrode which functions as a grounding plane to minimize stray electric fields that may distort the electron trajectories. A similar structure with two contacts to the graphene would function as a high-mobility transistor[26].

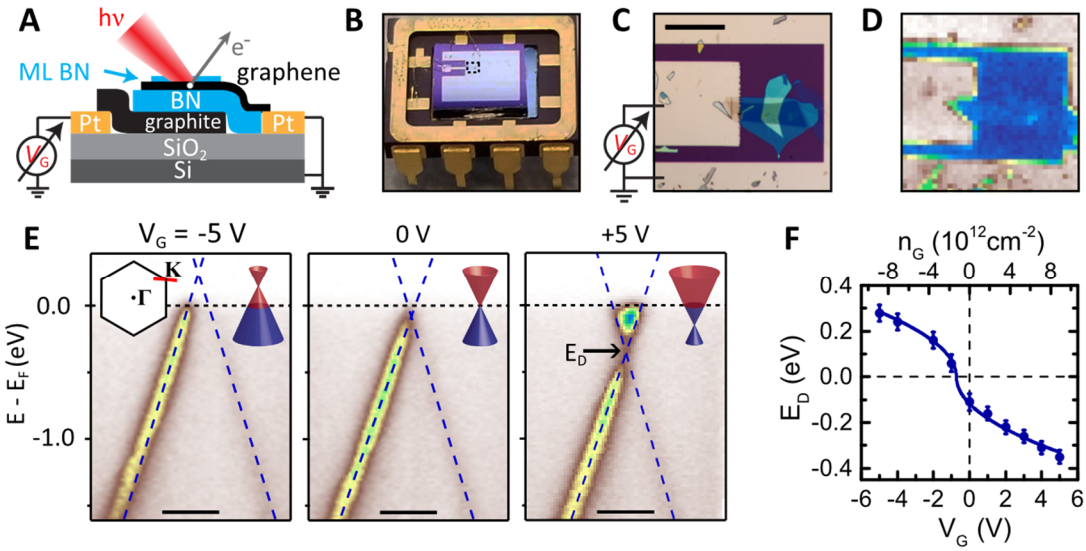

Figure 3.1. Visualizing electrostatic gating of monolayer graphene. **A,** Schematic of a device with a stack comprising graphene encapsulated by BN on a graphite back gate. The addition of ML hBN sharpened the graphene spectra which otherwise remained comparable to spectra from uncapped samples. The graphene is grounded while a voltage V_G is applied to the gate. **B**, Optical image of a device mounted in a standard DIP. **C**, optical zoom on the dotted box in **B** and **D,** SPEM image of the same area (scale bar, 50 μm). **E,** E - k slices near the graphene **K**-point, along the red line in the inset Brillouin zone, at the labelled V_G. The dashed lines are linear dispersion fits; the Dirac point energy E_D is deduced from their crossing (scale bars, 0.2 $Å^{-1}$). **F**, gate dependence of E_D, with error bars from MDC fits. The solid line is a fit based on the dispersion of graphene, with the gate-induced electron density n_G (top axis) calculated from the capacitance.

To minimize polymer contamination of the device surface, the substrates are pre-patterned with electrodes of ~30 nm Pt on a 5 nm Ti sticking layer. Pt is chosen for its high maximum annealing temperature (at least 400° C). Residual PMMA residue is removed by O_2 plasma treatment (50W, 15 minutes). The device is melted down onto the substrates and solvent and AFM-cleaned. The substrates are then mounted in ceramic eight-pin dual-inline packages (DIP, Kyocera SB008AK959-1) using low-outgassing, high-temperature compatible silver epoxy (EPO-TEK H20E). To minimize the annealing time in UHV, the packages are cleaned with IPA, then annealed in low vacuum at 300° C for two hours before the substrates are mounted. After mounting, the assembly is annealed again in low vacuum to cure the epoxy. Bare wire is wrapped around the package pins, fixed using the epoxy, and used to contact to leads on the ARPES sample mount.

ARPES measurements were done also at Spectromicroscopy under similar conditions as discussed in Chapter 2. Photon energy is 74 eV. Voltages are applied, and current is measured via a sourcemeter. SPEM is used to locate the sample in the ARPES chamber (Figure 3.1**D**). Figure 3.1**E** shows energy, E - E_F, vs momentum for a slice through the Dirac cone near the graphene zone corner **K**, acquired at a series of gate voltages V_G at 105 K. As expected, the Dirac point energy E_D shifts from above E_F at V_G = -5 V to below it at +5 V. Fitting a linear dispersion, $E(\boldsymbol{k}) = E_D \pm \hbar v_F \boldsymbol{k}$ (dashed lines), gives E_D and the Fermi velocity v_F at each voltage.

The variation of E_D with V_G is plotted in Figure 3.1**F** and is consistent with the expected form (solid line) given graphene's linear dispersion. To see this, it is useful to consider gate-induced doping n_G, which is expected to follow

$$n_G = \frac{C_g}{e}(V_G - \Delta V - \Delta\mu/e) \tag{3.1}$$

where ΔV is the voltage drop to ground from the sample under the ARPES beam due to photodoping, $\Delta\mu = \Delta(E_F - E_D)$ is the chemical potential change due to gate doping, and C_g is

the geometric capacitance. For graphene, the resistance R < ~1 kΩ and the maximum sourced current <2 nA, thus ΔV < ~2 μV which is negligible. $\Delta\mu$ can be found from the spectrum at each voltage to an accuracy of ~20 meV. In the measurements in Figure 3.1, $\Delta\mu/e$ is at least ten times smaller than V_G. Thus $n_G \approx C_g V_G$ (accurate to within 10%). As $k_B T = 9$ meV $\ll E_D$, from the conical Dirac dispersion one expects[35] $E_D^2 \approx \pi\hbar^2 v_F^2 (n_0 + n_G)$, where $n_G = CV_G$ is the induced 2D electron density, C the areal capacitance, and n_0 the residual electron density at $V_G = 0$.

The solid line in Figure 3.1**F** is a fit to this model with C and n_0 treated as fitting parameters. The value of n_0 obtained is $(1.8 \pm 0.1) \times 10^{12}$ cm^{-2}, implying a somewhat high residual doping that may be due to residual contamination. The value of C is $(2.2 \pm 0.2) \times 10^{-7}$ Farad cm^{-2}, consistent with the geometrical capacitance, $(\varepsilon_0 \varepsilon_{BN})/d_{BN} = (2.5 \pm 0.2) \times 10^{-7}$ Farad cm^{-2}, derived from the BN thickness, $d_{BN} = 14 \pm 1$ nm, measured by atomic force microscopy, and the dielectric constant, $\varepsilon_{BN} = 4.0$, taken from the literature[36–38]. Note also that the intensity near E_D is weak because these E - k slices do not pass exactly through **K**. The much lower intensity on one side of the cone corresponds to the graphene corridor (destructive interference between sublattice sites[39]).

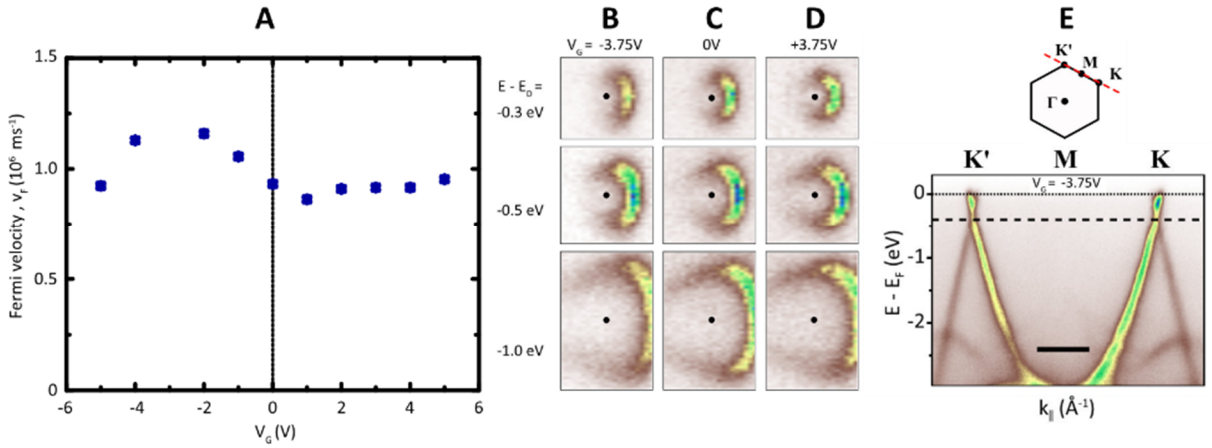

Figure 3.2. Gate dependence of graphene spectra. **A**, extracted graphene Fermi velocity vs. gate voltage V_G showing weak dependence. **B-D**, constant energy slices through the Dirac cone at different energies with no significant change with V_G. Panels are 4 Å-1 wide. **E**, E – k slice through **K** and **K'**, showing symmetric spectrum without gate-induced distortions.

Finally, we find $v_F = 9.3 \pm 0.1 \times 10^5$ ms^{-1} at $V_G = 0$, with a weak V_G dependence (Figure 3.2**A**). Evidence has previously been reported[157] of a reduction of v_F by up to 20% near E_D in graphene films at low doping levels (~1 × 10^{12} cm^{-2}). However, this corresponds to a subtler distortion of the Dirac cone than can be resolved by the spectrometer at Spectromicroscopy. Rather, the variations observed here might be explained by experimental limitations such as the very weak emission from one branch and the sensitivity to the exact alignment of the momentum slice with the Dirac point. No modification of the dispersion near E_D which could arise due to interactions, is detectable with the system spectral resolution (Fig. 3.2**B-E**). The consistency of the above properties with the graphene literature, together with the observation that the spectrum is undistorted as V_G is changed, implies that the photoelectron trajectories are not affected by stray electric fields due to the gate voltage or charging effects. We conclude that the technique produces accurate local electronic spectra during live electrostatic gating.

3.2 Visualizing the conduction band of 2D TMDs by gating

To study gate-doping of 2D semiconductors, we incorporate a TMD flake into the stack on top of the BN, partially overlapping graphene that acts as a contact to it (Fig. 3.3**A**). Figure 3.3**B** and **C** are optical and SPEM images of Device 1, which has a WSe_2 flake that has monolayer (ML), bilayer (2L) and trilayer (3L) regions. 27 eV excitation was used over 74 eV, as it produces more photoemission from the **K** valleys. Sample stage temperature was 100K. Figure 3.3**D-E** are momentum slices obtained with the beam spot on each of the regions, respectively, along **Γ** - **K** of the WSe_2 Brillouin zone at 100 K (Fig. 3.3**G**, inset). As expected, at $V_G = 0$ (upper row) only the valence bands can be seen. Their evolution with layer number is consistent with the literature[27] and matches the overlaid theoretical predictions (GW approximation, Appendix) well. At V_G = +3.35 V (lower row) an additional spot appears near E_F. The size of this conduction band feature

is determined solely by instrument resolution, and the dispersion cannot be resolved. However, its intensity is maximal near the graphene contact, possibly due to electrostatics. In ML WSe_2 the spot is located at **K**, whereas in 2L and 3L it is at **Q** (Fig. 3.3**G**). This is consistent with evidence from photoluminescence[25] that the gap is direct at **K** in the monolayer but indirect for 2+ layers.

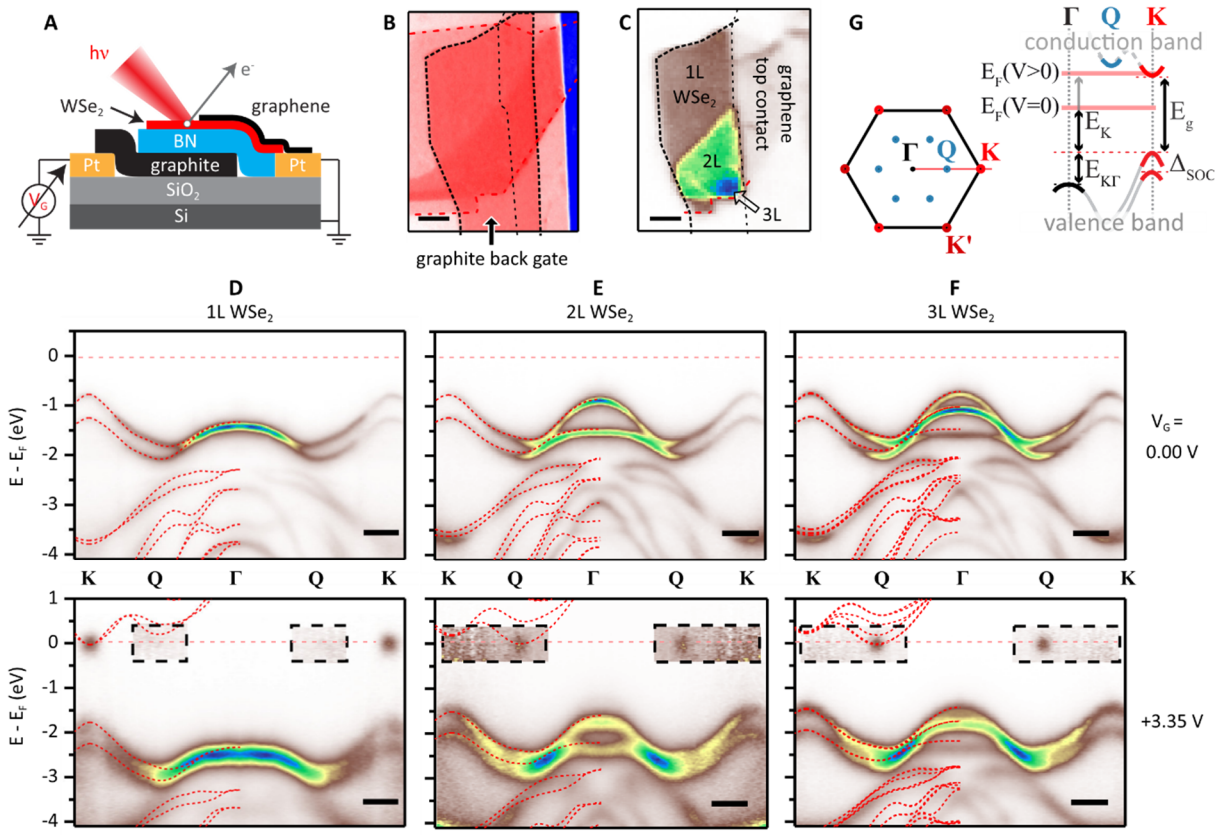

Figure 3.3. Layer-number dependent conduction band edge in WSe_2. **A**, Schematic of a device incorporating a WSe_2 flake with overlapping graphene top contact grounded and gate voltage V_G applied to the graphite back gate. **B**, Optical and **C**, SPEM images of WSe_2 Device 1 (d_{BN} = 7.4 ± 0.5 nm), with monolayer, bilayer and trilayer regions identified (scale bars, 5 µm). **D-F,** energy-momentum slices along **Γ - K** for ML, 2L, and 3L regions respectively. The upper panels are at V_G = 0 and the lower ones at V_G = +3.35 V. The intensity in the dashed boxes is multiplied by 20. The fuzzy spots signal population of the CBE. Scale bars, 0.3 $Å^{-1}$. The data have been reflected about **Γ** to aid comparison with electronic structure calculations (GW approximation, see Appendix) (red dashed lines). **G**, Brillouin zone of TMD, and schematic of bands along **Γ - K** showing definitions of the energy parameters discussed in the text.

Table 3.1. **Measured band structure parameters of TMDs.** As defined in Figure 3.3**G**, Δ_{SOC} is the valence band spin-orbit splitting at **K**; E_K is the valence band edge at $V_G = 0$; $E_{K\Gamma} = E_K - E_\Gamma$ is the difference between the valence band edges at **K** and **Γ** at $V_G = 0$; m_K^* is the effective mass of the valence band edge at **K** in units of the free electron mass m_e; and E_g is the band gap measured at gate-induced electron density $n_G = 1.0 \pm 0.2 \times 10^{12}$ cm^{-2}. The stage temperature was 100 K for the WSe_2 and 105 K for the others.

	Δ_{SOC} (eV)	E_K ($V_G = 0$) (eV)	$E_{K\Gamma}$ ($V_G = 0$) (eV)	m_K^*/m_e	E_g (eV)
ML MoS_2	0.17 ± 0.04	1.93 ± 0.02	0.14 ± 0.04	0.7 ± 0.1	2.07 ± 0.05
ML $MoSe_2$	0.22 ± 0.03	1.04 ± 0.02	0.48 ± 0.03	0.5 ± 0.1	1.64 ± 0.05
ML WS_2	0.45 ± 0.03	1.43 ± 0.02	0.39 ± 0.02	0.5 ± 0.1	2.03 ± 0.05
ML WSe_2	0.485 ± 0.010	0.80 ± 0.01	0.62 ± 0.01	0.42 ± 0.05	1.79 ± 0.03
2L WSe_2	0.501 ± 0.010	0.75 ± 0.01	0.14 ± 0.01	0.41 ± 0.05	1.51 ± 0.03 *
3L WSe_2	0.504 ± 0.010	0.74 ± 0.01	0.00 ± 0.01	0.40 ± 0.05	1.46 ± 0.03 *

*indirect, with CBE at **Q**

Table 3.1 shows the band parameters for ML–3L WSe_2 as well as for other monolayer TMD species, derived[15] from measurements on this and other devices (Fig. 3.4). The band gap, $E_g = E_C - E_K$, where E_C is the energy of the CBE, was determined at a doping level of $n_G \approx 10^{13}$ cm^{-2} for which $E_F - E_C \sim 30$ meV. We also list the simultaneously determined hole effective mass m_K^*, valence band edge E_K, spin-orbit splitting Δ_{SOC}, and $E_{K\Gamma}$ as defined in Figure 3.3**G,** all measured for the first time on an hBN substrate and with greater precision than in previous reports.

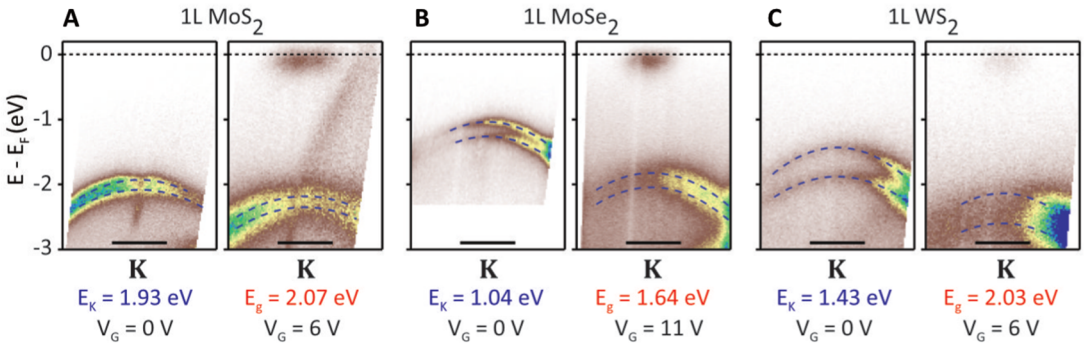

Figure 3.4. Conduction band edges in other ML TMDs. **A-C**, E - k slices through **K** for ML MoS_2, $MoSe_2$, and WS_2, respectively. Linear dispersion in **A** due to partial overlap with graphene capped region. Scale bars are 0.3 Å^{-1}.

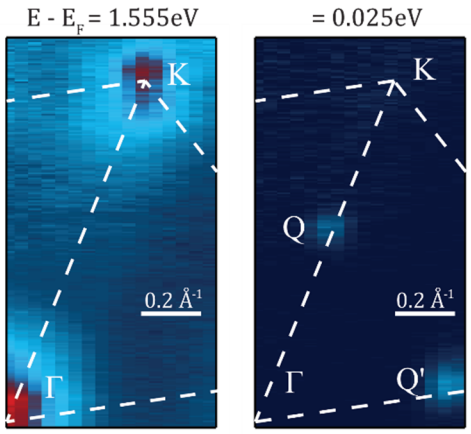

Figure 3.5. Uniform band shifting in electrostatically gated 2L WSe_2. Constant energy maps of gated 2L WSe_2 at $V_G = +8$ V, (left) at a binding energy of 1.555 eV which corresponds to the valence band maximum, and (right) near E_F at a binding energy of 0.025 eV. The conduction band energy is the same at **Q** and **Q'**, implying that the gate field does not significantly distort the spectrum in this case.

It is worth verifying that the gating process does not distort the TMD spectra. Figure 3.5 shows two constant energy slices from 2L WSe2 doped to the CBM at Q/Q' ($V_G = +8$ V through $d_{BN} = 24.5 \pm 0.5$ nm. The first slice is through the 2L WSe2 VBM, and allows determination of the hexagonal Brillouin zone. The second slice is very nearly at E_F, and shows small bright spots from the CBM at Q and Q'. Their energetic alignment to each other, and angular alignment to the valence band feature at K implies that the gate field is not generating significant distortion.

3.3 Band gap renormalization in the low doping regime

We can now consider gate dependence of the spectra in detail. The lower left of Figure 3.6 shows the behavior of the top of the valence band at **Γ**, where the photoemission signal is strongest, for monolayer WSe_2 Device 2. At low V_G (range labelled **B-C-D**) the spectrum shifts nearly linearly with a slope -1/*e*, where *e* is the electron charge, implying that the electrostatic potential in the WSe_2 tracks the gate potential when it is undoped. For V_G > +2.1 V (**E**) or < -1.5 V (**A**) it becomes almost independent of V_G, implying that these are the thresholds for electron and hole accumulation, respectively. The behavior can be understood with reference to the corresponding band diagrams (above), taking into account the balance of photoemission current, I_{PE}, the currents into the beam spot from the contact, I_C, and the gate, I_G, as indicated in the sketch at the top left.

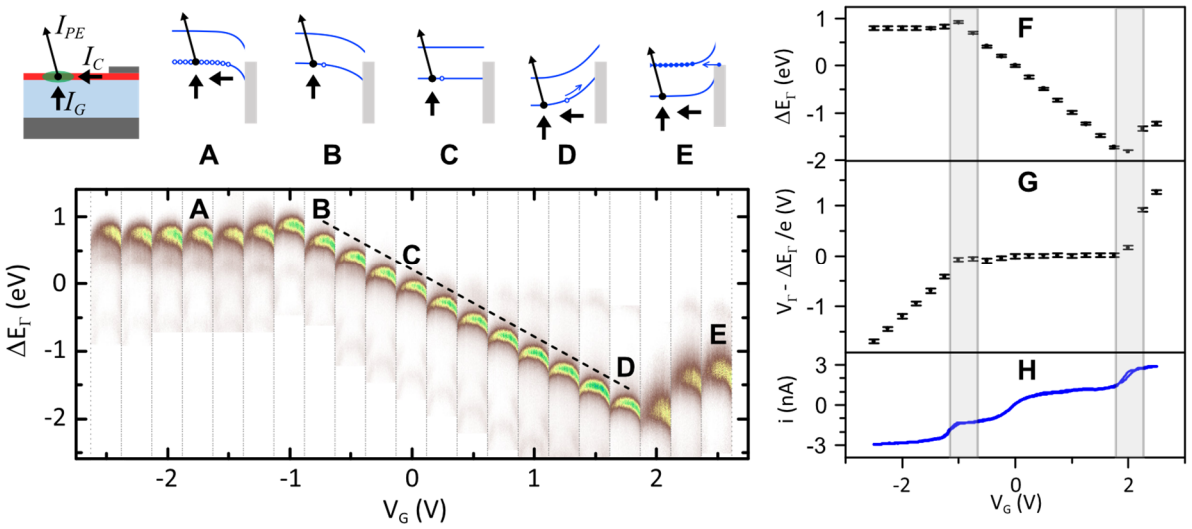

Figure 3.6. Electrostatic gating of monolayer WSe_2. (Bottom left) Each vertical strip is an energy-momentum slice, 0.6 $Å^{-1}$ wide, through **Γ** in WSe_2 Device 2 (d_{BN} = 6.0 ± 0.5 nm) measured at the gate voltage shown on the bottom axis. ΔE_Γ is the photoelectron kinetic energy measured relative to the Γ-point maximum at $V_G = 0$. The dashed line has slope -1/*e*. Above left is a device schematic indicating the photoemission current I_{PE} from the beam spot, current I_C from the graphene contact, and current I_G from the gate through the BN due to photoconductivity. The schematic band diagrams (top left) indicate the situations at the gate voltages labelled **A-E**. The gray rectangle is the graphene Fermi sea, the blue lines are the WSe_2 conduction and valence band edges, and the smaller arrows indicate when I_G and I_C are significant. **F**, ΔE_Γ vs V_G for WSe_2 monolayer Device 2. **G**, V_G - $\Delta E_\Gamma/e$ vs V_G. **H**, current i from gate to ground vs V_G. The grey shaded regions indicate the threshold regions in which the WSe_2 becomes conducting.

At small V_G, the doping n_G must be very small because of the band gap, so the in-plane resistance can be large and ΔV can be substantial. As long as n_G is negligible, ΔV can be identified with the purely electrostatic energy shift of an ARPES spectral feature. $\Delta E_\Gamma/e$ in Figure 3.6 indeed tracks V_G closely at low V_G (Fig. 3.6**F**,**G**). We deduce that in this regime photoemission directly from the hBN valence band generates photoconductivity in the hBN which is sufficient to keep the potential in the TMD close to that of the gate, i.e., $\Delta V \approx V_g$, with negligible potential drop across the hBN and no accumulation of charge in the TMD. In contrast, at a sufficiently large

magnitude of V_G, (V_G - $\Delta E_\Gamma/e$) tends towards a linear increase with V_G. This happens when the high doping makes in-plane resistance R small enough that the electrochemical potential in the TMD approaches that in the (ground) electrode and ΔV stops changing, with the Fermi energy virtually pinned at the band edge due to the large density of states. In this regime we can take

$$n_G = \frac{C_g}{e}(V_G - \Delta E_\Gamma/e) \tag{3.2}$$

since (V_G - $\Delta E_\Gamma/e$) is the static potential drop across the hBN, the electrons are in electrochemical equilibrium, and the quantum capacitance is negligible (i.e., E_F is effectively pinned at the CBE).

A full interpretation can thus be formed as follows. The currents I_{PE}, I_C, and I_G must sum to zero. I_G can be substantial because of photo-excited carriers in the hBN. (*n.b.,* in general such currents may cause a device to operate differently from how it would in the dark). Between **B** and **C**, the WSe_2 is depleted and insulating enough that the BN photoconductivity brings the potential close to that of the gate. Holes created by photoemission from the WSe_2 recombine with excited electrons in the BN, and $I_{PE} \approx I_G$. Between **C** and **D**, these holes can also drift to the contact through the depleted WSe_2, and I_C is significant. Above threshold, at **E**, electrons accumulate at the CBE in the WSe_2 as they flow in laterally from the graphene contact, and the CBE is pinned close to the graphene Fermi level. Similarly, at **A**, holes accumulate, and the valence band edge is pinned. An "overshoot" occurs at **D** because when the CBE in the beam spot first moves below the graphene Fermi level, the Schottky barrier between graphene and WSe_2 prevents electrons flowing in fast enough to accumulate.

Note that no change in spectral widths is seen as long as the WSe_2 is insulating (range **B-D**), but above threshold (range **D-E**) all features are smeared in energy by a similar amount. This can be explained by inhomogeneous broadening due to variation of the potential across the beam

spot associated with lateral current flow in the WSe_2. Refinement of the technique to reduce this effect may allow studies of changes in intrinsic broadening with doping.

Figure 3.7**A** shows spectra from monolayer WSe_2 Device 1 at $V_G = 0$ (for reference) and at selected gate voltages well above threshold (about +1.5 V). In this regime we derive the gate doping n_G, also shown, from Eq. 3.2 . The CBE becomes visible at **K** for $n_G > \sim 10^{12}$ cm^{-2} and at **Q** for $n_G > \sim 10^{13}$ cm^{-2}, when E_K is roughly 30 meV below E_F. We conclude that the conduction band minimum at **Q** is higher than that at **K**. Scanning tunneling spectroscopy (STS)[21] also indicates that for 1L WSe_2 these minima are very close. The form of the valence bands does not change

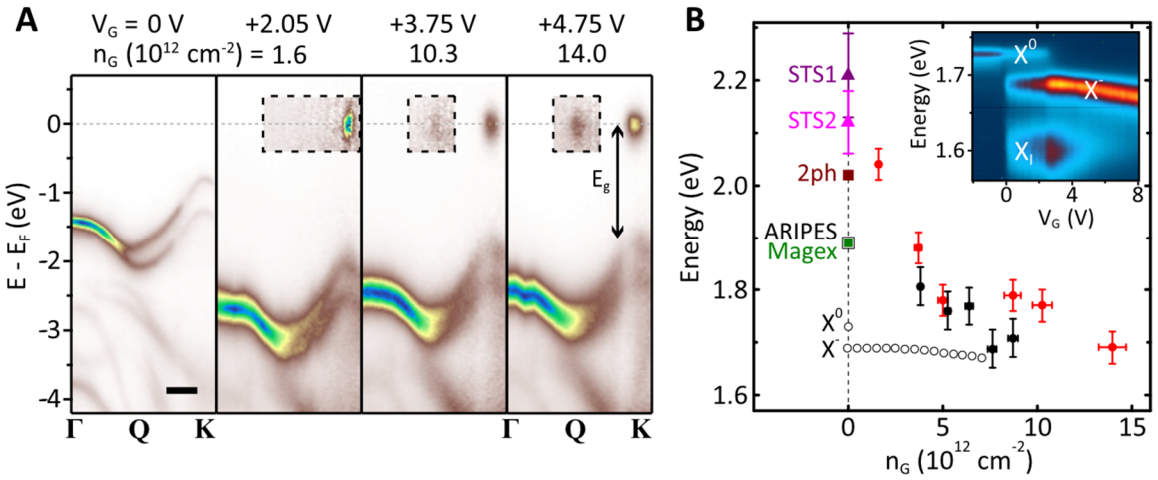

Figure 3.7. Renormalization of the band gap and comparison with PL. **A**, E - k slices along **Γ** - **K** for ML WSe_2 in Device 1 at a series of V_G, with doping n_G also shown (scale bar, 0.3 Å^{-1}). The intensity in the dashed box is multiplied by 20 at +2.05 V and by 40 at higher V_G. The definition of the band gap, E_g, is indicated. **B**, band gap dependence on n_G for Device 1 (red) and Device 3 ($d_{BN} = 4.5 \pm 0.5$ nm, solid black circles) at 100 K. Also plotted (black open circles) are the photoluminescence peak positions for the neutral exciton (X^0) and negative trion (X^-) in Device 3 at the same temperature. The inset shows the photoluminescence data, with an impurity-bound exciton peak X^I also labelled. The points at $n_G = 0$ are measurements of the gap from other techniques from the literature: STS1[20] (purple triangle) and STS2[21] (pink triangle) are from scanning tunnelling spectroscopy measurements, on graphite at T= 4.5 K and 77 K respectively; 2ph (brown square) is from two-photon absorption[22], on SiO_2 at 300 K; ARIPES (black open square) is from inverse photoemission[23], on sapphire at 300 K; and Magex (green solid square) is from magneto-optical measurements[24], encapsulated in BN at 4 K.

discernibly with increasing n_G but they shift upwards in energy while the CBE is pinned at E_F, implying that the band gap decreases.

Optical spectroscopy can be performed on the same devices, and under the same conditions, as the μ-ARPES measurements, eliminating uncertainties due to differences in sample quality, dielectric environment, gate voltage and temperature[28–30]. PL measurements were performed using ~20 μW linearly polarized 532 nm continuous-wave laser excitation in reflection geometry, with the signal collected by a spectrometer and a silicon CCD, in vacuum in a closed-cycle cryostat. Figure 3.7**B** shows both the μ-ARPES determination of E_g (black solid circles) and the PL peak positions (black empty circles), E_{X^0} and E_{X^-}, for neutral (X^0) and charged (X^-) excitons, for monolayer WSe_2 Device 3 as a function of gate doping at 100 K. Also shown are the values of E_g from Device 1 (red solid circles), which agree to within the uncertainty. It is apparent that E_g decreases systematically, by ~400 meV as n_G rises to 1.5×10^{13} cm^{-2}. Such renormalization of the band gap with static doping is expected to occur in a semiconductor as a result of free-carrier screening[31], though it has not previously been so accessible to experiments.

Also plotted in Figure 3.7**B** are values of the band gap at $n_G = 0$ inferred from several other techniques. An extrapolation of E_g measured by μ-ARPES to $n_G = 0$ is consistent with STS measurements which put it in the range 2.1-2.2 eV. Comparison with E_{X^0} supports arguments that the binding energy of neutral excitons is very large in WSe_2 28, at several hundred meV. E_g decreases much faster than E_{X^-} with doping, implying dramatic weakening of the exciton binding which is another expected effect of free-carrier screening[29]. Finally, the still smaller values of E_g reported in monolayers doped with alkali metals (down to 1.4 eV for 1L WSe_2) are consistent with an extrapolation of the renormalization process to higher n_G[7,8].

3.4 Field-dependent band alignment at the graphene/TMD interface

In electronic and optoelectronic devices made from 2D materials, electric fields may induce substantial band structure changes underpinning device operation. This is perhaps most practically important where the material of interest interfaces with its contact. As we have seen, graphene itself can function as a contact to TMDs. In fact, using graphene (or another 2D conductor) as a contact can be advantageous, as its finite density of states means its carrier density, and therefore its band alignment to, say, a TMD can be tuned by a gate voltage. Understanding to what degree this is possible, then, is vital to development of all-2D devices.

μ-ARPES can be applied to this question with the device geometry used in the previous subsection (Fig. 3.8**A**). Figure 3.8**B** is an optical image of Device 4, with the different layers outlined. Figure 3.8**C** shows the Brillouin zones of the graphene and ML WSe_2 and Figure 3.8**D** shows sketches of the bands along the three colored lines (in Fig. 3.8**C**) at the zone center (**Γ**, red), the zone corner of WSe_2 ($\mathbf{K_W}$, blue), and the zone corner of graphene ($\mathbf{K_{gr}}$, green line). The behavior of the spectra along these lines, as a function of gate voltage, is shown in the cubes in Figure 3.8**E-G**. On the front of each cube is an energy-momentum slice of the intensity $I(E, k_{\parallel}, V_{\mathrm{G}})$ along the respective momentum line at $V_{\mathrm{G}} = -6$ V. As V_{G} is varied each of these pieces of the spectrum shifts vertically with some broadening; the shift is seen on the side of the cube.

At each gate voltage we determined the WSe_2 valence band maximum at **Γ**, E_{Γ}, from a parabolic fit to the intense photoemission around **Γ**, and similarly E_{K} from the weaker photoemission around $\mathbf{K_W}$. The Dirac point energy, E_{D}, of the graphene was found from the crossing points of linear fits to each side of the conical graphene dispersion around $\mathbf{K_{gr}}$. We find $E_{\mathbf{\Gamma}} - E_{\mathbf{K}} = 0.55 \pm 0.05$ eV, and the spin splitting at $\mathbf{K_W}$ is $\Delta_{\mathrm{SOC}} = 0.48 \pm 0.03$ eV, consistent with our previous measurements[103,158] on ungated monolayer WSe_2. At $V_{\mathrm{G}} = 0$, the valence band

edge is at $E_K = 0.85 \pm 0.05$ eV, slightly higher binding energy than the value of 0.80 ± 0.01 eV from Table 3.1 where there was no top graphene. Since monolayer WSe_2 on BN has a direct gap[158] of approximately 2.1 eV, the chemical potential is deep in the gap of the WSe_2.

The variation of these band parameters with V_G is plotted in Figure 3.9**A**. The Dirac point moves downwards in an S-shaped manner as V_G is increased, as expected due to the vanishing density of states in graphene near the Dirac point[159]. The WSe_2 valence bands shift rigidly, with detectable changes in neither $E_K - E_\Gamma$ nor Δ_{SO}. They also follow an S-shape, but their overall shift in the same V_G range is larger. Figure 3.9**B** shows similar measurements done with Device 5, which had monolayer $MoSe_2$ instead of WSe_2. Spectra were only acquired from the $MoSe_2$ bands at **Γ**

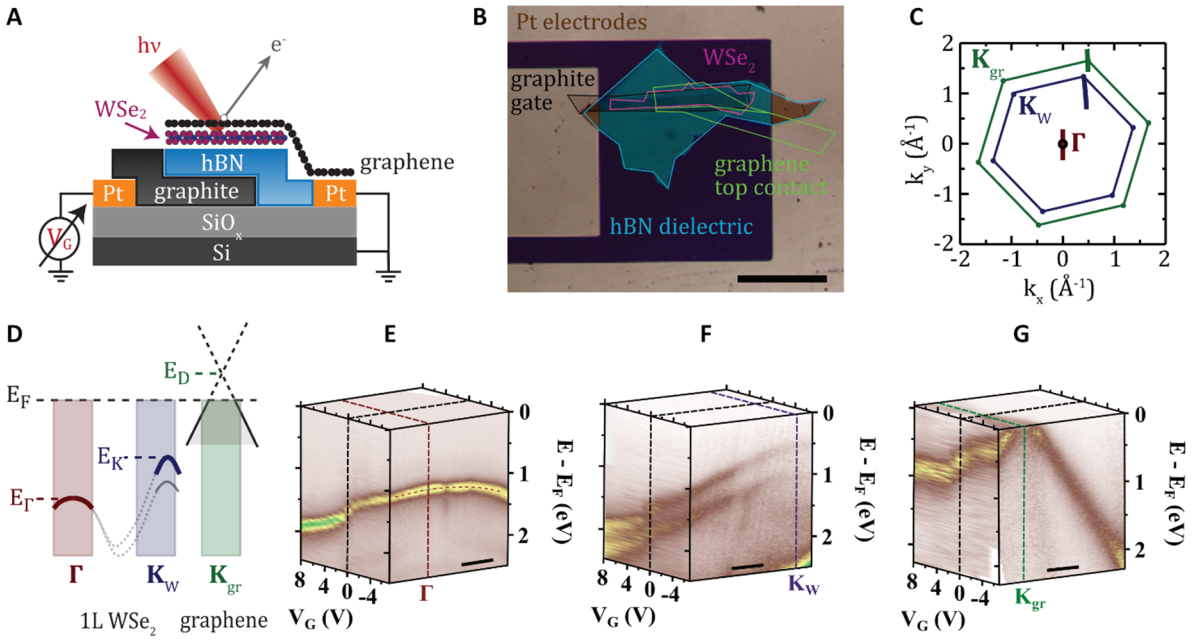

Figure 3.8. Gate-dependent valence band measurements in a 2D heterostructure. **A**, Schematic and **B**, optical microscope image of device 4, the scale bar corresponds to 50 µm. **C**, First Brillouin zones of the monolayer WSe_2 (blue hexagon) and graphene (green hexagon), with the positions of the energy-momentum slices marked as solid lines. **D**, Energy-momentum schematic of the band energies. **E**, Photoemission intensity as a function of energy, momentum, and gate voltage, $I(E, k_\parallel, V_G)$ around the Brillouin zone center; **F**, the zone corner of WSe_2; and **G**, and graphene; the scale bars correspond to $0.3 Å^{-1}$.

due to the low photoemission intensity at the zone corner. The band gap of $MoSe_2$ is similar to that of WSe_2,[158,160] so the higher position of E_Γ at $V_G = 0$ suggests n-doping of the $MoSe_2$, possibly due to intrinsic defects. Note that these measurements were made in UHV after annealing to remove atmospheric contaminants, and at low temperature (100 K) so that adsorbates and charge traps in the substrate are unlikely to contribute.[161]

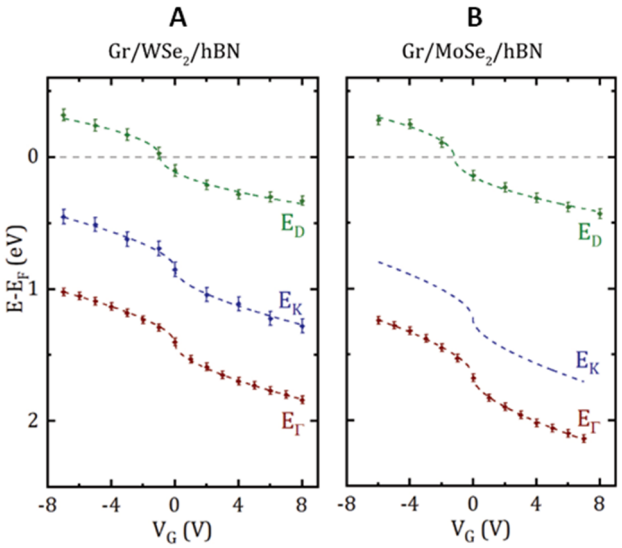

Figure 3.9. Gate-dependent band alignments across graphene on TMD. Band energies E_D (green), E_K (blue) and E_Γ (maroon) extracted from the data in Figure 3.8, plotted as a function of gate voltage, for **A**, graphene on monolayer WSe_2 and **B**, graphene on monolayer $MoSe_2$. The dashed lines are fits to the data as described in the text.

We interpret these shifts via schematic band diagrams, Figure 3.10**A** and **B**. At $V_G = 0$ (Fig. 3.10**A**), the graphene Dirac point E_D is very close to the Fermi level, i.e., $E_D = 0$, implying that the graphene is undoped and the electric field in the hBN is small. The position of the valence band edge E_K in the monolayer TMD is then defined to be E_{K0}. When a (positive) gate voltage V_G is applied to the graphite (Fig. 3.10**B**) the electric field increases, the graphene becomes doped with electrons to a chemical potential μ, measured relative to the Dirac point, and, since the Fermi energy is defined to be zero, E_D shifts to $-\mu$. The areal charge density is to a good approximation CV_G, where the geometric capacitance $C = \varepsilon_{BN}/D$ is dominated by the hBN with thickness D and dielectric constant $\varepsilon_{BN} \approx 4.5$, found in the previous subsection. Then $e\int_0^\mu n(E)dE \approx CV_G$, where $n(E) = n_{gr} + n_{gap}$ is sum of the density of states of the graphene, $n_g r = \frac{2}{\pi(\hbar v_F)^2}E$, and of possible

in-gap states in the TMD, n_{gap}. $\mu(V_G)$ can therefore only be calculated if n_{gap} is known. However, for the WSe_2 device, $d = 25.5 \pm 0.2$ nm and we obtain a good fit to the measurements of $E_{\mathrm{D}} = -\mu$ vs V_{G} by taking $n_{\mathrm{gap}} = 0$. From this we infer an upper bound on the density of in-gap states in the monolayer WSe_2 of $< 10^{11}\mathrm{cm}^{-2}$.

The shift of the TMD bands relative to the graphene Dirac point observed in Figure 3.9 is naturally explained by the gate electric field creating an electrostatic potential energy difference Δ between electron states localized on the WSe_2 layer and those localized on the graphene. This is

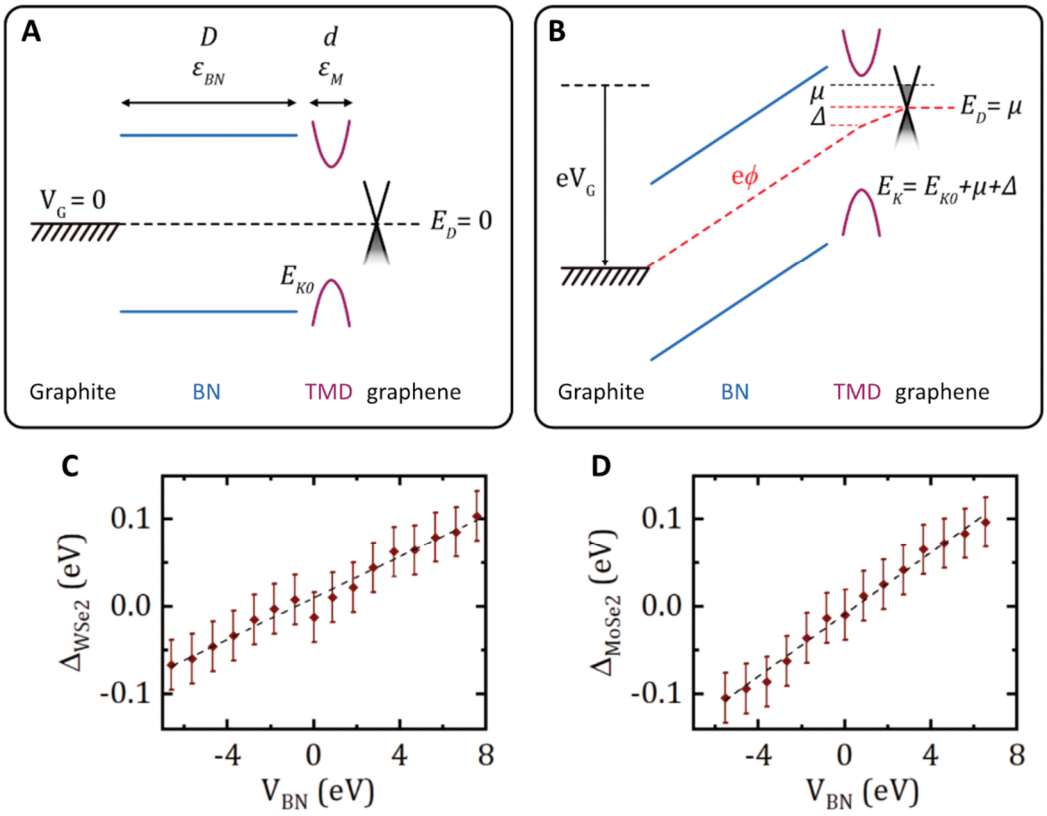

Figure 3.10. Gate-dependent electrostatic potential drop across the TMD layer. Schematics of the band edge energies across the heterostructure without applied gate voltage $V_{\mathrm{G}} = 0$ (**A**), and with applied gate voltage V_{G} (**B**). The electrostatic potential difference between states on the MX_2 and top graphene layer, determined from the band alignment data in Figure 3.9, plotted as a function of the electrostatic potential drop across the BN for WSe_2 (**C**) and $MoSe_2$ (**D**) heterostructures. The dashed lines are linear fits to the data.

indicated in the profile of the electrostatic potential ϕ, drawn in red superimposed on Figure 3.10**B**. For linear polarizability of the insulators, Δ will be proportional to the total potential drop ($V_{\mathrm{G}} - \mu/e$) between the graphite gate and the graphene, that is, $\Delta = \alpha(eV_{\mathrm{G}} - \mu)$, where α is a numerical constant. Therefore, $E_{\mathrm{K}} = E_{\mathrm{K0}} + \mu + \Delta = E_{\mathrm{K0}} + \mu + \alpha(eV_{\mathrm{G}} - \mu)$, and using $E_{\mathrm{D}} = -\mu$,

$$E_{\mathrm{K}} - E_{\mathrm{D}} = E_{\mathrm{K0}} + \alpha(eV_{\mathrm{G}} - E_{\mathrm{D}}). \tag{3.3}$$

Thus, plotting $E_{\mathrm{K}} - E_{\mathrm{D}}$ against $eV_{\mathrm{G}} - E_{\mathrm{D}}$ using the measured values of E_K and E_D should yield a straight line of slope α. Such plots are shown in Figure 3.10**C** and **D** for WSe_2 and $MoSe_2$, respectively. For the WSe_2 the linear fit shown yields $\alpha = 0.012 \pm 0.002$. Treating the BN and WSe_2 as dielectric slabs gives $\alpha = \frac{d}{D}\frac{\varepsilon_{\mathrm{BN}}}{\varepsilon_M}$, where d and ε_{M} are the effective thickness and perpendicular dielectric constant of the monolayer TMD. Taking $d^{\mathrm{WSe_2}} = 0.65$ nm[162–164], we get $\varepsilon_{\mathrm{WSe_2}} = (9.8 \pm 1.5)$ which is similar to prior reports for multi-layer WSe_2[165]. And for the $MoSe_2$, with $d^{\mathrm{MoSe_2}} = 0.65$ nm and $D = 19.0 \pm 0.5$ nm, we find $\varepsilon_{\mathrm{MoSe_2}} = (8.9 \pm 1.0)$.

3.5 Discussion and Summary

The results presented here demonstrate that ARPES with *in-operando* gating can probe device physics in 2D heterostructures. The ability to measure changes in the electronic bands throughout 2D field-effect devices opens up many interesting possibilities. For example, it could be used to study electric-field tuning of the bands across topological phase transitions[5]; to investigate the doping dependence of spectra in correlated electron systems such as in superconductors, Mott insulators, and charge-density-wave materials; to observe spectral reconstructions in structures with moiré superlattice modulations[32]; and, with the addition of circularly polarized light or a spin-resolved spectrometer, to study electrically controlled magnetic phenomena[33].

Chapter 4. BAND ALIGNMENTS AND REPLICA BANDS IN TWISTED 2D HETEROSTRUCTURES

A unique degree of freedom in designing 2D heterostructures is the interlayer rotational alignment, which can be set to arbitrary angles to produce nearly any desired incommensurate stacking. At such a twisted heterointerface, the electrons can feel the combined potential of the nearby layers – a moiré superpotential with longer spatial period than of the constituent crystals. The moiré periodicity from two similar lattices at small twist can alter the underlying optical and electronic properties. For graphene based superlattices many studies of high impact physics have been reported as the result of flat moiré bands driving strong correlations, such as magic-angle superconductivity[41], and tunable Mott insulator states[157]. More recently, moiré potentials have been exploited in heterostructures of TMDs to change their optical response, e.g. by localizing interlayer excitons[64,166,167]. Naturally, knowledge of the band structure in these systems is of paramount importance for substantiating and interpreting any observed novel phenomena.

This chapter will cover on-going work to apply μ-ARPES to such incommensurate 2D heterostructures to directly determine the effect, if any, of twisting on the combined electronic structure. All ARPES presented came from Spectromicroscopy with identical procedures as previously discussed. The discussion will be chronological, starting with observations of twist-dependent replications of the spectral features in samples of ML hBN on ML and 2L TMDs. There, the folded bands are not observed to produce minigaps where they cross with the original bands. Thus, any possible moiré effects (which would change the underlying bands) must be disambiguated from final state diffraction effects (affecting only the ARPES). Following this will be a discussion of more recent studies of gated TMD/TMD twisted-heterobilayers, both with and without graphene on top. These results are less ambiguous, as the graphene bands themselves are observed to be replicated according to the moiré of the underlying TMD/TMD bilayer.

4.1 What is a moiré?[168]

Just as the spatially periodic potential of a crystal produces a reciprocal periodicity of the electronic states, a moiré potential imposes an additional periodicity on the bands, producing replicas within the electronic structure of the material. This generates multiple mini-Brillouin zones (mBZ) within the original host Brillouin zone. The strength of the moiré potential is predicted to decrease with twist angle between the layers[169–172]. The position of replica bands, $\boldsymbol{k}^{\mathbf{R}}$, in momentum space is given by:

$$\boldsymbol{k}^{\mathbf{R}} = \boldsymbol{k} - \mathbf{G}_{\mathbf{D}}. \tag{4.1}$$

where $\mathbf{G}_{\mathbf{D}} = \mathbf{G}_{\mathbf{1}} - \mathbf{G}_{\mathbf{2}}$, the difference in reciprocal lattice vectors of the two-interacting consecutive layers and $\boldsymbol{k}$ is the wave vector of the original band.

However, replica bands have another possible origin: electron diffraction. Equation 4.1 also describes the condition for the diffraction of photoelectrons as they pass through the encapsulating atomic layer to the surface. Such diffraction is plausible as the wavelength of the photoelectrons in ARPES experiments is comparable to the atomic spacing in the 2D lattices. Final state diffraction effects are an artefact often seen in high-energy ARPES data[173] and are seen in similar experiments were photoelectrons are scattered by a surface barrier potential[174,175].

The question of whether replica bands seen in ARPES data are a result of a final state diffraction effect or a moiré potential have been considered for studies of graphene on Ir(111) and SiC(0001)[176,177]. The interpretation of results came down to whether there were hybridization minigaps present between the primary and replica bands along the mBZ boundaries, which can only result from an initial state effect, such as a moiré potential.

4.2 Micro-focus low-energy electron diffraction (μ-LEED)

Some of the samples discussed in this chapter were characterized using μ-LEED, and so it is valuable to briefly review the technique. As its name suggests, LEED measures the diffraction of electrons off a surface of interest. Diffraction off of a lattice produces a pattern of spots that reflects the reciprocal lattice. This alone makes it a powerful technique for characterizing a surface of unknown symmetries, e.g. to verify *in-situ* the growth of a desired polytype, or to probe the angular alignment between (and any consequent structural reconstruction of) a grown film and its substrate[178,179]. More quantitative analysis can be performed of the dependence of the diffraction spots' intensities on incident electron energy which results from attenuation of the incident electron beam as it penetrates the structure. This is sensitive to the average absorption height, which itself a function of the registry (and therefore the level of interaction) between the atomic layers at the surface. This so-called I-V analysis (comparing the diffracted current I to the electron gun voltage V defining the electron energy) requires nontrivial simulation and is not presented here.

The μ-LEED measurements that will be presented were performed on the low energy electron microscope (LEEM) at the Nanospectroscopy beamline at Elettra[180]. A micrometer spot size beam of low energy electrons was focused on to the sample through a 20 μm illuminating aperture and the elastically backscattered electrons were directly imaged on a 2D detector. A voltage bias applied to the sample determined the energy of the electron beam. LEEM images of the flake were acquired using a contrast aperture to acquire the μ-LEED patterns at the same positions as the μ-ARPES data. The μ-LEED patterns in Figure 4.2 and Figure 4.4 were acquired with an electron beam energy of 50 eV. The diffraction patterns in Figure 4.6were acquired at multiple energies from 17 - 35 eV, comparable energy to that of the μ-ARPES data, and averaged. Before measurement, the samples were annealed under similar conditions as used for μ-ARPES.

4.3 Twisted hBN / TMD heterostructures

4.3.1 *First encounter in hBN on $W_{0.75}Mo_{0.25}S_2$*

As mentioned Chapter 3, Device 1 had a monolayer hBN cap atop the graphene. The motivation for its inclusion was to sharpen the bands at the cost of overall counts. Time permitting, this approach was also applied to some monolayer TMD devices, including Device 6 (Fig. 4.1**A**). As part of an experimental run probing $W_xMo_{1-x}S_2$ alloys, this device comprised gated ML $W_{0.75}Mo_{0.25}S_2$ wholly capped with ML hBN. Compared to similar devices sans cap, the ARPES counts over the TMD were reduced by about a factor of four, which we attributed to the hBN. Nevertheless, the bands were sharp at $V_G = 0$ with the spin-orbit splitting at **K** clearly resolved in an *E–k* slice through $\mathbf{K}_{TMD}$ (Fig. 4.1**B**). Note that Figure 4.1**B** is plotted in terms of the photoelectron kinetic energy, E_{kin}. The hBN cap and the TMD were coincidentally aligned within a degree in this device, and Figure 4.1**B** just captures the hBN VBM at $\mathbf{K}_{hBN}$. A large minigap can be seen where a TMD band crosses the hBN band (Fig. 4.1**B**, horizontal arrow). At $V_G = 3.75$ V, the TMD CBM at **K** can be seen (Fig. 4.1**C**), though the valence bands have broadened, as has been seen previously when the conduction band is populated (e.g., Fig. 3.6).

Interestingly, the ungated spectra from Device 6 differs from what we have previously seen from monolayer TMDs, with additional valence features (Fig. 4.1**B**, vertical arrows) including one at high E_{kin} in between **Γ** and $\mathbf{K}_{TMD}$. It disperses similarly to the TMD valence band at **Γ** and is centered at a $\boldsymbol{k}^{rep}$ equal to the difference in the momenta of the TMD and hBN zone corners,

$$\boldsymbol{k}^{rep} = \mathbf{K}_{hBN} - \mathbf{K}_{TMD}. \tag{4.2}$$

This is Eq. 4.1 with the original feature at **Γ** (where $\boldsymbol{k} = 0$). These replicated bands do not clearly hybridize/anti-cross where they intersect with original bands from either then TMD or the hBN (Figure 4.1**B**, circled), however, and they are not resolvable when the gate is applied.

Furthermore, careful analysis is made challenging by the alloyed composition, which complicates theoretical prediction of the original bands with which to compare. Nevertheless, this observation was, to our knowledge, the first of a replicated band in an incommensurate 2D structure, and so sufficiently intriguing to merit further studies of twisted ML hBN on TMDs.

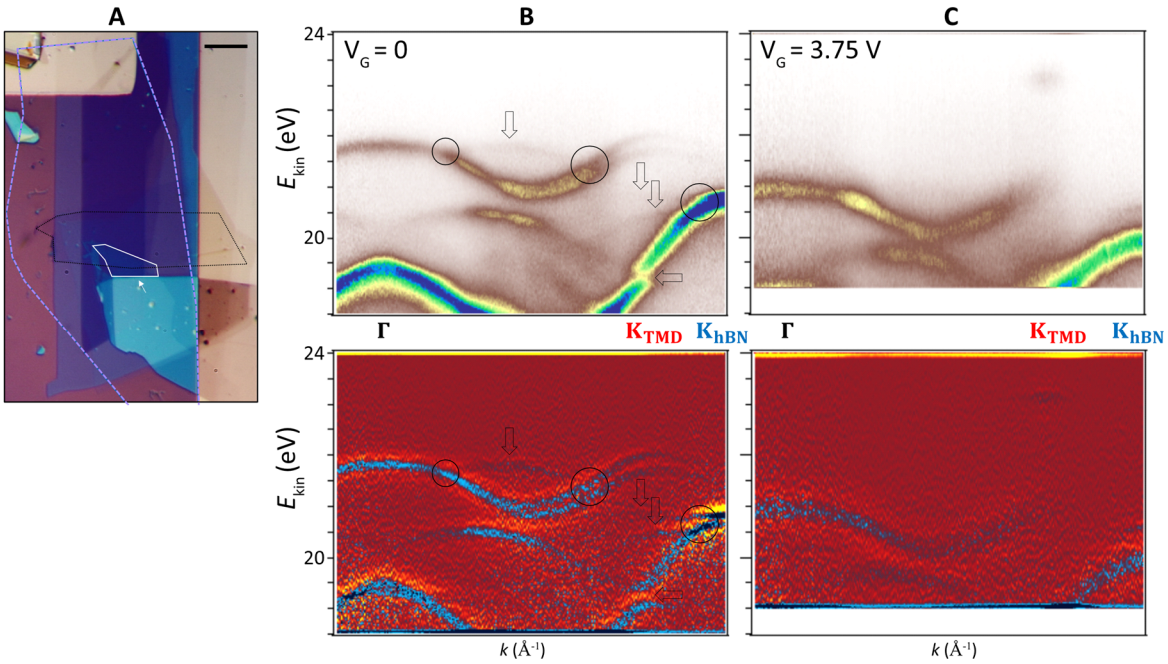

Figure 4.1. Replicated bands in a gated ML hBN/ML $W_{0.75}Mo_{0.25}S_2$ heterostructure. **A**, an optical image of Device 6. The graphene is outlined in black, the ML $W_{0.75}Mo_{0.25}S_2$ in white, and the monolayer hBN in blue. **B**, energy-momentum slice spectra (above) and twice-differentiated (below) connecting **Γ**, and the **K**-points of the TMD, $\mathbf{K}_{\mathrm{TMD}}$, and of the capping hBN, $\mathbf{K}_{\mathrm{hBN}}$ from the hBN/TMD/back gate region with $V_{\mathrm{G}} = 0$. The horizontal arrow points at the avoided crossing between the TMD and hBN bands. Vertical arrows point at replicated bands. Circled are where replicated and original bands cross. **C**, energy-momentum slice spectra (above) and twice-differentiated (below) with $V_{\mathrm{G}} = 3.75$ V.

4.3.2 *Small-angle twisting of ML hBN on WSe_2*

To go beyond this serendipitous observation, we turn to study a ML TMD we know better, WSe_2, starting with Device 7. Figure 4.2**A** shows a schematic of the device, and Figure 4.2**B** shows an optical image with the different flakes outlined. The mismatch $\delta a/a$ between the in-plane lattice

constants of WSe_2 and hBN is about 32% (a_{WSe_2} = 3.32 Å, a_{hBN} = 2.52 Å). The stacking of misaligned ML hBN on top of ML WSe_2 therefore creates a highly incommensurate heterostructure. μ-LEED measurements performed on the device (Figure 4.2**C**) show a twist angle of 2 ± 1° between the layers. The electron diffraction pattern shows the first order diffraction spots from the hBN and WSe_2 plus additional diffraction spots seen at positions corresponding to the vector $\mathbf{G}_D$. A schematic of the relative orientation and size of the hBN (blue) and WSe_2 (red) hexagonal Brillouin zones can be seen in Figure 4.2**D**.

Replica bands are seen in the valence band structure of the sample, which also appear at positions $\mathbf{G}_D$ from the primary bands. Figure 4.3**A** shows μ-ARPES constant energy maps at a variety of binding energies. The maps show numerous repeated features much unlike what would be expected from previous measurements without an hBN cap (*cf.* Fig. 2.3). Take for example, the map through $E - E_F = 1.21$ eV through the WSe_2 VBE at **Γ**. In the region of momentum space probed, three replica **Γ** bands of WSe_2, $\mathbf{\Gamma}^R$, are seen within the first WSe_2 BZ (bounded by the red lines), highlighted by the hollow black circles. An energy-momentum slice along the direction of the black arrow labelled $\mathbf{G}_D$ in that map is shown in Figure 4.3**B**. The spectrum below is a double-differentiated spectrum of the above. No hybridization gap is observed at the mini BZ boundary

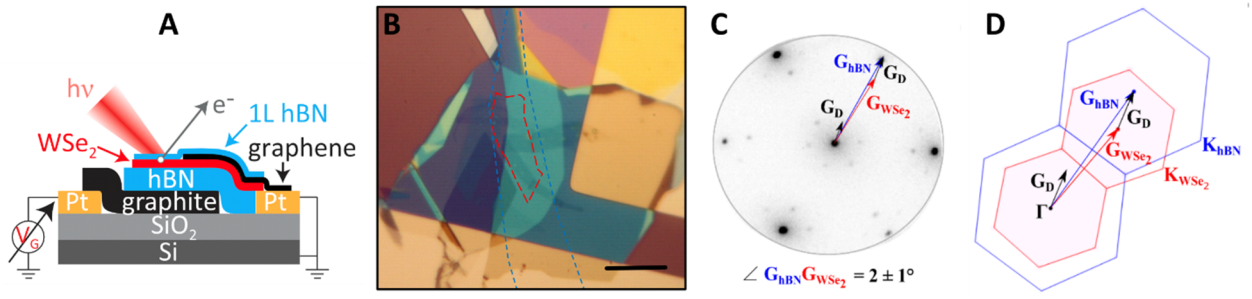

Figure 4.2. A twisted ML hBN on WSe_2 device. **A**, schematic and **B**, optical image of Device 7. The ML WSe_2 is outlined in red, and the ML hBN in blue. Scale bar 15 μm. **C**, schematic of hBN (blue) and WSe_2 (red) Brillouin zones. Difference in the reciprocal vectors, $\mathbf{G}_{hBN}$ and $\mathbf{G}_{WSe2}$, given by $\mathbf{G}_D$ (black arrows). High symmetry points are labelled. **D**, μ-LEED image with voltage 50 eV.

where the **Γ** and **Γ^{R}** bands intersect (white arrow). The absence of the hybridization gap could be attributed to its magnitude being smaller than the energy resolution of the beamline (50 meV) because of a very weak moiré-periodic potential. However, the intensity of the replica bands observed are relatively strong, suggesting that at least a proportion of their intensity is likely due to final state diffraction effects.

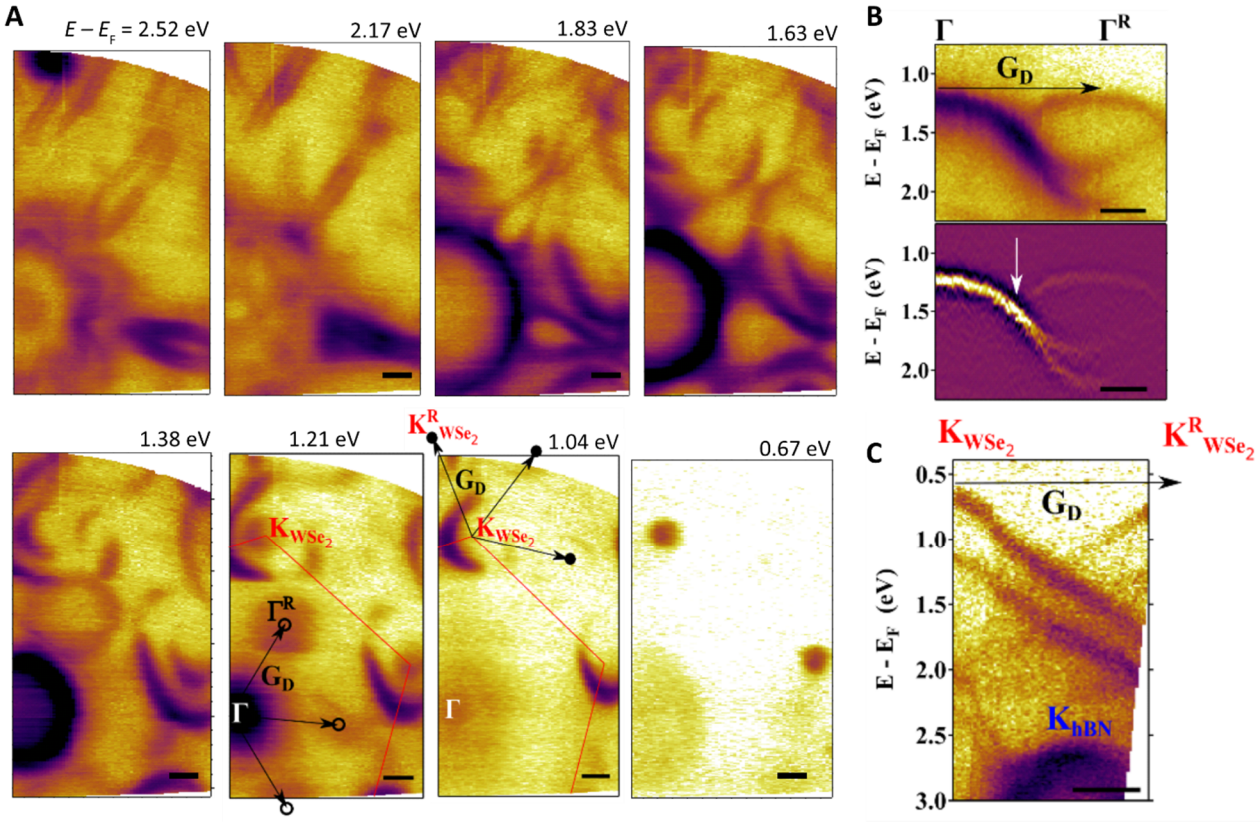

Figure 4.3. Bands in low twist angle hBN/TMD. **A**, constant energy μ-ARPES maps at a variety of binding energies. Two maps at $E - E_F = 1.21$ and 1.04 eV, are labelled with the various high symmetry points. Positions of replica **Γ** bands, **Γ**^{R}, are indicated by hollow black circles. Positions of replica **K**$_{WSe2}$ bands, **K**$^{R}_{WSe2}$, are indicated by solid black circles. **B** and **C**, energy-momentum slices between Γ(K$_{WSe2}$) and **Γ**^{R}(**K**$^{R}_{WSe2}$) along arrows labelled **G**$_D$ in maps at $E - E_F = 1.2$ and 1.0 eV respectively. Underneath in **B**, second derivative spectra of above with white arrow showing where the **Γ** and **Γ**^{R} bands overlap. Red lines mark the Brillouin zone boundary of WSe_2. All scale bars, 0.2 Å^{-1}.

Figure 4.3**C** shows a μ-ARPES constant energy map at a binding energy just below the VBM of the WSe_2 **K** point ($\mathbf{K}_{WSe2}$). Similarly, replica bands, $\mathbf{K}^{R}_{WSe2}$, can be seen at positions corresponding to the vector $\mathbf{G}_D$, highlighted by the solid black circles. Again, an energy-momentum slice along the direction of the black arrow with the label $\mathbf{G}_D$ in Fig. 2e is shown in Fig. 2f and no hybridization gap is observed between the primary and replica bands. Similar results, as described above, have also been observed for a heterostructure of ML graphene on ML WSe_2 with small twist angle[172].

4.3.3 *Large-angle twisting of ML hBN on WSe_2*

Similar results were observed in Device 8 (Fig. 4.4**A**) which has a large twist angle between the top ML hBN and WSe_2. Figure 4.4**B** shows a μ-LEED diffraction pattern from this device revealing a twist angle of 28 ± 2°. As with Device 7 (*cf.* Fig. 4.2**C**), additional diffraction spots are also observed at positions corresponding to $\mathbf{G}_D$. Figure 4.4**C** shows the relative orientation of the BZs.

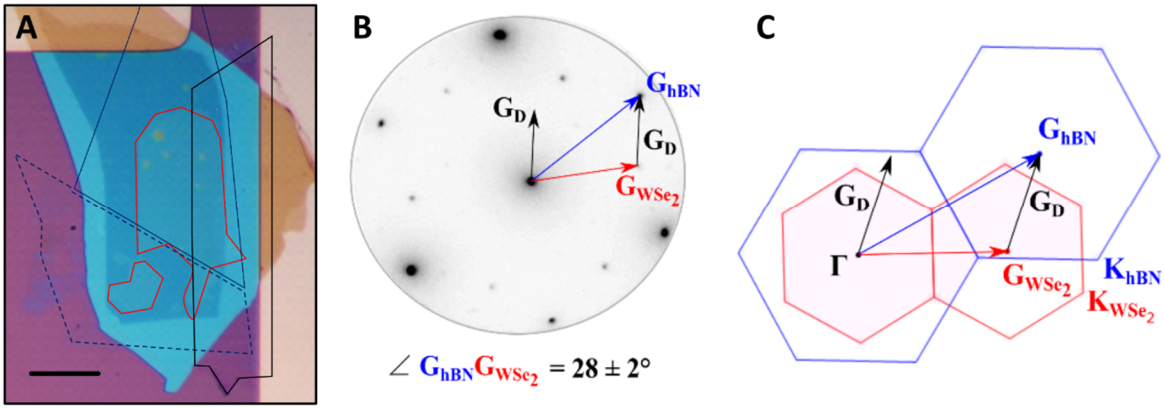

Figure 4.4. A ML hBN on ML WSe_2 device with large twist. **A**, optical image of Device 8. The ML WSe_2 is outlined in red, ML hBN in solid blue, 2L hBN in dashed blue, and graphene in black. Scale bar 14 μm. **B**, μ-LEED image with start voltage 50 eV. and **C**, schematic of hBN (blue) and WSe_2 (red) Brillouin zones. Difference in the reciprocal lattice vectors, $\mathbf{G}_{hBN}$ and $\mathbf{G}_{WSe2}$, given by the vector $\mathbf{G}_D$ (black arrows). High symmetry points are labelled.

Within the momentum space field of view, multiple replica WSe_2 **K** points, $\mathbf{K}^{R}_{WSe2}$, were observed, clearly manifesting as a hexagonal pattern of dots about **Γ** near the VBM energy $E - E_F = 0.60$ eV. The formation of these replica bands close to **Γ** is explained by the schematic in Figure 4.5**B**. Other replicas $\mathbf{K}^{R}_{WSe2}$ can be identified both outside the first BZ and inside, as shown in the slice at $E - E_F = 0.89$ eV. Additionally, one replica **Γ** band, $\mathbf{\Gamma}^{R}$, is observed at the expected position, seen in the μ-ARPES constant energy map at $E - E_F = 1.09$ eV, Figure 4.5**A**. An energy-momentum slice in the **Γ** - $\mathbf{\Gamma}^{R}$ direction is shown in Figure 4.5**C**.

The observation of these replica bands is unexpected as a previous report for ML graphene on ML WSe_2 heterostructure with large twist angle did not observe any replica bands. This was attributed to the fact that the moiré potential was too weak at such large twist angle[172]. The high

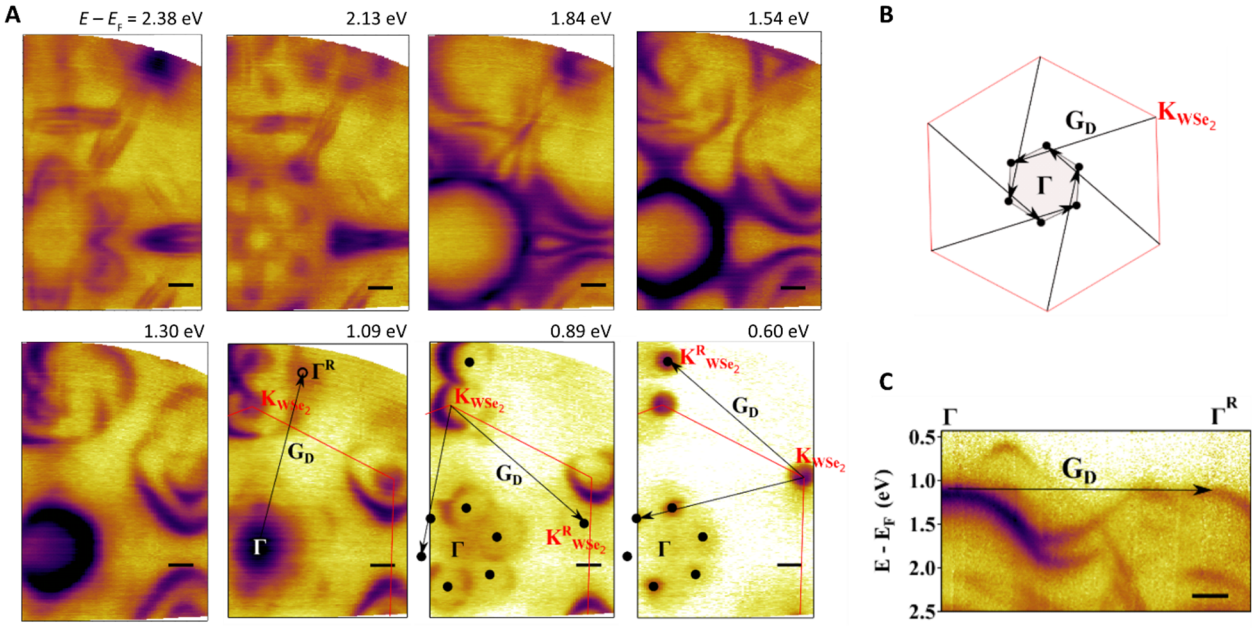

Figure 4.5. Bands in large twist angle hBN/TMD. **A**, constant energy μ-ARPES maps at a variety of binding energies. Two maps at $E - E_F = 1.09$, 0.89 and 0.60 eV, are labelled with the various high symmetry points. Positions of replica **Γ** bands, $\mathbf{\Gamma}^{R}$, indicated by hollow black circles. Positions of replica $\mathbf{K}_{WSe2}$ bands, $\mathbf{K}^{R}_{WSe2}$, indicated by solid black circles. **B**, Schematic of formation of $\mathbf{K}^{R}_{WSe2}$ around **Γ**. **C**, Energy-momentum slice between **Γ** and $\mathbf{\Gamma}^{R}$ labelled in **A**. All scale bars, 0.2 $Å^{-1}$.

intensity of the replica bands seen in our data and again the absence of the hybridization gap suggests these replica bands are due to final state diffraction effects. However, further experimentation is still required to resolve whether a moiré potential is still present which could be contributing to the intensity of the replica bands observed.

4.3.4 *Twisted hBN and $MoSe_2$*

For comparison, a heterostructure of a different TMD, $MoSe_2$, was also studied. $MoSe_2$ has a similar lattice constant to WSe_2 (a_{MoSe2} = 3.28 Å). For Device 9, a partially hBN encapsulated $MoSe_2$ sample, μ-LEED and μ-ARPES measurements were performed on three different regions: (1) ML $MoSe_2$ on hBN, ML (2) hBN on ML $MoSe_2$ and (3) ML hBN on bilayer (BL) $MoSe_2$, illustrated by Figure 4.6**A**. An optical image of the sample is shown in Figure 4.6**B**, , where the yellow box indicates where the SPEM map in Figure 4.6**C** was taken. For each region, additional diffraction spots were observed in the μ-LEED patterns, Figure 4.6**C - E**. These measurements were used to find the twist angle between the top two layers in each region. Figure 4.6**F - H** show constant energy slices from the corresponding regions taken at different energies.

We start with region (1), where there was no hBN cap. Interestingly, no first order diffraction spots from hBN were observed here (Fig. 4.6**C**) despite the presence of the hBN back gate. Nonetheless, spots not associated directly with the $MoSe_2$ were observed (which we assign to $\mathbf{G}_D$) From this, we can infer the twist angle between the $MoSe_2$ and the underlying hBN of $7\pm1°$. In addition, one replica band of the $MoSe_2$ **K** point was observed within the region of momentum space probed (Fig. 4.6**F**). Scattering from an underlying hBN substrate has also been shown to form replica bands of graphene in ARPES[181], and a diffraction-replicated feature can be identified by analyzing the symmetry of their dark corridors. Unfortunately, the only feature observed here is centered beyond the accessible momentum space, and its symmetries cannot be

determined. To clarify the underlying physics will require further study, though this is the only known observation in this system despite many studies on our part of TMD on hBN.

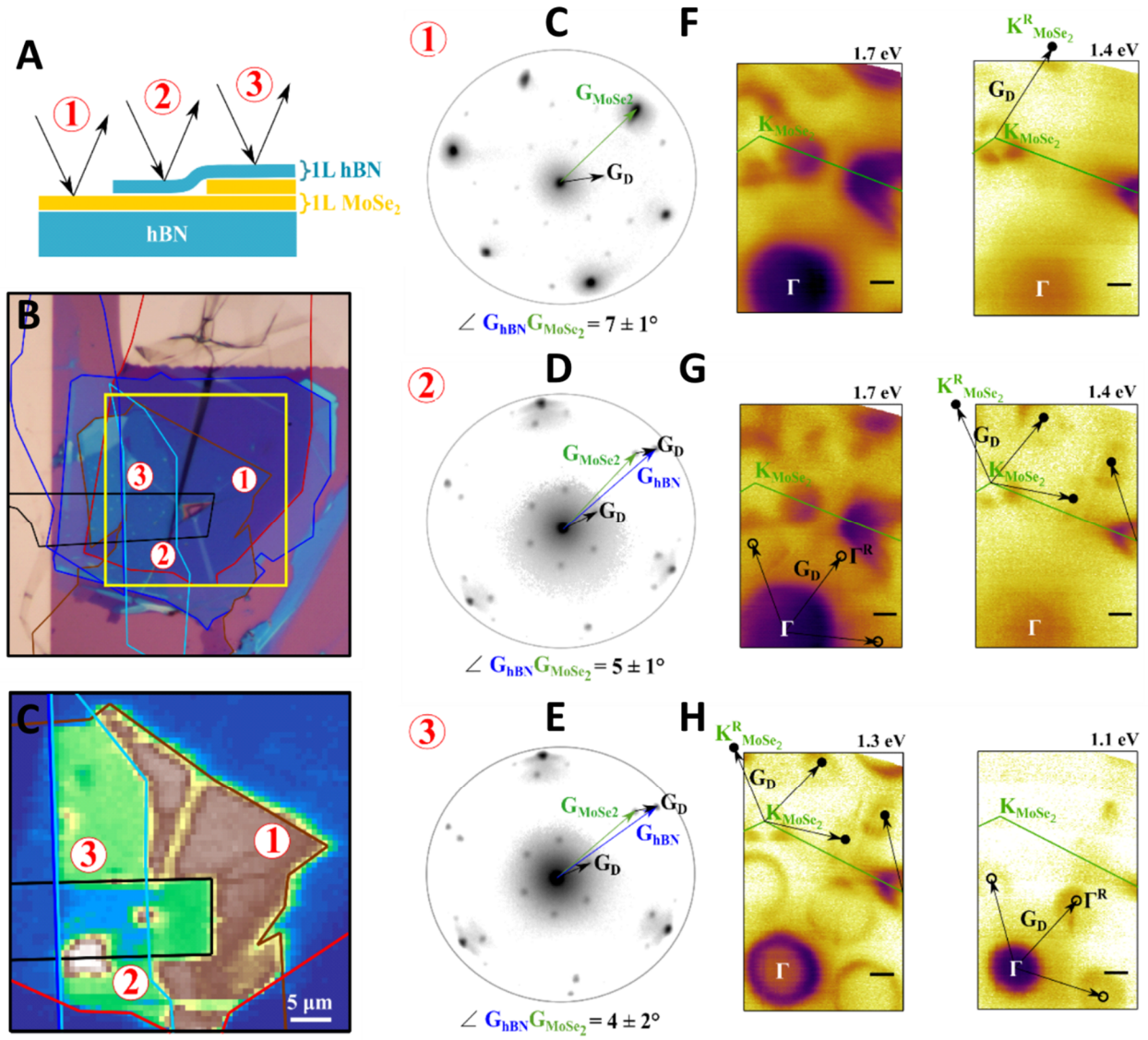

Figure 4.6. Twisted hBN on $MoSe_2$. **A**, sample schematic, and **B**, optical of Device 9. Different layers are outline, ML hBN (light blue) and thick hBN (blue) on graphene (black) on $MoSe_2$ (brown) on hBN (blue) on graphite back gate (red). Yellow square shows area imaged in **C**. **C**, SPEM map identifying location of regions 1, 2, and 3. **(C-E)** Averaged µ-LEED image from start voltage of 17-35 eV. **(E-G)** Constant energy µ-ARPES maps at the binding energy defined in top left of the individual maps. Position of replica **Γ** bands, $\mathbf{\Gamma}^R$, indicated by hollow black circle. Position of replica $\mathbf{K}_{MoSe2}$ bands, $\mathbf{K}^R_{MoSe2}$, indicated by solid black circles. Otherwise noted, all scale bars, 0.2 $Å^{-1}$.

Encapsulating ML $MoSe_2$ in hBN (region 2) shifts the $MoSe_2$ bands lower in binding energy by 0.04 eV, which can be attributed to a shift of the surface work function. The μ-LEED pattern (Fig. 4.6**D**) clearly shows a set of spots from hBN and from the $MoSe_2$ monolayer. The $MoSe_2$ spots are identical to those from the uncapped region. However, the small wavevector features are different here, though they can be described via the $\mathbf{G}_D$ expected from the observed primary spots. This suggests that these hBN spots are coming from the cap, rather than the supporting hBN. The constant energy maps (Figure 4.6**D**) from this region show replica features like those already discussed in this section. Notably, the same effect is seen, but an order of magnitude larger, when encapsulating WS_2 between graphene and hBN[172].

Finally, for bilayer $MoSe_2$ (region 3), the **Γ** point is the VBM at a binding energy of 1.1 eV, whereas in the ML the **K** point is the VBM. Figure 4.6**E** shows a μ-LEED diffraction pattern similar to that from the ML $MoSe_2$ region. However, higher intensity replica bands are seen in the μ-ARPES measurements of the bilayer (Figure 4.6**H**).

4.3.5 *Summary*

This section has shown a variety of studies hBN twisted with one- and two-layer TMDs. In all samples even without a capping hBN layer, μ-LEED revealed all (first order) diffraction spots expected from Equation 4.1. The μ-ARPES was less consistent, not showing every feature that would be expected by a complete application of Eq. 4.1. Furthermore, replication-related anti-crossings were not observed, as would be expected if the replicas actually resulted from a moiré superpotential. Finally, the moiré periodicity between hBN and TMDs is ≅1 nm, which would severely limit the strength of the resultant potential[103,182]. These issues suggest that the underlying mechanism is final state diffraction. Potential future measurements to fully address this problem are time-resolved μ-ARPES, and I-V analysis to see if a moiré pattern is in fact present.

4.4 Case study: Monolayer WS_2 on monolayer WSe_2 with finite twist

Chapter 2 discussed how twisting monolayers of WSe_2 and $MoSe_2$ at a small but finite angle can still produce strong hybridization between bands of out-of-plane character. We argued this results from these layers with similar lattice constants ($\delta a/a \approx 0.3\%$) forming commensurate domains wherein the interlayer coupling is maximized. This section will consider in detail a particular heterostructure of WS_2 and WSe_2, which have a lattice mismatch of ~ 4%[183]. Even with nearly zero twist, this system should remain incommensurate throughout. Despite this, the WS_2/WSe_2 heterobilayer hosts the strongest moiré potential of all TMD combinations[182]. The device discussed here has a working back gate with which to probe the conduction bands to reveal a different manifestation of band replication than was seen with monolayer hBN capping. This will allow direct determination of the band alignments of the TMD MLs. Additionally, the graphene partially above the heterobilayer will provide a useful probe of the moiré superpotential formed by the TMDs, with its Dirac cone is replicated according to the TMD/TMD moiré vector $\mathbf{G}_D$.

4.4.1 *Device characterization*

Figure 4.7**A** shows an optical image of Device 10. Note that the graphene has been shaped into a comb using electrochemical AFM cutting[121]e before being transferred along with the rest of the heterostructure. This maximizes the heterobilayer area that is near but not under the grounding graphene. As discussed in Chapter 3, such areas are where the conduction band ARPES signal is generally strongest and stablest. To determine the twist angle between the TMDs in this device, we employed contact-resonant lateral PRM to image the moiré pattern both where the heterobilayer is uncapped, and capped with graphene (Fig. 4.7**B** and **C**, respectively). 2D FFTs of the maps show peaks at the moiré periods, which are ~ 2.5 nm on average in both regions. That

the FFT peaks are at different radii implies the moiré is anisotropic, i.e., the system is strained[184]. The twist angle θ is related[123] to the period λ, lattice constant a, and lattice mismatch δ by

$$\lambda = \frac{(1+\delta)a}{\sqrt{2(1+\delta)(1-\cos(\theta))+\delta^2}} \text{ which yields } \theta \approx 7°. \quad (4.3)$$

A large area SPEM map (Fig. 4.8**A**) with the gate grounded highlights where the TMD flakes overlap the gate but are not obscured by the graphene ground. Scanning photocurrent microscopy (SPIM) performed over the same area (Fig. 4.8**B**) highlights where the current measured to the graphene ground lead is greatest. With the gate grounded and the TMD(s) insulating, this is where the grounded graphene overlaps with the gate (and therefore generates an additional current from it, see Figure 3.6). Higher resolution SPEM and SPIM maps taken around the area of interest (Figs. 4.8**C** and **D**) reveal an area where the TMD photoemission is uniformly strong, and multiple (but not all) of the graphene 'fingers' remain contiguous and grounded.

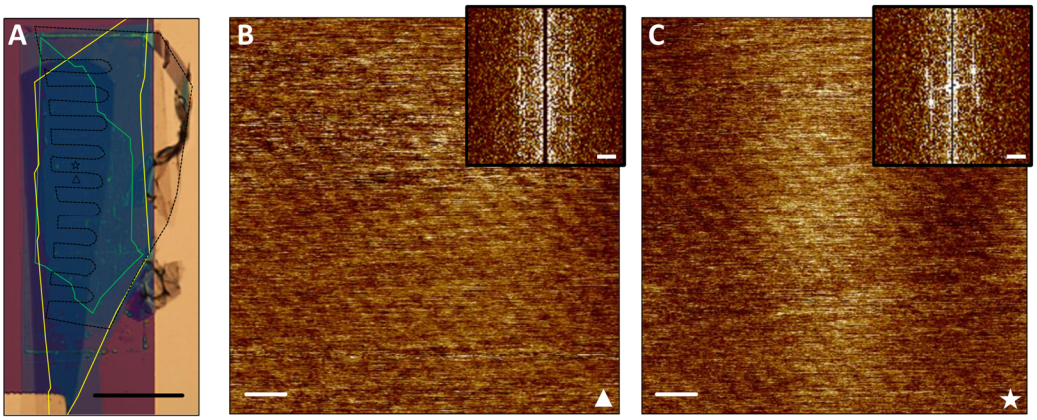

Figure 4.7. Microscopy of a gated WS_2/WSe_2 device with small twist. **A**, optical image of Device 10, outlining the graphene (black dashed), ML WS_2 (yellow), and ML WSe_2 (green). Scale bar 15 µm. **B** and **C**, contact-resonant lateral PRM taken in the uncapped heterobilayer (marked with a triangle in **A**) and graphene capped heterobilayer regions (marked as a star in **A**), respectively. Scale bars are 5 µm. Insets in **B** and **C**, FFTs of the corresponding spatial maps, scale bars, 1 nm.

Figure 4.8**E** plots the photocurrent as a function of back gate voltage over the heterobilayer with and without graphene. A clear rise in the photocurrent from the uncapped bilayer, indicating when the TMD(s) become conducting, can be seen at $V_G \approx 1.5$ V. SPEM taken at 2.5 V (Fig. 4.8**F**) highlights a slightly smaller area than at 0V, suggesting that the heterobilayer (or the smaller monolayer) is more conductive than the rest. A SPIM map taken at the same voltage (Fig. 4.8**G**) shows that the gated TMDs and the graphene are indeed conducting.

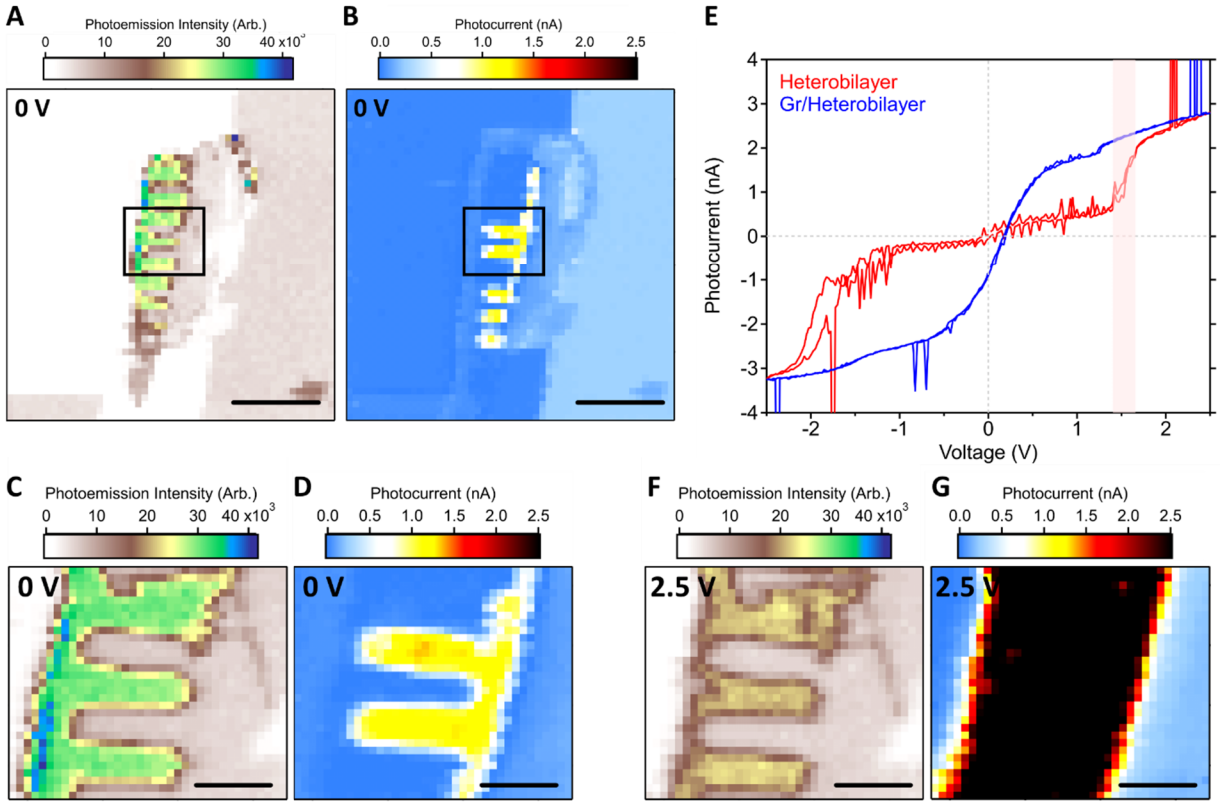

Figure 4.8. SPEM and SPIM of a gated WS_2/WSe_2 device with small twist. **A**, large area SPEM and **B**, corresponding SPIM at 0 V. SPIM highlights the most conducting regions, i.e. where grounded graphene overlaps the gate. Scale bars 20 µm. **C**, SPEM and **D**, corresponding SPIM at 0 V of region of interest (solid black boxes in **A**, **B**) with intact graphene pieces (highlighted in SPIM). **E**, photocurrent vs gate voltage from graphene capped (blue) and uncapped (red) regions. **F,** SPEM and **G**, corresponding SPIM (right) at 2.5 V in the region of interest. Scale bars in **C, D, F,** and **G**, 5 µm.

4.4.2 *Ungated spectra*

Figure 4.9**A** and **B** show constant energy slices through binding energies near the WS_2 and WSe_2 VBM containing the **Γ** and the **K** points of the TMDs with the gate grounded. The two zone corners can clearly be identified, and from this a twist angle of ~7° can be immediately determined, consistent to the PRM result. No replicated features can be observed over the probed region of

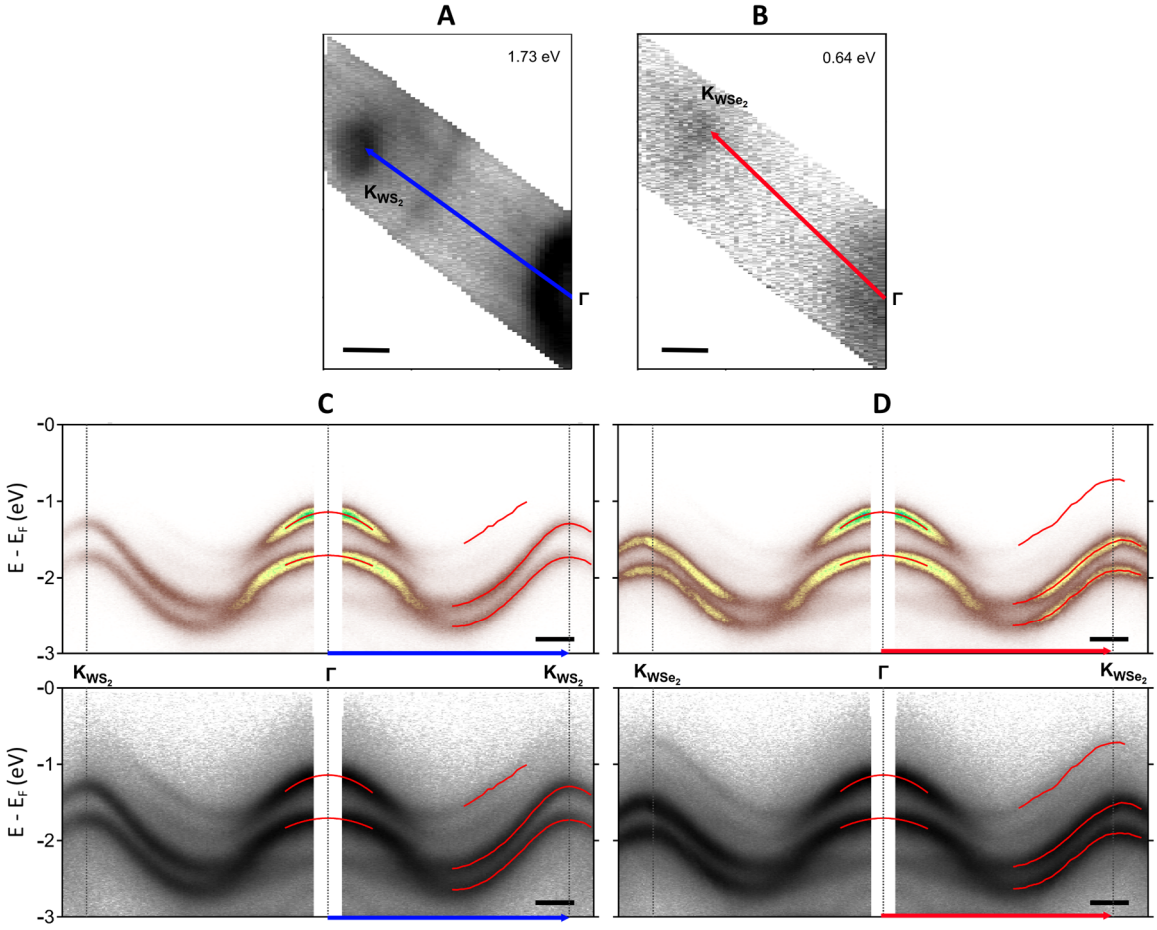

Figure 4.9. Ungated bands WS_2/WSe_2 device with small twist. **A** and **B**, constant energy maps through WS_2 **K** VBM and the WSe_2 **K** VBM respectively, both averaged over 0.6 eV, at inscribed binding energies. Suggests a twist angle of ~5°. **D**, E - k slices of WS_2/WSe_2 heterobilayer at 0 V, along the high symmetry directions **Γ**-$\mathbf{K}_{WS2}$ and **Γ**-$\mathbf{K}_{WSe2}$, as illustrated in **A** (blue arrow), and **B** (red arrow), respectively. Red lines show peak fits through EDCs near **Γ** and the WSe_2 and WS_2 **K** points (where possible). Plots are mirrored across **Γ** for clarity. Color plots are linearly scaled, grayscale plots are log-scaled. All scale bars, 0.2 $Å^{-1}$**.**

momentum space. Figure 4.9**C** and **D** plot energy-momentum slices along the high symmetry directions **Γ**-$\mathbf{K}_{WS2}$ and **Γ**-$\mathbf{K}_{WSe2}$. Again, no extraneous spectral features can be identified. Note that the intensities of the bands assigned to WSe_2 are substantially lower than those from WS_2, as can be expected from the fact that the WSe_2 is underneath.

Nonetheless, the WSe_2 dispersion near $\mathbf{K}_{WSe2}$ can be fitted to (red line), yielding an effective mass $m_K^*/m_e = 0.47 \pm 0.02$. This and other band parameters are summarized in Table 4.1. The effective masses at the **K** points are in agreement with our previous measurements (Table 3.1) when comparing the uppermost band here to isolated ML WSe_2, and the third band from the top to ML WS_2. This is consistent with the orbital composition analysis for $MoSe_2$ and WSe_2 which holds here, and so permits assignment of the bands at **K** in this heterobilayer to the respective layers. As the two bands at **Γ** each flow continuously into a particular material's spin-split **K** bands, it is tempting to assign them similarly, i.e., the upper band to WSe_2. However, the effective mass of the upper band here differs substantially from our previous measurement for ML WSe_2 (Fig. 2.6). This indicates strong hybridization of these bands without either global commensuration (given the large twist angle), or commensurate domains (as there are only 2 bands at **Γ**).

	Peak Energy (eV)	m^*/m_e
Upper **Γ**	1.144 ± 0.001	0.88 ± 0.01
Lower **Γ**	1.707 ± 0.001	1.45 ± 0.01
Upper $\mathbf{K}_{WSe_2}$	0.716 ± 0.002	0.47 ± 0.02
Upper $\mathbf{K}_{WS_2}$	1.293 ± 0.001	0.38 ± 0.01
Lower $\mathbf{K}_{WS_2}$	1.732 ± 0.001	0.56 ± 0.01

Table 4.1. Measured band parameters in a WS_2/WSe_2 heterobilayer with $V_G = 0$. Parameters extracted from bands observable in Figure 4.9, from peak positions of Lorentzian fits to EDCs (Figure 4.9, red lines).

Figure 4.10 shows spectra from spots where graphene overlaps the heterobilayer. Constant energy surfaces (Figs. 4.10**A** and **B**) show strong emission, and an energy-momentum slice through the Dirac point (Fig. 4.10**C**) shows reasonably sharp linear bands. A surprise comes from comparing to the spectra in Figure 3.1, which were taken along a similar line in the BZ. Those

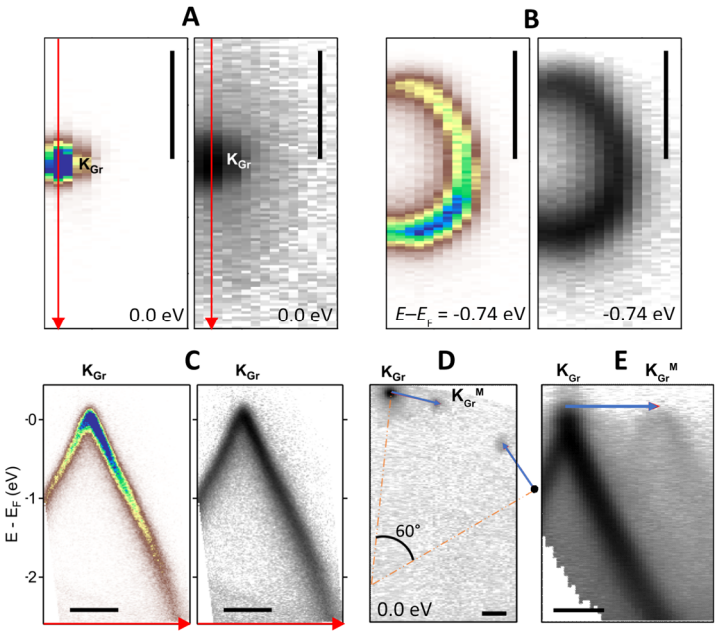

Figure 4.10. Ungated strained graphene. **A** and **B**, constant energy maps through $E - E_F = 0$ and -0.74 eV. **C**, *E-k* through Dirac cone (red arrow in **A**). **D**, large area constant energy map through $E - E_F = 0$, showing natural Dirac point ($\mathbf{K}_{Gr}$) and replica Dirac at ($\mathbf{K}_{Gr}^{R}$). **E**, *E-k* through $\mathbf{K}_{Gr}$ and $\mathbf{K}_{Gr}^{R}$ (blue arrow in **D**). In each pair, data is linearly scaled on the left, log-scaled on the right. All scale bars, 0.2 Å^{-1}. (**A-C**) and (**D**&**E**) acquired from different spots on the device.

bands were highly asymmetric about the **K** point as the result of cutting across the graphene dark corridor. In contrast, the bands in Figure 4.10**A** and **B** are symmetric in intensity. The constant energy surfaces similarly reveal no strong angular dependence on the photoemission intensity. Since the dark corridor is an effect of the sublattice sites in graphene being equivalent, this suggests that the sublattice symmetry has been lifted here. This may be the result of coupling to the underlying TMD heterobilayer, the moiré pattern of which was shown to be strained by PRM.

In Figure 4.10**D**, a larger area constant energy slice through E_F, the Dirac point at $\mathbf{K}_{Gr}$ can clearly be identified along with two other, fainter spots. The closer of them to $\mathbf{K}_{Gr}$ has been labeled $\mathbf{K}_{Gr}^{R}$. An *E* - *k* cut connecting it and $\mathbf{K}_{Gr}$ shows that this feature replicates the graphene bands and is ~0.4 Å away (Fig. 4.10**E**). A cut through the other spot similar shows a faint Dirac cone. As it was outside of the measurement range, the position of $\mathbf{K'}_{Gr}$ close to the second spot must be extrapolated (rightmost dashed orange line, Fig. 4.10**D**). Its distance from the second spot is also ~0.4 Å^{-1}, and the vector connecting them is consistent with being 120° rotated from the vector connecting $\mathbf{K}_{Gr}$ and $\mathbf{K}_{Gr}^{R}$.

4.4.3 *Gating the twisted heterobilayer*

As was seen in Chapter 3, applying a sufficiently large V_G can generate a measurable CBM signal. Based on previous measurements of the direct band gap in each ML (Table 3.1), and the band offset at **Γ** of 0.564 eV from Figure 4.9, the band alignment can be expected to be type II (as with $MoSe_2/WSe_2$), and the global CBM at $\mathbf{K}_{WS_2}$. Indeed, with V_G at 2.5 V (above the threshold from Figure 4.8) a line cut from **Γ** to $\mathbf{K}_{WS_2}$ shows a strong feature at the Fermi energy directly above the WS_2 VBM (Figure 4.13**A**). Pushing the gate to 3 V (Figure 4.13**B**) produces a fainter feature at **Q** like what was seen in ML WSe_2 (Figure 3.7). Eq. 3.2 gives $n_G(3V) = 6.4 \pm 0.4 \times 10^{12}\text{cm}^{-2}$ at this voltage, which is much lower than the voltage previously required to populate the **Q**-point with ML WSe_2.

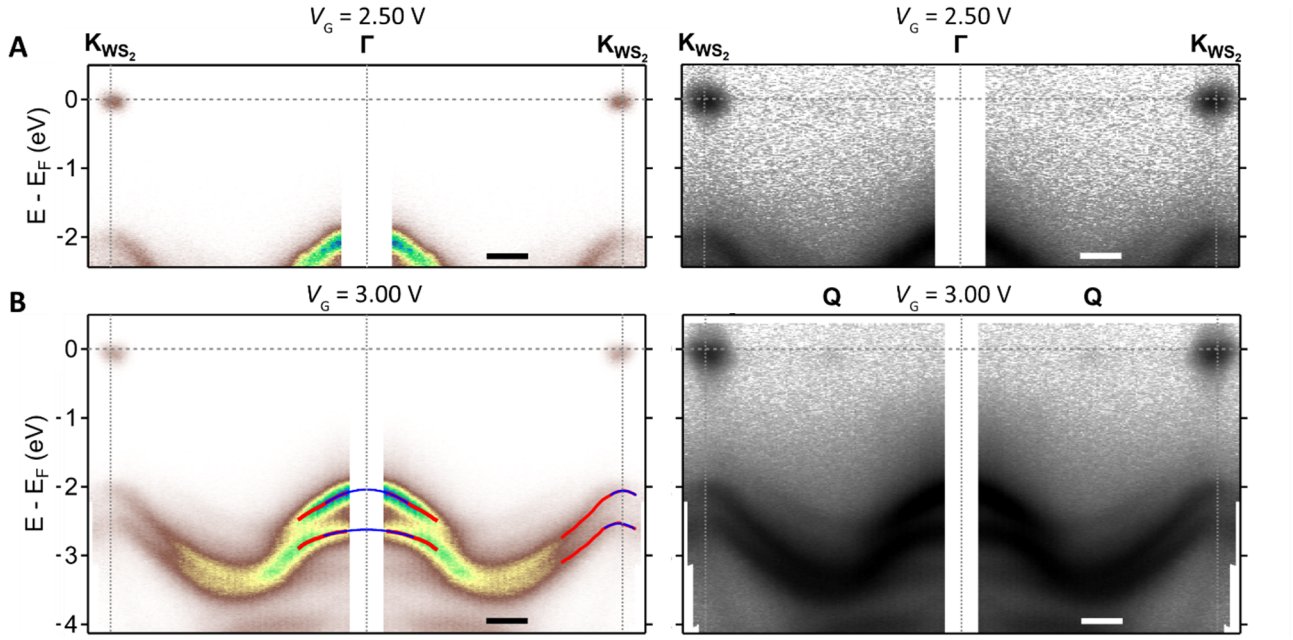

Figure 4.11. Gated bands in a WS_2/WSe_2 device with small twist. Energy-momentum slices of WS_2/WSe_2 heterobilayer at $V_G = 2.50$ V (**A**), and 3.00 V (**B**) along **Γ**-$\mathbf{K}_{WS2}$. Slices are plotted with a linear color scale (left), and on a log scale (right) to highlight low intensity features. Red lines show peak fits to EDCs in the vicinities of **Γ** and $\mathbf{K}_{WS2}$, blue lines are parabolic fits to red lines. Plots are mirrored across **Γ** for clarity. Scale bars, 0.2 Å^{-1}.

Unlike with previous measurements, however, the CBM feature at $\mathbf{K}_{WS_2}$ with $V_G = 3$ V is not flat and instead seems to disperse on close inspection (Fig. 4.12**A**). Taking EDCs through the feature (Fig. 4.12**B**) reveals the momentum-dependence of the energy of peak photoemission intensity, which can be estimated by naïvely fitting each EDC to a Lorentzian. The centers of these Lorentzians can be fitted to coarsely estimate the WS_2 CBM effective mass, $m^*_{WS_2\ CBM}/m_e \sim 0.2$. In **k**-space, if the CBM is in fact resolvably far away from E_F, then the Fermi surface should be an annulus. Figure 4.12**D** shows that this is indeed the case, with the peak intensity (yellow) forming a ring about $\mathbf{K}_{WS_2}$. The fact that the conduction band dispersion could be resolved here but not in any other device may be thanks to the cut graphene reducing the effective resistance to the ground.

A more robust fit would be to the product of a Lorentzian with a Fermi function centered on $E_F = 0$. However, the counts here are relatively low which makes it difficult to deconvolve the two factors when they are so close energetically. This primarily affects the extracted dispersion

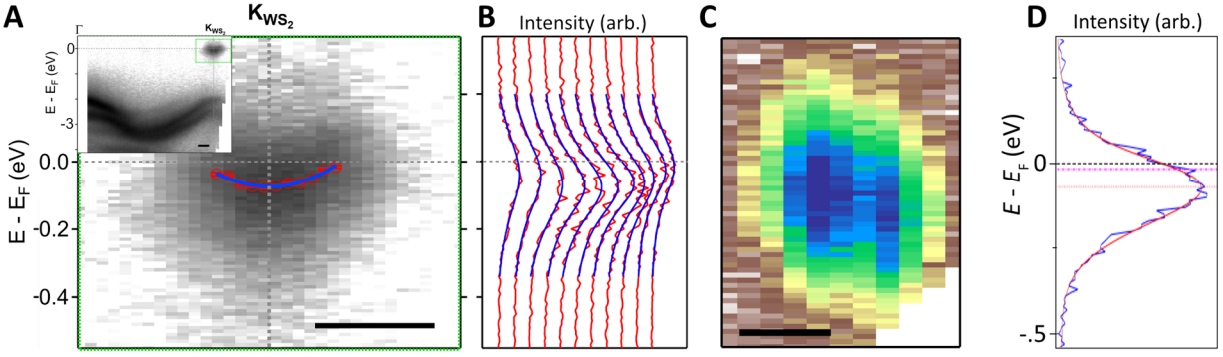

Figure 4.12. Curvature of WS_2 CBM. **A**, *E-k* slice zoomed in around the WS_2 CBM at $\mathbf{K}_{WS_2}$, from full *E-k* slice (inset, green box) at $V_G = 3$ V. Intensities are log-scaled. **B**, EDCs through CB (red lines), each averaged over 0.01 Å^{-1} and fit to a Lorentzian (blue curves). Fitted peak center energies from **B** (red dots) are fitted to a parabolic dispersion (blue curve) and overlaid in **A**. **C**, constant energy map averaged over $0 > E - E_F > 0.15$ eV, **D**, EDC through CBM (solid blue line) and fit to a Fermi function centered at $E - E_F = 0$ times a Lorentzian (solid red line). Dashed lines mark E_F (black), the fitted Lorentzian center (blue), and overall maximum intensity (yellow). Scale bars in **A** and **C**, 0.1 Å^{-1}.

away from $\mathbf{K}_{WS_2}$ and therefore the fitted m^*. Nevertheless, we can fit this proper model to the EDC through the CBM (Fig. 4.12**D**) to extract a band position of 17 $\pm$ 1 meV below E_F. This is equal to the energy offset between CBM and the $\mathbf{Q}_{WS_2}$ CBE if we assume that the CBE is only just being populated. Comparison of this to the center of the single Lorentzian fit at 74 meV below E_F shows that a more careful analysis of the conduction band dispersion will be required.

So far, we have only examined the low energy spectra along the WS_2 high symmetry direction, observing two features: a manifest CBM at $\mathbf{K}_{WS_2}$, as expected, and seemingly a CBE at $\mathbf{Q}_{WS_2}$. Taking instead an energy-momentum cut from **Γ** to $\mathbf{K}_{WSe_2}$ (Fig. 4.13**A**) shows, surprisingly

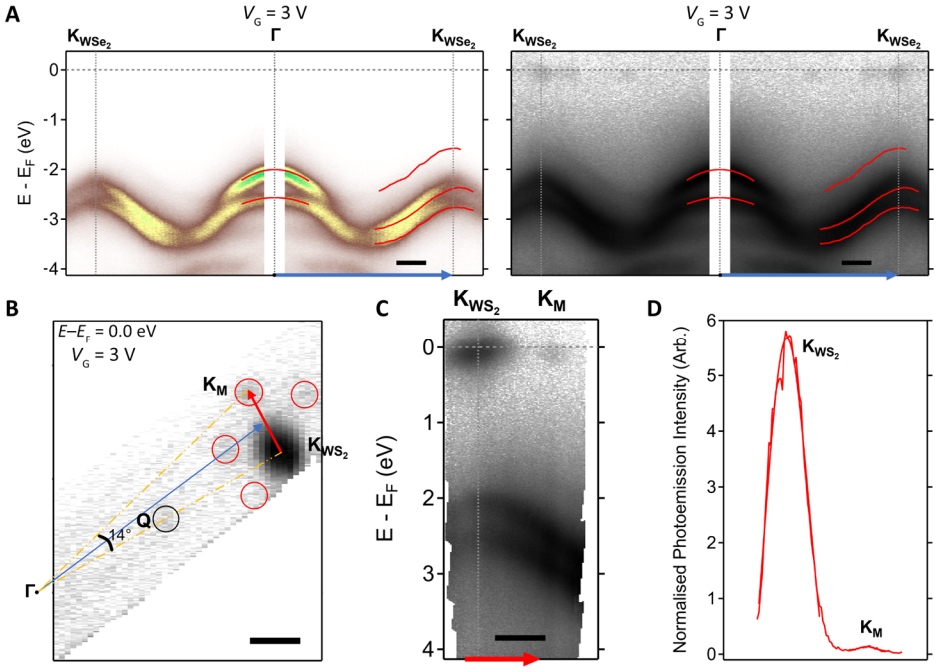

Figure 4.13. Replica conduction features in gated WS_2/WSe_2 with small twist. **A**, energy-momentum slices of WS_2/WSe_2 heterobilayer at 3 V along **Γ**-$\mathbf{K}_{WSe2}$ (**B**, blue arrow). Slices are plotted with a linear color scale (left), and on a log scale (right) to highlight low intensity features. Red lines show peak fits to EDCs from $V_G = 0$V (Figure 4.9) shifted down in energy, Plots are mirrored across **Γ** for clarity. **B**, Constant energy map at the energy of the CBM (WS_2 **K** point), averaged over 0.2 eV and log-scaled. Visible are the CBE at **Q** (black circle) and replica conduction features (red circles). **C**, intensity vs. k line cut from **B** taken along $\mathbf{K}_{WSe2}$ to $\mathbf{K}_M$. **C**, log-scaled *E-k* spectra from $\mathbf{K}_{WSe2}$ to $\mathbf{K}_M$ (**B**, red arrow) at 3 V. All scale bars, 0.2 Å^{-1}

perhaps, three features near E_F: one at $\mathbf{K}_{WSe_2}$, one near $\mathbf{Q}_{WSe_2}$, and one in between. These features are all extremely faint, visible only when intensity is log-scaled. To illuminate their origins, a constant energy slice at the Fermi energy is plotted in Figure 4.13**B**. The strong feature from the WS_2 conduction band can be identified readily. It overlaps with the line connecting **Γ** to $\mathbf{K}_{WSe_2}$ (upper yellow line) determined in Figure 4.9**A**. This explains the observed intensity at $\mathbf{K}_{WSe_2}$ as not coming from the WSe_2 itself and rules out measurement of the conduction band offset from these spectra. Similarly, a cluster of photoemission (circled in black) can be observed centered on the line connecting **Γ** to $\mathbf{K}_{WS_2}$ (lower yellow line), i.e., at $\mathbf{Q}_{WS_2}$. As the TMD **Q**-points are closer together than the **K**-points, the intensity at $\mathbf{Q}_{WSe_2}$ also can be ascribed to the WS_2.

The remaining feature in Figure 4.13**A** resembles three others in the vicinity of the TMD zone corners (all circled in red). They all lie on corners of a hexagon centered on the WS_2 **K**, like the replicated features observed in the previous section with monolayer hBN and are on average ~0.3 $Å^{-1}$ away from $\mathbf{K}_{WS_2}$. Figure 4.13**C** is an *E* - *k* cut through $\mathbf{K}_{WS_2}$and the brightest feature, labeled $\mathbf{K}_M$, which shows that the feature is indeed localized to near E_F, albeit with ~100 times lower intensity (Fig. 4.13**D**). These features are thus consistent with being replicas of the WS_2 CBM, with positions described by Eq. 4.1 (using the location for $\mathbf{K}_{WSe_2}$ from Fig. 4.9).

4.4.4 *Summary and discussion*

To recap, Device 10 is a heterobilayer of ML WS_2 on ML WSe_2 with a twist angle of ~8° as determined by PRM and ARPES of the valence bands. By gate doping the heterobilayer, we were able to populate both the WS_2 CBM at $\mathbf{K}_{WS_2}$ and CBE at $\mathbf{Q}_{WS_2}$, and determined their energy offset as 17 $\pm$ 1 meV. Photoemission from the WSe_2 CBM was never resolved, implying that the band alignment between these monolayers is Type II.

Interestingly, while no replicas of the TMD valence bands were observed, multiple replicas of WS_2 CBM were seen. These were about 0.3 $Å^{-1}$ translated from the original feature and located consistently with the model for replication for this twist as seen in the previous section with hBN on TMDs. As these features do not cross any other bands, we cannot look for anti-crossings as proof-positive of moiré effects. However, ARPES of the graphene-capped heterobilayer reveals replication of the graphene Dirac point by a wavevector that is wholly inconsistent with the difference vector between the graphene and either of the TMDs present.

Instead, it is similar to that of the TMD replicas. Replication of the graphene bands by the TMD/TMD difference vector, $\mathbf{G}_{\mathrm{D}}^{\mathrm{TMD}}$, as has been observed in Ref.[183], cannot be the result of diffraction. Instead, it must originate from a moiré superperiod from the TMD heterobilayer folding the graphene into a MBZ. The presence of a strong (moiré) interaction between the incommensurate TMD layers is further evinced by a large modulation of the bands at $\boldsymbol{\Gamma}$. We note though that the graphene replication vector is about 0.4 $Å^{-1}$, which is longer than but still within uncertainty of $\mathbf{G}_{\mathrm{D}}^{\mathrm{TMD}}$. Unfortunately, due to constraints on beam time, the TMD VBM were not measured with the replicated graphene to directly measure the local twist angle. Nevertheless, to the author's knowledge this is the first report of moiré of TMD conduction bands, and the first strong evidence of moiré effects in an incommensurate structure at relatively large twist.

Substantial additional work can be done in this system. For example, here the WSe_2 VBM became too broad to resolve when heterobilayer became conducting, and so the band gap could not be measured. This could be remedied by reversing the TMD order, placing the WSe_2 on top to increase the photoemission from its derived bands relative to the WS_2. Additionally, the data presented here could be further analyzed to search for renormalization, as was seen in gated ML WSe_2, which would modulate the alignment of the valence bands.

4.5 Other TMD/TMD heterobilayers

Having studied Device 10 in detail we now turn to others that, due to limited beam time, have not been as fully investigated but each provide additional pieces of evidence for moiré effects in the band structure of twisted TMDs.

4.5.1 *WS_2 on WSe_2 with nearly zero twist*

Figure 4.14**A** is an optical image of Device 11, which has AFM cut graphene on top of WS_2 on WSe_2. Both flakes happened to have monolayer and bilayer regions, and they were stacked ML-on-ML, and 2L-on-2L. A SPIM map at $V_G = 0$ confirms that the graphene is contiguous (Fig. 4.14**B**). The monolayer crystal orientations were determined by lin-SHG and stacked to be aligned (mod 60°). The alignment was confirmed by PRM (Fig. 4.14**C**), the FFT of which reveals a maximum moiré period of ~8 nm (Fig. 4.14**D**), which corresponds to a twist angle $\theta < 1°$. However, there is also a minor period of ~6 nm ($\theta \sim 2°$), indicating that the moiré is strained. The

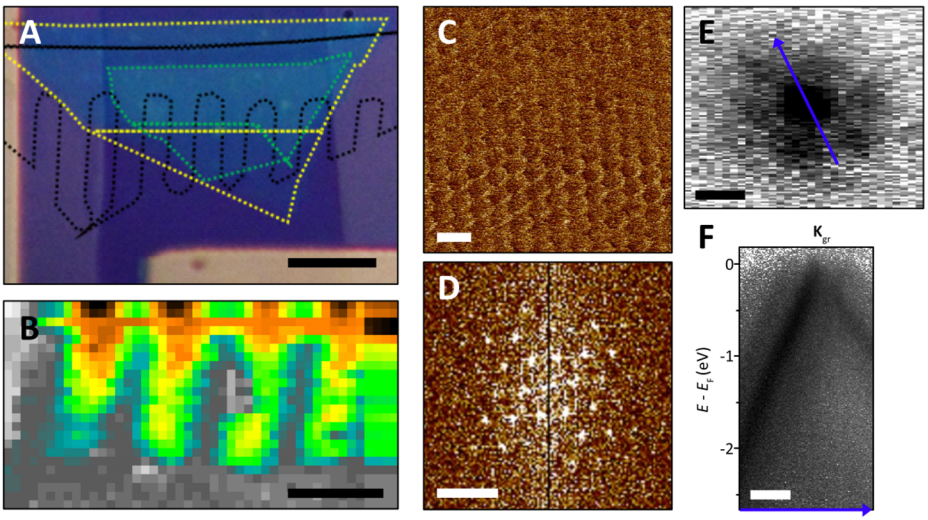

Figure 4.14. Replica bands in graphene on a low-twist WS_2 on WSe_2 heterobilayer. **A**, optical image of Device 11, outlining the graphene (black), ML and BL WS_2 (yellow), and ML and BL WSe_2 (green). Scale bar 10 µm. **B**, SPIM map with $V_G = 0$. **C**, contact-resonant PFM of ML-on-ML region, scale bar 10 nm. **D**, 2D FFT of **C**, scale bar 5 nm. **E**, constant energy map around $\mathbf{K}_{gr}$, and **F**, log-scaled *E* - *k* spectra across $\mathbf{K}_{gr}$ (**E**, blue arrow) at 0 V. Scale bars in **E** and **F**, 0.1 $Å^{-1}$.

Fermi surface about $\mathbf{K}_{gr}$ reveals a hexagonal pattern of spots (Figure 4.14**E**), and an *E-k* slice through the graphene **K** (Fig. 4.14**F**) shows that these spots are replica Dirac points. There is also a weak secondary replica Dirac cone visible at the edge of the slice. The replica Dirac point closest to $\mathbf{K}_{gr}$ is ~0.1 $Å^{-1}$ away, which is consistent with the TMD layers being aligned within 1°. However, the TMD bands in the exposed regions were relatively weak, and no replica valence bands were observed. Additionally, we were unable to dope the sample to conduction in either of the 2L-on-2L or the ML-on-ML regions.

4.5.2 *WS_2 on $MoSe_2$ with large twist*

WSe_2 and $MoSe_2$ are closely lattice matched, and so the $WS_2/MoSe_2$ heterobilayer system should be similarly incommensurate to the case of WS_2/WSe_2. Figure 4.15**A** is an optical image

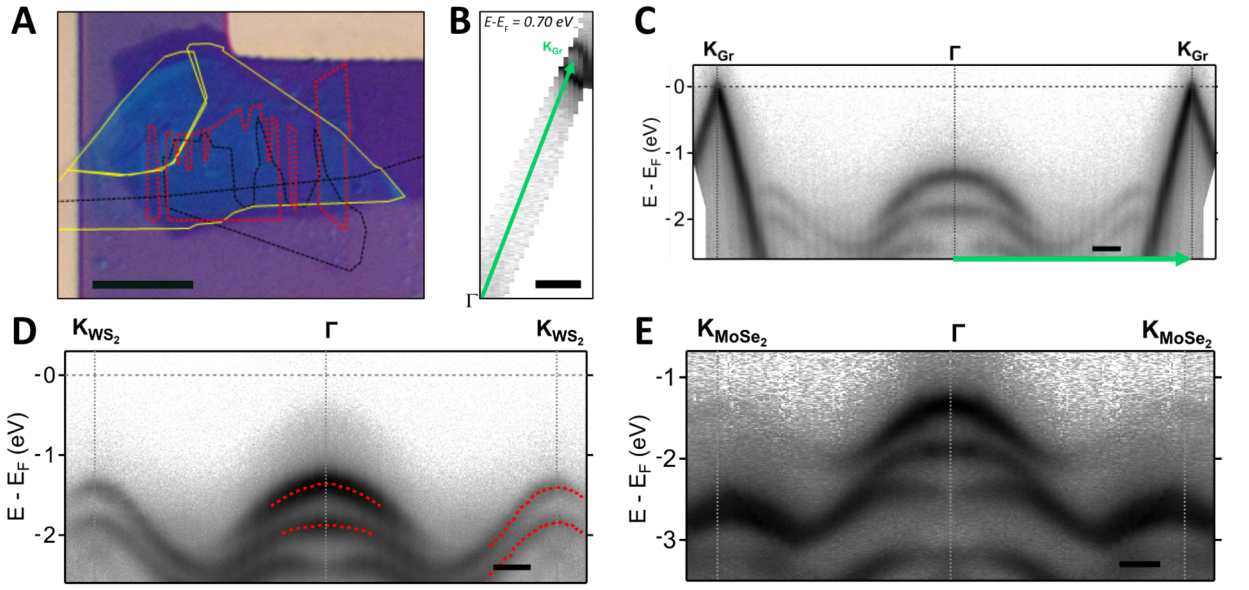

Figure 4.15. Ungated characterization of WS_2 on $MoSe_2$. **A**, optical image of Device 12, outlining the graphene (black), ML WS_2 (yellow), and ML WSe_2 (red). Scale bar 10 µm. **B**, constant energy map ($E - E_F = 0.70$ eV) and **C**, *E-k* slice between **Γ** and $\mathbf{K}_{gr}$ (**B**, green arrow) from graphene on heterobilayer. **D** and **E**, *E-k* spectra from heterobilayer region between **Γ** and **K** points of WS_2 and $MoSe_2$, respectively. Fitted Lorentzian peaks to EDCs overlaid on **D** (red points). All spectra log-scaled, and *E-k* slices mirrored. Scale bars in **B**-**E**, 0.2 $Å^{-1}$.

of Device 12, which has AFM cut graphene on ML WS_2 on ML $MoSe_2$. The crystal axes were determined by SHG and stacked to be ~30° rotated. No lateral PRM contrast was resolved anywhere on the sample, as would be expected for such a large twist. As was seen in Device 10 (*cf.* Figure 4.10), ARPES spectra from the capping graphene (Figure 4.15**B** and **C**) shows strong bands lacking a dark corridor, which indicates breaking of the graphene sublattice symmetry. No graphene replicas were observed in any of the measurements, also as expected given the large TMD/TMD twist angle and large $\mathbf{G}_D$[183].

The TMD **K** points in the uncapped region were determined via constant energy maps at the TMD VBMs as usual, revealing a relative twist of $35° \pm 1°$. Ungated *E* - *k* slices through **Γ** and each **K** point are shown in Figure 4.15**D** and **E**. No clear valence band replicas were observed. As was the case with WSe_2, the lowest energy valence bands around the zone boundary are derived from the $MoSe_2$ and are of diminished intensity due to the stacking order. Unfortunately, the $MoSe_2$ bands are too faint to accurately determine their effective masses or the energies of their maxima. Both the VBM at **Γ** and WS_2-derived VBE at $\mathbf{K}_{WS_2}$ are well resolved and the standard fitting procedure extracts band parameters (at $V_G = 0$) listed in Table 4.2.

	m^*/m_e
Upper **Γ**	0.91 ± 0.02
Lower **Γ**	2.10 ± 0.07
Upper $\mathbf{K}_{WS_2}$	0.63 ± 0.02
Lower $\mathbf{K}_{WS_2}$	0.54 ± 0.04

Table 4.2. Measured effective masses in a $WS_2/MoSe_2$ heterobilayer with $V_G = 0$. Values extracted from bands observable in Figure 4.15, from peak positions of Lorentzian fits to EDCs.

As was the case with Device 10 (*cf.* Table 4.1), the effective masses at **K** are comparable to those from the isolated monolayers while those at **Γ** are quite different, indicating (strong) orbital-overlap dependent hybridization (*cf.* Table 3.1 and Figure 2.6).

We now consider the conduction bands in this device after applying a gate voltage $V_G = 2.5$ V. From the shifting of the bands, Equation 3.2 gives the corresponding doping as $n_G(2.5\text{ V}) = 8.9 \pm 0.9 \times 10^{12}\text{cm}^{-2}$. Figure 4.16**A** and **B** are *E-k* slices along the same directions as Figure 4.15**C** and **B** respectively. The slice through $\mathbf{K}_{WS_2}$ shows a conduction band feature $\mathbf{K}^{CB}_{WS_2}$ at the WS_2 zone corner. Interestingly, the slice through $\mathbf{K}_{MoSe_2}$ shows photoemission from both the zone corner $\mathbf{K}^{CB}_{MoSe_2}$, and between **K** and **Q**. Constant energy maps through E_F confirm that all three are isolated spots rather than stray counts. That the CBEs are simultaneously observable at the individual **K** indicates that the CBM in $MoSe_2$ and WS_2 are nearly energy degenerate. Though all three were observed at all nonzero V_G probed, that the intensity of $\mathbf{K}^{CB}_{WS_2}$ is uniformly weaker than $\mathbf{K}^{CB}_{MoSe_2}$ despite the stacking order indicates the $MoSe_2$ CBM is at marginally lower energy.

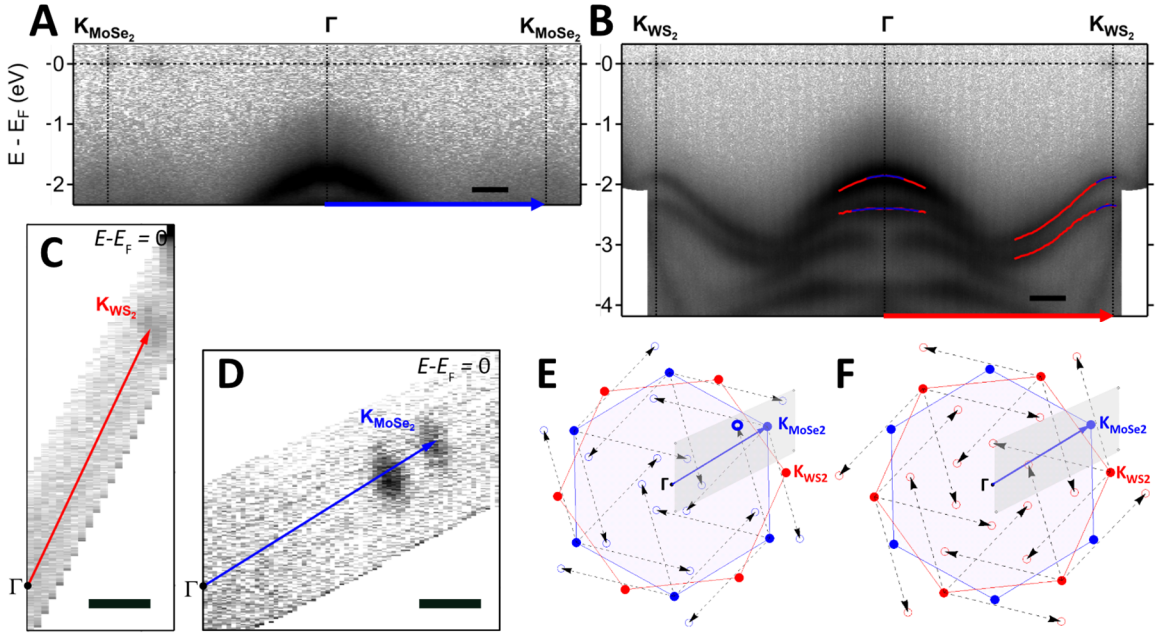

Figure 4.16. Conduction bands in WS_2 on $MoSe_2$. **A** and **B**, *E-k* slices between **Γ** and (**A**) $\mathbf{K}_{MoSe_2}$, and (**B**) $\mathbf{K}_{WS_2}$ with overlaid fitted band (red) and dispersions (blue). **C** and **D**, constant energy maps at $E - E_F = 0$. Spectra in **A-D** taken at $V_G = 2.5$ V and log-scaled. Scale bars 0.2 Å^{-1}. **E** and **F**, schematics of the BZs in 35° twisted $MoSe_2$ (blue) and WS_2 (red) with overlaid translations by $\mathbf{G}_D$ of the $MoSe_2$ **K** point (**E**) and the WS_2 **K** point (**F**). Parallelograms mark region probed in **D**.

The third feature can be seen in Figure 4.16**D** as overlapping but centered off the line between **Γ** and $\mathbf{K}_{\mathrm{MoSe_2}}$, and with higher intensity than $\mathbf{K}^{\mathrm{CB}}_{\mathrm{MoSe_2}}$. A schematic of where Equation 4.1, predicts folding of $\mathbf{K}^{\mathrm{CB}}_{\mathrm{MoSe_2}}$ (Figure 4.16**E**) qualitatively reproduces the location of this extraneous feature, $\mathbf{K}^{\mathrm{M}}_{\mathrm{MoSe_2}}$. If this is indeed a moiré replica, then it is from a remarkably large $\mathbf{G}_{\mathrm{D}}$, comparable to that between hBN and TMDs. Notably, that $\mathbf{K}^{\mathrm{M}}_{\mathrm{MoSe_2}}$ may be folded from a different $\mathbf{K}^{\mathrm{CB}}_{\mathrm{MoSe_2}}$ than the one seen in the map may explain the discrepancy in intensities. However, the models for folding of $\mathbf{K}^{\mathrm{CB}}_{\mathrm{MoSe_2}}$ and $\mathbf{K}^{\mathrm{CB}}_{\mathrm{WS_2}}$ (Fig. 4.16**F**) predict multiple other replicas within the areas of **k**-space studied in Figure 4.16**C** and **D** that were not observed. It is perhaps not surprising that replicas of the latter were not seen given the already low intensity from $\mathbf{K}^{\mathrm{CB}}_{\mathrm{WS_2}}$.

4.5.3 *WSe_2 and $MoSe_2$ at finite twist*

This section concludes by returning to the combination discussed back in Chapter 2, ML WSe_2 and ML $MoSe_2$. There, we addressed in detail the case of close alignment, which permits the formation of commensurate domains. This then produces three apparent bands at **Γ** comprising two pairs of hybridized bands with different splittings that serendipitously partly overlap. Only briefly touched upon was the finite twist-angle case, where hybridization at **Γ** was still observed but at a substantially reduced degree. Here we will discuss two devices (with functional gates) combining these monolayers wherein only two bands at **Γ** were observed, indicating incommensuration. These devices have the monolayers stacked in opposite orders, thereby potentially enabling comparison of band alignment shifting due to the Stark effect. This is because the CBM is (expected) to be in the $MoSe_2$, i.e., gate-induced charges will be localized there regardless of the stacking. The graphene-covered regions in these devices were not studied due to time constraints.

Figure 4.17**A** is an optical image of Device 13, which has graphene partially capping ML $MoSe_2$ on ML WSe_2. The graphene naturally had a 2 um wide crack as exfoliated, and the device was laid out to position heterobilayer region within the gap. Constant energy maps through the two TMD VBM energies, $E^{VBM}_{MoSe_2}$ and $E^{VBM}_{WSe_2}$ are used to determine the **K** points of the two layers and their relative angle. This was done via measurements where the layers were isolated (Fig. 4.17**B**) and stacked (Fig. 4.17**C**). Surprisingly, $\mathbf{K}_{WSe_2}$ and $\mathbf{K}_{MoSe_2}$ were found to be ~5° apart from the individual layers, but were indistinguishable in the heterobilayer, i.e., $\mathbf{K}_{WSe_2} \sim \mathbf{K}_{MoSe_2} \equiv \mathbf{K}$.

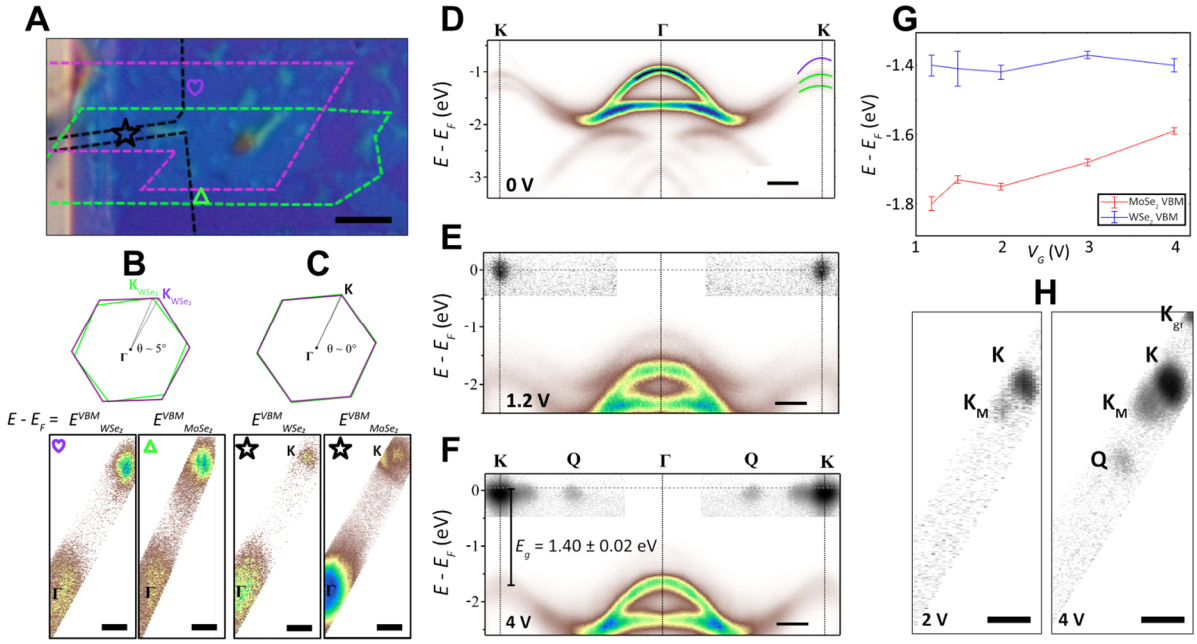

Figure 4.17. Bands in twisted $MoSe_2$ on WSe_2. **A**, optical image of Device 13 outlining the graphene (black), ML $MoSe_2$ (green), and ML WSe_2 (pink). Scale bars 5 µm. **B** and **C**, (bottom) constant energy maps at WSe_2 and $MoSe_2$ CBMs taken at points labeled in **A** with exposed WSe_2 (heart), exposed $MoSe_2$ (triangle), and heterobilayer (star). Above are schematic BZs of WSe_2 and $MoSe_2$ showing angular alignment extracted from constant energy maps. **D-G**, *E-k* slices through apparent shared **K** point in heterobilayer at $V_G = 0$, 1.2 V, and 4 V. Spectra in color are linearly scaled, those in grayscale are log-scaled. Faint low energy valence bands in **E** are due to accidental overlap with the graphene-capped region. **G**, fitted energies of WSe_2 and $MoSe_2$ VBMs in the heterobilayer vs. V_G when the conduction band is observable. **H**, constant energy maps through E_F at $V_G = 2$ V and 4 V. Scale bars in **B-F, H**, 0.25 $Å^{-1}$.

An energy-momentum slice between **Γ** and the shared **K** at $V_G = 0$ reveals sharp bands with two low energy bands at **Γ** and three observable bands at **K** (Fig. 4.17**D**). As previously seen in Chapter 2, the lower branches of the WSe_2 and $MoSe_2$ spin-split bands at **K** overlap without hybridizing. Since the $MoSe_2$ is above the WSe_2, the counts from the apparent lowest energy band we take to come from the $MoSe_2$. Gating the sample produces a measurable signal near the Fermi energy around **K** (Fig. 4.17**E**). Equation 3.2 gives the minimum doping required as $n_G^{\min} \leq 0.96 \pm 0.05 \times 10^{12}$ cm^{-2}. That the VBM is also at **K** confirms that the gap is direct here.

Further doping the sample to $n_G = 9.0 \pm 0.4 \times 10^{12}$ cm^{-2} populates the **Q** point (Figure 4.17**F**). The energy offset between the **K** and **Q** CBE cannot be directly inferred from these data as was done for Device 10 because the dispersion at **K** was not resolved here. However, the offset can be estimated by assuming that **Q** was only just populated at $V_G = 3$ V (spectra not shown here) and taking the conduction band effective mass as that of $MoSe_2$ from theoretical predictions[147], $m^*_{CBM}/m_e \sim 0.15$. This yields $E_{\mathbf{Q}}^{CBE} - E_{\mathbf{K}}^{CBM} = 28 \pm 5$ meV.

In this device, we were able to resolve the highest energy valence bands at **K** derived from both monolayers even when the device is gated. As usual then, we extracted the effective masses and VBM energies from each layer, $E^{VBM}_{MoSe_2}$ and $E^{VBM}_{WSe_2}$ via fitting parabolic dispersions to the band positions in E - k (determined by fitting Lorentzians to EDCs) at each gate voltage where the conduction band is observed. The effective masses were not found to vary significantly and agreed with the values from Figure 2.6. The two **Γ** band edge energies were extracted similarly. Their offset – a measure of interlayer coupling – is nearly independent of V_G, averaging 0.66 ± 0.02 eV.

Plotting VBM energies vs. V_G (Figure 4.17**G**) reveals that while the WSe_2-derived upper band at **K** is also independent of V_G, that of $MoSe_2$ changes roughly linearly. This follows from the assignment of the CBM to $MoSe_2$, as doping the heterobilayer into conductance implies the

induced charges are localized to the $MoSe_2$. Any band gap renormalization in the system should thus predominantly occur in the $MoSe_2$. The decrease in binding energy is ~200 meV over the gate voltage range studied, comparable to what was seen for ML WSe_2 in Chapter 3 (*cf.,* Fig. 3.7). Since the global VBM is WSe_2-derived, this implies that the band gap E_g is not substantially varying with gate voltage, averaging $E_g = 1.40 \pm 0.06$ eV.

Regarding possible Stark shifting of the bands, we first note that in this device the $MoSe_2$ is on the opposite side of the WSe_2 than the hBN dielectric/graphite gate. Since induced charge must go into the $MoSe_2$, this means the electric field must pass through both the WSe_2 and hBN before reaching the $MoSe_2$, *i.e.*, the ML WSe_2 and hBN function as a composite dielectric (as discussed in section 3.4). A schematic of the potential landscape is shown in Figure 4.18.

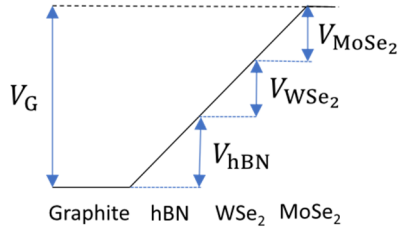

Figure 4.18. Schematic potential landscape in a gated $MoSe_2$ on WSe_2 heterobilayer.

In this model, the hBN and WSe_2 are at different electrostatic potentials due to voltage drops V_{hBN} and V_{WSe_2}. These plus the drop through the $MoSe_2$, V_{MoSe_2}, must sum to the gate voltage V_G. V_{MoSe_2} is equal to the shifting of the $MoSe_2$-derived bands due to the gate, provided we ignore any hybridization effects. That is, we have $V_{MoSe_2} = \Delta E^{VBE}_{\boldsymbol{K}_{MoSe2}}$. The electric-field induced shifting of the WSe_2 bands to larger binding energy relative to the $MoSe_2$, i.e. the Stark shift, is given by $V_{WSe_2} = \Delta E^{VBM}_{\mathbf{K}_{WSe2}} - \Delta E^{VBE}_{\mathbf{K}_{MoSe2}}$. This leaves $V_{hBN} = V_G - \Delta E^{VBM}_{\mathbf{K}_{WSe2}}$. Applying these formulae to the shifts observed in our spectra yield value smaller than their uncertainties for all V_G except the highest voltage, $V_G = 4$ V. There, we measure $V_{WSe_2}(4\text{ V}) = 0.12 \pm 0.03$ V. Modeling the layers as capacitors in parallel and using the dielectric constants derived in section 3.4 yields an estimated shift of $V^{model}_{WSe_2}(4\text{ V}) = 0.14 \pm 0.01$ V, with which our measured value agrees.

Finally, while no replicated valence bands were observed at any V_G, one replicated CBM feature was seen in this device. It is close to **K** and became measurable at $n_G = 3.5 \pm 0.2 \times 10^{12}$ cm^{-2}. (Fig. 4.17**H**). Its position is consistent with our model (Eq. 4.1) with a twist angle θ between 2° and 6°. It is unclear why only one of the three expected replicas were observed. Though the area of k-space probed did not include the expected centers of the other two foldings, the intensity/width of the observed feature $V_G = 4$V suggests that the others should have been partly visible.

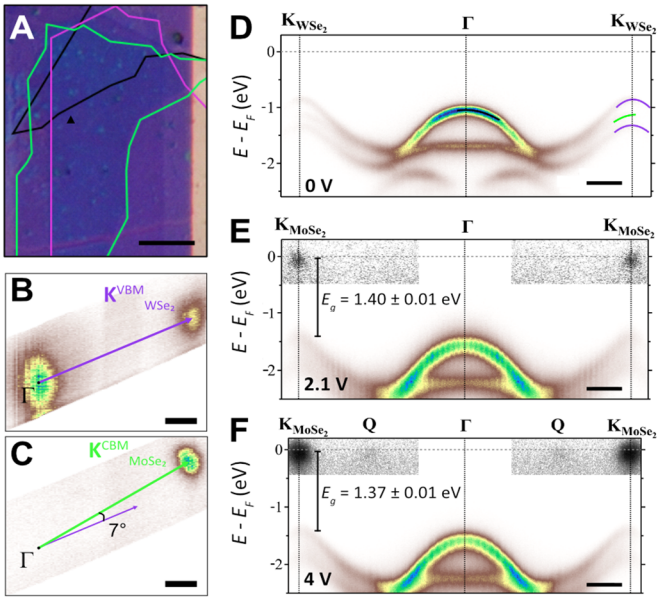

Figure 4.19. Bands in twisted WSe_2 on $MoSe_2$. **A**, optical image of Device 14 outlining the graphene (black), ML WSe_2 (pink), and ML $MoSe_2$ (green). Scale bar, 10 µm. **B** and **C**, constant energy maps at WSe_2 VBM (top) and $MoSe_2$ CBM (bottom). **D-E**, *E-k* slices through labeled **K**-points at V_G = 0, 2.1 V, and 4 V. Spectra in color are linearly scaled, those in grayscale are log-scaled. Scale bars in **B-F**, 0.25 Å^{-1}. All spectra from heterobilayer near graphene (**A**, triangle).

We now turn to the final device in this chapter, Device 14, which comprises graphene partly capping ML WSe_2 on ML $MoSe_2$, shown optically in Figure 4.19**A**. Here, the graphene originally also had a natural few µm-wide gap which did not survive the sample fabrication process. The TMD alignment was determined to be ~7° directly from the heterobilayer region via constant energy maps through the WSe_2 VBM (Fig. 4.19**B**), and the $MoSe_2$ CBM (at finite gate voltage, Figure 4.19**C**). With $V_G = 0$, all the valence bands at **K** are resolvable (Fig. 4.19**D**), and their extracted effective masses agree with those from Device 13 and Figure 2.6. With doping to $n_G = 4.2 \pm 0.5 \times 10^{12}$ cm^{-2}, the CBM was visible at $\mathbf{K}_{MoSe_2}$ (Fig. 4.19**E**). The CBE at $\mathbf{Q}_{MoSe_2}$ is visible at $n_G = 10 \pm 1 \times 10^{12}$ cm^{-2} (Fig. 4.19**F**). No photoemission is seen near E_F at $\mathbf{K}_{WSe_2}$ at

any V_G. The **Γ** band edge energy offset showed no systematic change with V_G, averaging 0.67 ± 0.03 eV. Replica features were observed from neither the valence nor conduction bands.

Thanks to the increased photoemission from the WSe_2 VBM in this device compared to Device 13, the band gap can be more accurately determined. Time only permitted measurement at two gate voltages, $V_G = 2.1$ V and 4 V. A small change was resolved between these spectra, with E_g decreasing from 1.40 ± 0.01 eV to 1.37 ± 0.01 eV. Alas, the $MoSe_2$ **K** bands suffered from the flake being underneath in this geometry, and they became unresolvable when the sample was conducting. Consequently, we have nothing to compare to the renormalization seen with Device 13. For the same reason, we are unable to measure relative shifting of the $MoSe_2$ and WSe_2 bands.

Note that no Stark shifting should be present here, as WSe_2 is on the wrong side of the $MoSe_2$ in this device. Consequently, E_g should be larger here than that in Device 13 by the predicted Stark shift $V_{WSe_2}^{model}$, which is not the case. It is yet unclear whence comes this discrepancy. Though the sample twist angles are slightly different (mod 60°), the interlayer coupling (measured by proxy via the splitting at **Γ**) is consistent between the devices. The hBN dielectrics are of similar thickness (~9.5 nm), ruling out the effect of a relative difference in hBN dielectric constant[185].

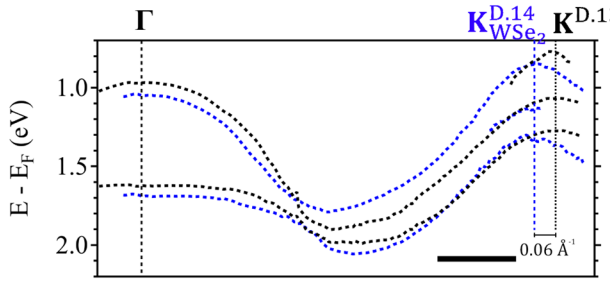

Figure 4.20. Band positions from Devices 13 (black) and 14 (blue) fitted from *E-k* slices between **Γ** and **K** point of WSe_2 in Device 14 ($\mathbf{K}_{WSe_2}^{D.14}$) and heterobilayer **K** point in Device 13 ($\mathbf{K}^{D.13}$). Scale bar, 0.25 Å^{-1}.

To perhaps shed some light on this, we plot the fitted *E-k* from each devices from **Γ** to their respective VBM in Figure 4.20. Surprisingly, the shared **K** in Device 13, $\mathbf{K}^{D.13}$, is ~0.06 Å^{-1} farther out than the **K** of an isolated ML would be (~1.26 Å^{-1}). This implies a substantial reconstruction which may be the result of Device 13 being stacked differently[186], with the layers' armchair axes

anti-aligned (twist ~ 60°). This may change the average interlayer distance and therefore the capacitive model, as well as the interlayer coupling which, though small, is nonzero at the **K** point and may have unanticipated dependence on the electric field or doping. This would impact the comparability of these devices and so underlines a less visible facet of twisting. We note that there is also a Stark shift occurring in the graphene-capped region. This would be significantly more difficult to study, as the added layer would diminish the TMD signal at **K**. This would likely preclude observation of those bands from the bottom TMD, necessitating study of at least two devices with opposite stacking orders (but with similar absolute angular alignments).

4.6 Summary and Discussion

The varied results presented in this chapter hopefully further highlight how uniquely positioned μ-ARPES is for probing twisted systems. With ML hBN on TMDs, twisting produces a striking mélange of folded features. While the lack of observed anticrossings points to diffraction rather than moiré effects, it could be limited by the measurement resolution. As this device geometry is perhaps the most direct for enabling ARPES with air-sensitive compounds like WTe_2, further study is warranted to fully resolve this question. If these results are indeed from diffraction, hopefully it will clarify the importance of caution when applying ARPES to twisted 2D structures.

With twisted TMD bilayers, in contrast, that the twisting of TMDs generates folding of the bands in proximal graphene indicates the presence of a moiré superpotential. That no folding of the TMD valence bands was seen is a standing mystery, as is whether the graphene folding is due to a moiré effect on the Dirac dispersion itself or diffraction off of the moiré potential. Here. i*n-situ* gating again has proven itself invaluable. By providing access to conduction states and their moiré replicas, it sheds light on the alignments in these heterobilayers and how they may yet be engineered by doping, electric field, and, naturally, with twisting.

Chapter 5. μ-ARPES OF A MONOLAYER TOPOLOGICAL INSULATOR

An increasing number of the known 2D systems are proving to be sensitive to air, water and/or heat when thinned down to the atomic limit. Despite the consequent difficulty of study these materials attract a tremendous amount of scientific attention as they display a vast variety of exotic behaviors. The theoretical models of these exotic materials are often at odds with the experimental observations. This naturally demands direct study of the underlying physics to clarify the discrepancy. For example, calculations of the interlayer magnetic coupling in CrI_3 initially predicted that the lowest-energy bilayer form would be ferromagnetic in contrast to optical studies showing[187] layered-antiferromagnetism. More thorough modeling has since revealed that the metastable monoclinic stacking of CrI_3 produces antiferromagnetic coupling[188], a prediction supported by subsequent spin-polarized STS[189].

The nature of the band gap in ML WTe_2 has similarly been at the center of scientific back and forth. Its first theoretical treatment[86] predicted it as the only TMD to be a topological semimetal in its stablest polytype. This was contrast to transport measurements[91,92] showing a semimetal-insulator transition at low temperatures. Subsequent low temp. ARPES and STS measurements[95,96] revealed a gap of ~50 meV. More recent band structure calculations have since predicted a band insulator phase with a similar gap opening via SOC[95,190]. Yet later transport and STS experiments have suggested that the insulator state is not from an intrinsic band gap, but instead forms from either electron localization due to defects (a Coulomb gap)[191] or, more exotically, the formation of an excitonic insulator phase[98]. In this chapter, we will consider gated, temperature dependent μ-ARPES of ML WTe_2 to address this controversy. Along the way, we will demonstrate how our sample design enables gate-tunable μ-ARPES of air-sensitive materials.

5.1 Sample preparation

The materials we have studied so far are all air- and water-stable, compatible with post-transfer cleaning in standard solvents under ambient conditions (even only minimally encapsulated or not encapsulated at all). They are similarly relatively stable under UHV annealing at high temperature before ARPES measurement. In comparison, ML WTe_2 devices prepared for transport studies have historically been fully encapsulated with at least few-nm thick hBN with no reports of post-transfer annealing for fear of compromising the WTe_2.

The first attempt at ARPES study of ML WTe_2 to the author's knowledge was his own, done at Spectromicroscopy using a sample geometry like that of Chapter 2. These samples were prepared by dry transfer inside a glovebox with a N_2 atmosphere, and O_2/H_2O levels both below 0.1 ppm. However, they were taken outside of the glovebox and solvent cleaned like the TMD samples, in chloroform and IPA (stored under ambient conditions) for upwards of 12 hours. They were then annealed in forming gas at up to 275° C for at least an hour, and annealed again in the ARPES chamber at up to 300° C.

An example sample that has both monolayer and multilayer regions is shown in Figure 5.1**A**. μ-ARPES was done in both regions with $h\nu = 74$ eV, and at two different temperatures,

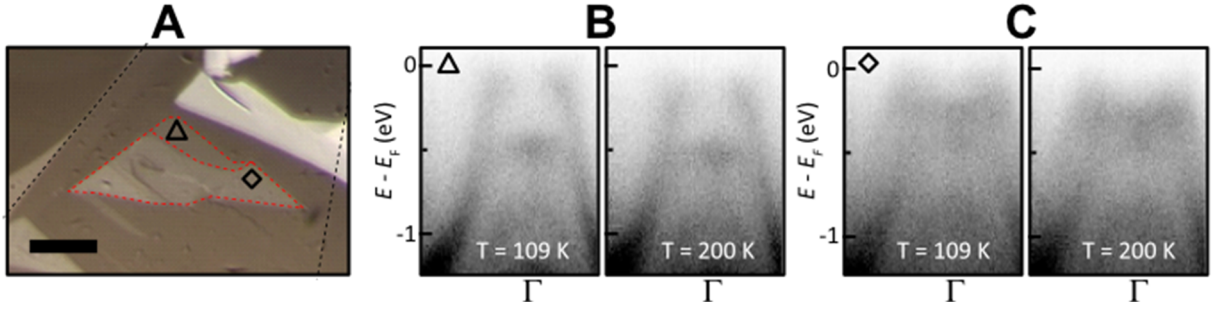

Figure 5.1. Temperature dependent μ-ARPES of ML WTe_2 at Elettra. **A**, optical image of a sample with graphene (dashed black outline) on WTe_2 with ML and multilayered regions (dashed red) on graphite on Si. Scale bar, 10 μm. **B** and **C**, *E-k* slices between **Γ** and **Y** of ML WTe_2 (**B**, triangle in **A**) and multilayer WTe_2 (**C**, diamond in **A**) at T = 109 K and 200 K.

109 K and 200 K. In the ML spectra taken along **Γ** – **Y** (Figure 5.1**B**), photoemission is only seen from the wings of the valence band about **Γ**, and the VBM is not directly observed. This is consistent with the predicted orbital character of the low energy bands[192]. Combined with the mostly P-polarization of the excitation at Spectromicroscopy, this causes the matrix element in the immediate vicinity of **Γ** to vanish. There is an increase in photoemission near E_F at 109 K compared to 200 K, and it is localized at momenta consistent with the expected positions of the electron pockets. However, from neither these energy-momentum slices nor constant energy slices are the electron pockets distinguishable. Consequently, the gap is not resolvable from these data. The multilayer spectra (Figure 5.1**C**) is of similar resolution, and compares poorly not only to our other data from other bulk samples (*cf.* Figure 2.2) but to other reports of ARPES from WTe_2[193] as well. This indicates an underlying problem with the experiment, perhaps from the sample preparation exacerbated by the comparably low flux and fixed excitation energy at Spectromicroscopy.

Our next opportunity to study WTe_2 was at MAESTRO which offered multiple advantages. Notably, the beamline has an integrated glovebox in which sample stored under dry conditions can be loaded directly into the ARPES chamber. To keep the sample from contacting water or air, the sample processing protocol was modified to use anhydrous solvents inside of a glovebox. The sample was sealed inside of a ConFlat™ (CF) flanged cap couplet for transport to MAESTRO

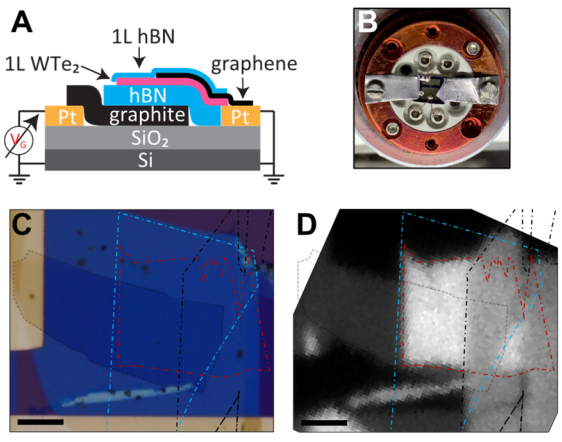

Figure 5.2. A large area gated ML WTe_2 device. **A**, device schematic. **B**, image of Device 15 mounted to MASTRO sample puck with contacts. **C** optical image and **D,** SPEM map of Device 15 with ML hBN (dashed blue outline) on graphene (dashed black) partially overlapping ML WTe_2 (dashed red). SPEM was integrated at E_F and **Γ** highlighting ML hBN/WTe_2. Scale bars, 10 μm.

glovebox-to-glovebox. Furthermore, MAESTRO offers variable excitation polarization and energy. Figure 5.2**A** shows a schematic of the device geometry used, which is like the one introduced in Chapter 3. The sample mounts at MAESTRO are round pucks, designed to facilitate automated sample loading. It is adapted for gating by replacing the center with an alumina plate screwed through which are eight stainless steel bolts. These bolts contact to external leads on the other side of the puck. While it is possible to wire-bond from a sample substrate (mechanically affixed to the alumina face) to these bolts using aluminum wires, we did not have access to wire-bonding under dry conditions. Consequently Device 15 was wired to the bolts using silver paste (Figure 5.2**B**). To leave open the possibility of measuring in both ARPES endstations, the device was designed to have a 12 × 12 μm area of WTe_2 over the gate and capped with only ML hBN (Figure 5.2**C**). A SPEM map of the sample in nano-ARPES (with the gate grounded) taken at 67 K shows uniform, bright photoemission intensity over this area.

5.2 Measurements in Micro-ARPES

Our first measurements were taken in microARPES after UHV annealing at up to 210° C for several hours. After cooling the sample stage down to 15 K, rough *E-k* maps with 72 eV excitation were taken to identify the WTe_2 orientation relative to the detector slit axis. This energy

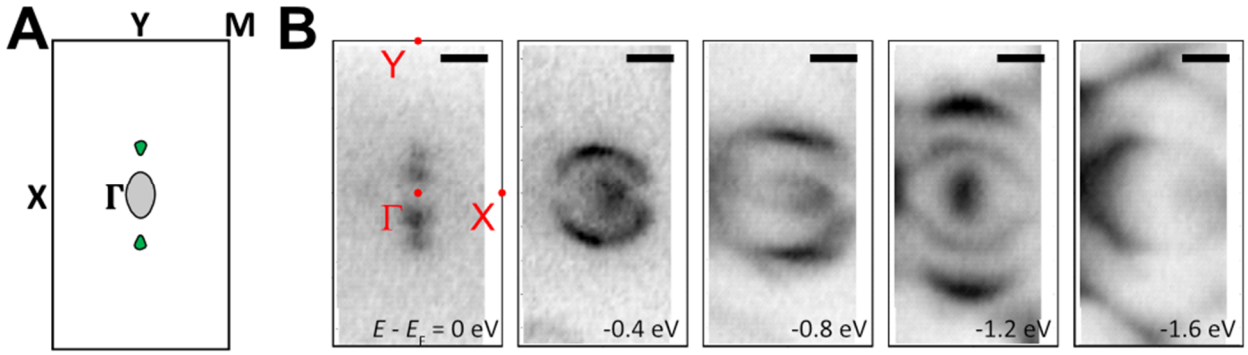

Figure 5.3. Constant energy maps through WTe_2 at 15 K. **A**, schematic Fermi surface and first Brillouin zone of ML WTe_2. **B**, constant energy maps in the first BZ at 15K with 72 eV LH-polarized excitation averaged over energy windows of 0.1 eV. Scale bars, 0.25 $Å^{-1}$.

was reported in the literature to maximize the photoemission cross section[95]. The analyzer was then manually rotated to align the slit with the WTe_2 **Γ-Y** axis and through the electron pockets (Figure 5.5**A**) and a fine *E* - ***k*** map taken within the first Brillouin zone with a pass energy of 50 eV and linear horizontal (LH) polarization. The Fermi energy was determined here from the background away from **Γ**, and agreed with the E_F measured from the platinum ground electrode. The constant energy cut through this map at $E - E_F = 0$ (Figure 5.5**B**) averaged over a 0.1 eV window shows a four spots of photoemission along **Γ**-**Y**, with the center two curving inwards and forming ellipses. Cuts at lower binding energy, such as at $E - E_F = -0.8$ eV and -1.6 eV show modulations of the photoemission intensity between otherwise symmetric points in ***k***-space.

5.2.1 *Polarization dependence and matrix elements*

An *E* - *k* slice through this map along **Γ**-**Y** (Figure 5.4**A**) shows a valence band centered on the Brillouin zone that curves sharply near **Γ**, going nearly flat before vanishing. Just farther out from where the valence band seemingly kinks are two pockets of photoemission where the conduction band's electron pockets are expected[86]. These pockets and the two flat segments from

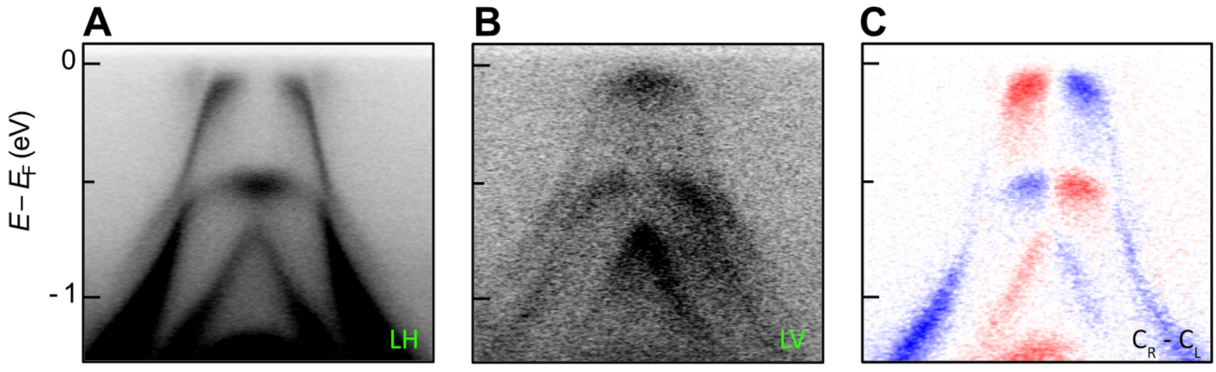

Figure 5.4. Excitation polarization dependence of WTe_2 spectra in μ-ARPES. **A**-**C**, *E*-*k* spectra of WTe_2 along **Γ**-**Y** taken at microARPES with T = 15 K using linear horizontal (LH, **A**), linear vertical (LV, **B**), circular right (C_R) and left (C_L) excitation. **C** plots the difference between spectra with C_R and C_L.

the valence band are the four spots of photoemission seen as the apparent Fermi surface from Figure 5.5**B**. *E* - *k* snaps were taken along the same line and with comparable integration times as in Figure 5.4**A** using linear vertical (LV), circular right (C_R) and circular left (C_L) polarized excitation. Figure 5.4**B** shows the LV data, wherein no conduction band-like features can be seen. Instead, the entirety of the valence band can be seen with maximal intensity at **Γ**. The signal-to-noise ratio here is distinctly worse than in Figure 5.4**A** due to a substantially lower flux.

The spectra in Figure 5.4**A** and **B** are consistent with the literature, such as ref[95] which showed polarization dependence of the ARPES spectra. The matrix element for photoemission vanishes when the parity (with respect to reflection across the mirror plane defined by the sample surface normal and the excitation light path) of the excitation and the orbital character of the initial electron state differ. In this reference, calculations of the orbital characters of the low energy bands showed that the valence band near **Γ** has primarily d_{yz} character, which translated to the measurement geometry in our experiment has the same parity as LV polarization. This causes enhancement of its photoemission signal in Figure 5.4**B** and suppression in Figure 5.4**A**. Similar arguments can be made for the conduction band, which has either d_{z^2} or mixed p_y and d_{xz} characters, and the rest of the valence band (also p_y and d_{xz}) being enhanced by LH polarization.

While circularly polarized excitation can differentially probe spin-polarized states[19489], our spin-agnostic measurement should not be sensitive to this effect. Nevertheless, plotting the difference shows the difference in photoemission with C_R and C_L light (Figure 5.4**C**) reveals an asymmetry of most of the bands across **Γ** with multiple inflection points where the asymmetry reverses. Strangely, only the outermost visible valence band below $E - E_F \sim 0.5$ eVis symmetric in $C_R - C_L$ across **Γ**. Qualitatively similar results have been reported from dichroic ARPES studies of graphene and hBN where momentum-modulated circular-dichroism of the photoemission was

observed in correlation with the bands' local Berry curvature[195]. As a difference in the Berry curvature of the electron pockets in ML WTe_2 has already been demonstrated experimentally[196], a similar effect may be at play here with the valence bands.

5.2.2 *Temperature dependent spectra*

Following these polarization dependent measurements, the sample temperature was incrementally stepped and $E - \boldsymbol{k}$ maps were taken at T = 60 K, 90 K, 120 K, and 150 K along over a small window in $\boldsymbol{k}$. LH polarization was used to maximize the signal-to-noise and to allow visualization of the conduction band feature. Figure 5.5**A** shows $E - k$ slices taken along **Γ**-**Y** at each temperature. From these data two primary effects of increasing temperature can be seen. The first is that the energy of the lower valence band feature, as tracked in EDCs through **Γ** (Figure 5.5**B**) shifts monotonically towards lower binding energy by ~40 meV over the full temperature range. A similar shift has been seen in bulk WTe_2 which was ascribed to Lifshitz transitions due to temperature regulation and surface modification[197]. It is unclear how applicable such effects would be in the monolayer limit. Private communications with other groups have indicated consistent shifting has been observed by them in monolayer WTe_2.

The other observable change with the temperature is with the conduction band feature, which visibly extends nearly 200 meV below the Fermi energy at 150 K, but only about 100 meV

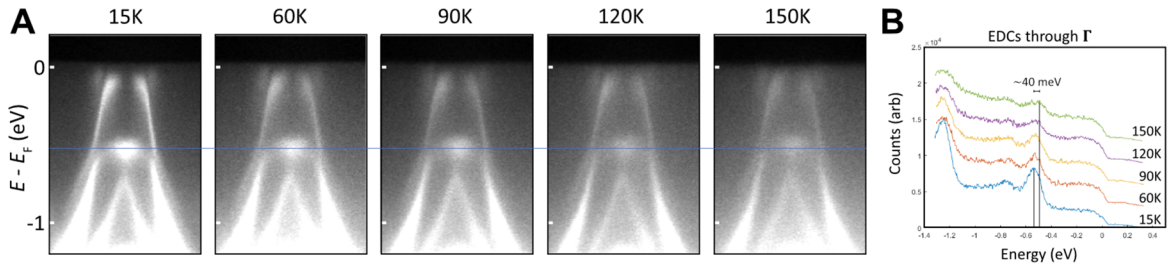

Figure 5.5. Temperature dependence of WTe_2 microARPES spectra. **A**, *E-k* slices along **Γ**-**Y** at various temperatures using LH. Dashed blue line marks the peak energy of the central valence band feature at 15K. **B**, EDCs through **Γ** at various temperatures from **A**.

below E_F at 60 K and 15 K. This difference cannot be ascribed to temperature alone, as the difference in Fermi smearing is $\sim 2.2 \times k_B \Delta T \sim 20\ meV$. Intriguingly, that the conduction band seems to continue to overlap the valence band even at the lowest temperatures is in stark contrast with the other ARPES measurements in the literature. It should be noted that in the 90 K, 60 K, and 15 K data, the conduction feature drops off approaching zero binding energy well before reaching the edge of the background (which is used to calibrate E_F). While this may be the signature of an exotic energy shifting of the apparent conduction band, perhaps due to electron-hole pairing into excitons which would cause a shift by ~ the exciton binding energy, it could also be due to an error with the electron analyzer according to the beamline scientists.

5.3 Measurements in Nano-ARPES

Following the measurements in microARPES, the sample was transferred over to nanoARPES where at the time of the measurement the sample stage was cooled via LN_2 with a stable base temperature of 180 K. When this temperature was equilibrated with the sample loaded, the detector was aligned to the **Γ-Y** axis of the sample as was done in microARPES. Then, large area $E - \boldsymbol{k}$ maps were taken. The spot size was ~3 μm, and LH 72 eV excitation was used. Figure 5.6 shows constant energy slices through this map, which extended into neighboring Brillouin zones which show similar features as the first zone. Two features are of note. Firstly, at several

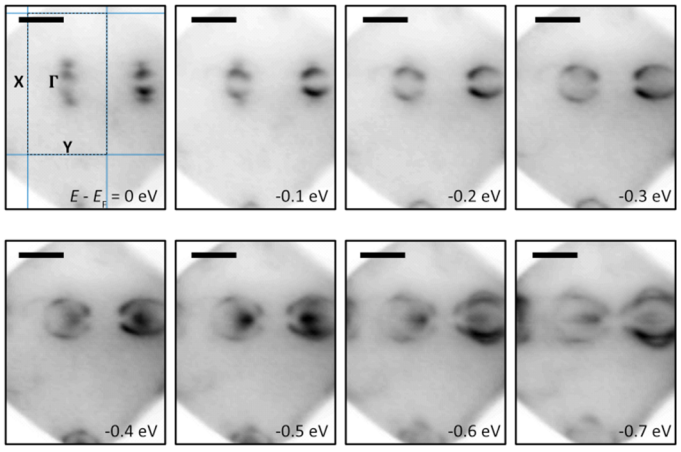

Figure 5.6. nanoARPES constant energy maps over multiple Brillouin zones of WTe_2 at 180 K. First Brillouin zone is outlined in dashed black in first map. Measurements used 72 eV LH-polarized excitation averaged over energy windows of 0.1 eV. Scale bars, 0.50 $Å^{-1}$.

ghostly replicas can be seen in between the zones, especially at $E - E_F = -0.4$ eV and -0.7 eV. These are reminiscent of the replica bands from Chapter 4. However, it is unclear how the drastically different crystal symmetries between WTe_2 and the other 2D flakes in this device can produce band folding. The second notable feature is that the nearby zone the map nearly fully captures shows higher intensity from the valence bands but less from the conduction bands. As we are interested in the conduction band, and to ease potential comparison to the measurements from microARPES, the remaining measurements were all also from in the first Brillouin zone.

5.3.1 *Temperature and gate voltage dependent spectra with LH polarization*

The first such measurements were *E* - *k* slices along **Γ**-**Y** taken at a series of gate voltages between -4 V and $+4$ V across the 14 nm thick hBN dielectric (Figure 5.7**A**). The voltage biasing was done with a Keithley sourcemeter, and the current compliance limit was set to a few nA. For yet unclear reasons, the Fermi edge of the background in these measurements was nonuniform in

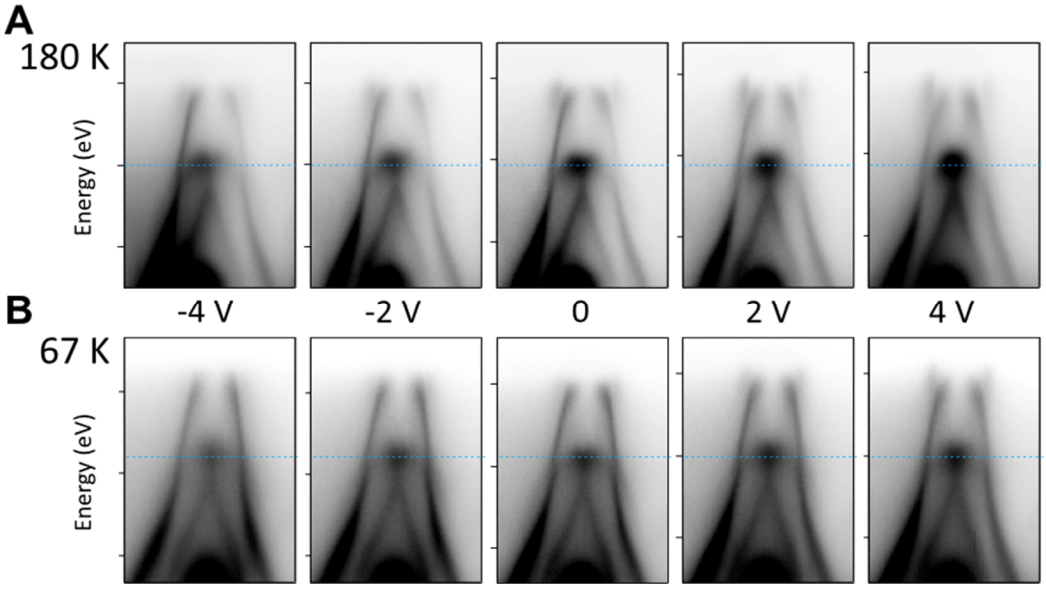

Figure 5.7. Gate and temperature dependence of WTe_2 nanoARPES spectra. **A**, *E*-*k* slices along **Γ**-**Y** at 180 K and V_G between -4V and $+4$ V using LH 72 eV excitation. **B**, similar slices taken at 67 K. All spectra have been vertically shifted to align the central valence band feature to the dashed blue line for ease of comparison. Energy scale tick marks are 0.5 eV apart.

momentum, possibly due to distortion from the electron lens. Consequently, the data have modulations in energy and are not aligned to E_F. The former problem is fortunately not significant in the vicinity of **Γ**. To sidestep the latter, the data can be shifted vertically as to align the fitted peak energies of the valence band feature at the centers of the slices. Thusly the data from different voltages can be directly compared despite possible relative energy scale shifts due to, e.g., changing surface potential due to the gate.

As the sample was swept from maximally p-doped at $V_G = -4$ V to maximally n-doped, the apparent E_F shifted to higher energy and more of the conduction band feature could be seen. Nevertheless, it remained visible and overlapped with what can be seen of the valence band over the entire voltage range. Though with the present spectral resolution this feature cannot be definitively ascribed to electrostatic population of the conduction band, it is strongly suggestive of the band structure being ungapped.

Remarkably, the full dispersions of the electron pockets were never fully resolvable even with the gate at $+4$ V. Instead, they appear as essentially straight lines pointed slightly outwards away from the valence band, resembling the 'inner' halves of the full bands. This behavior is similar with previously reported ARPES measurement of the conduction band at high (K-)doping using what was labeled "S-polarized" excitation[95], the analogue of which at MAESTRO is LV. However, this is surprising as these data were taken with LH excitation which enhanced the signal from the valence band 'wings' as is consistent with the model but for the same reason should be similarly enhancing the entire conduction band. This should not be the result of a rotation of the sample crystal axis relative to the excitation/surface normal mirror plane, as the orbital character of the 'missing' conduction band half is d_{z^2} which should be insensitive to rotation.

Some time after this beamtime, nanoARPES was upgraded with a new closed cycle cryostat and we took the chance to have this device remounted and measured below 100 K with gating. In between these beamtimes, the sample was sealed in CF flanges and stored inside of the glovebox at MAESTRO. Figure 5.7**B** shows the spectra taken at the system's base temperature at otherwise identical gating/excitation conditions as the previous measurements at 180 K. As was done with those data, the spectra here are also shifted to align the central valence band. Due to the system then being newly commissioned and not well calibrated, it was only later that the base temperature was characterized as 67 K.

Starting with the spectrum with the gate grounded, the signal from the conduction band has been dramatically reduced compared to the grounded 180 K measurement, with the difference in the energy extent of that feature shrinking by more than would be expected from the temperature difference alone. This is consistent with what was previously seen in microARPES. When the gate voltage was taken positive, the conduction band feature extended to higher energy while the valence band was fixed. As was at 180 K, not the entire electron pocket is being visualized but what can be seen energetically overlaps the valence band.

As the gate was instead taken to negative voltage, the valence bands shifted up in kinetic energy while the photoemission intensity from the electron pockets decreased. The band shifting effect was not seen at the higher temperature. It is suggestive of the band shifting one would expect when gating a gapped system as the work function is tuned by the gate voltage while the Fermi energy is inside of the gap. At -4 V, the photoemission intensity of the conduction band vanishes entirely. Since the valence band is known to be very flat near $\mathbf{\Gamma}$ with a high density of states at the band edge, the relatively low doping achievable with such a low gate voltage over 14 nm of hBN

(4 V/14 nm ~ 0.28 V/nm ≪ 0.5 V/nm, the typical breakdown field for hBN gates) is not expected to substantially move the Fermi energy into the valence band.

Therefore, that the electron pocket vanishes strongly indicates that the gap is positive in contrast to the higher temperature case. This stands in contrast with the positive gate result, and the discrepancy is too great to be ascribed to thermal smearing. While it cannot be proven from these data alone, this hints at a possible tuning of the band gap itself with doping. This would be consistent with the idea that the gap is opening due to the formation of excitons, as doping the system can reduce the exciton binding energy (see Figure 3.7) and ultimately dissolve the excitonic insulator state.

However, the author remains wary of drawing strong conclusions from these data as time constraints limited the ability to carefully align the slices to be exactly along **Γ-Y** and the strengths of the electron pocket signal at each gate voltage may not be comparable between each other. Similarly, as the 180 K and 67 K data were taken several months apart (during which time the sample was stored in only reasonably dry conditions), they may also not be simply compared. For example, the sample's rotational alignment to the excitation/surface normal mirror plane can change is not easily controlled due to the rotational symmetry of the sample puck. Changes in this may then affect the matrix elements and artificially change the relative intensities of the conduction band feature.

5.3.2 *Visualizing all low energy bands with circular polarization and gating*

The last data we will discuss here were taken at the last moments of our beamtime when it was realized that C_R and C_L together should access all parts of the bands more consistently than with linearly polarized excitation alone. Indeed this was the case, as can be seen in Figure 5.8**A** which shows spectra taken at 67 K with V_G pushed near the ~2 nA compliance limits at +6 V and

-5 V. These spectra have been shifted in energy to align their apparent local E_F by eye. While the intensity at the VBM was still greatly diminished relative to the rest of the band structure, it remained high enough to resolve and appears strongly in the second derivative.

The electron pockets evolved consistently with what was seen with LH excitation. In particular, the electron pocket remains seemingly half-visualized, and at the most negative gate voltage intensity from it is essentially completely gone even in the second derivative data. Finally, the shifting of the valence bands in energy (without the manual energy-scale shifting of the spectra) can be seen via EDCs through **Γ** (Figure 5.8**B**) from which a monotonic shift totaling ~75 meV over this voltage range can be seen for two different valence band features. This is surprisingly similar to the shift seen in other reports[95] using K-doping which likely reached at least twice the amount of induced carriers than achieved here with gating.

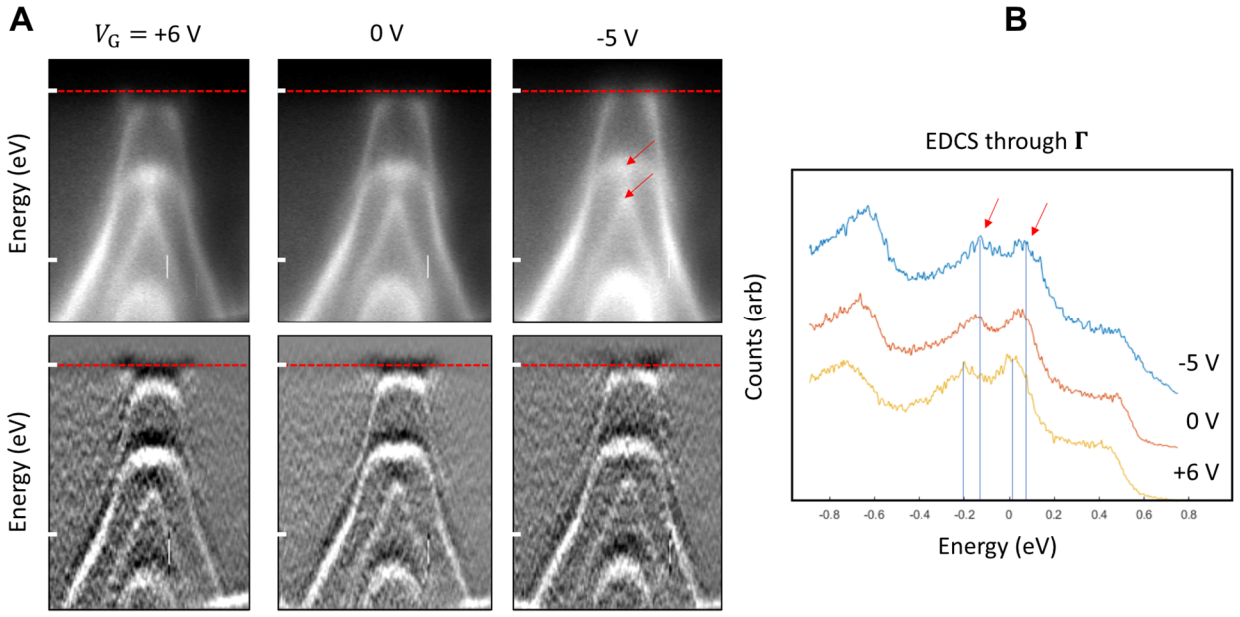

Figure 5.8. Gate dependence of circularly polarized spectra at 67 K. **A**, *E-k* slices along **Γ**-**Y** at 67 K at −5 V, 0 V, and +6 V with C_R + C_L excitation. Raw spectra are plotted above, second derivatives beneath. **B**, EDCs through **Γ** from **A**. Two prominent valence band features labeled by red arrows and their peak energies marked by blue lines.

5.4 Summary and Discussion

In this chapter, we discussed a substantial number of μ-ARPES studies of an air-sensitive monolayer, topologically nontrivial material with both electrostatic gating and temperature dependence. These results would not have been possible without the numerous advantages to measuring at MAESTRO, e.g., the integrated glovebox, tunable excitation energy and polarization, closed-cycle cooling, and high flux. Promising changes of the spectra with temperature were observed in measurements from both the microARPES and nanoARPES endstations. In particular, the photoemission from the conduction band could be modulated with decreasing temperature by a greater degree than would be expected by changing thermal broadening. Similarly, the Fermi energy was tunable with gate, and at high positive voltage it was shifted towards the conduction band by more than the highest plausible estimates of the band gap. At high negative voltage, the conduction band could still be visualized at high temperatures but as absent at 67 K. This is inconsistent with a trivial gap of ∼50 meV again as this is much larger than the expected broadening due to the Fermi-Dirac distribution.

It is however also inconsistent with the high positive gate behavior which had the conduction band overlapping the valence band at all temperatures. This may indicate a doping-dependent band structure, possibly due to the destruction of an exotic gapped phase such as the excitonic insulator state proposed in other works. A direct signature of such a phase is shifting of the spectral weight between the low energy valence and conduction bands. This stems from the fact that ARPES ultimately probes the photohole and excitons would comprise electrons from the conduction band and holes from the valence band[23]. This effect would vanish with increasing energy past the transition temperature and so a relative change of the spectra may make provide additional information.

The data presented here lack the resolution to resolve such spectral weight shifting, in part due to the yet unclear polarization dependence. We are not helped by the difficulty in comparing the gated spectra taken at nanoARPES at different temperatures, as they were taken at different times and therefore under different conditions. These problems may be addressed in the future with a fresh sample with which all gate- and temperature-dependent measurements can be done simultaneously. In the near term, nanoARPES has very recently demonstrated a new lower base temperature of 15 K, with which thermal broadening should be yet decreased and the conduction band edge made sharper. We learned that the combination of circular left and right excitation at MAESTRO allows convenient simultaneous observation of the electron and hole pockets, a capability that will certainly be leveraged with future beamtimes. Theoretical support will also be critical by providing, say, models of how the matrix elements should vary with the formation of an excitonic insulator state.

Chapter 6. OUTLOOK

Over the last decade the development and application of μ-ARPES to 2D materials has exploded. Not only have new beamlines been developed[198] and new focusing schemes demonstrated[25], but hopefully the works discussed here have shown how the 2D fabrication process and understanding of the spectra from 2D heterostructures have continued to evolve to leverage ever more of μ-ARPES's full power. In particular, it should be clear now that *in-operando* gating provides a uniquely potent tool for studying the local changes of the electronic structure in operating 2D heterostructures and devices. Here we only touched on a single shelf in the two-dimensional material library and have left much up to be discovered with continued study.

Though many (if not most) of the remaining isolated materials are likely less stable than the TMDs, our measurements with WTe_2 have demonstrated a device geometry affording both relative sample stability and ease of application to ARPES with an air-/water-/heat-sensitive material. Other materials of similar sensitivity include some of the 2D magnets, such as Fe_5GeTe_2[199] and $NiPS_3$[200], studies of which will benefit from long term development of spin-resolved μ-ARPES[11]. In the case of $NiPS_3$, for example, the photoluminescence spectra have a strong dependence on thickness due to an expected shift in the band extrema positions and can have doping dependence – perfect matters for gated μ-ARPES to probe.

Beyond studying individual materials, μ-ARPES is also an effective tool for studying the bands at the surface of heterostructures and particularly heterobilayers/heterotrilayers. The most topical facet of which today is involves twisting at "magic angles" wherein the folded and hybridized bands form flat bands. The formation of such bands has already been reported from ARPES, but so far no effects of gating on the bands have been claimed. Instead claims of the isolated nature of the flattened bands from the dispersive higher conduction bands were supported

by normalization of the spectra by the Fermi function, thereby revealing a weak, distanced center of photoemission at positive binding energy. Clearly, however, electrostatic doping would have been a more direct means to reach those states. *In-situ* electric field control may be especially important in magic systems where gate-induced polarization of the electrons in the heterostructure is important, such as in magic-angle double-bilayer graphene[201].

Finally, we should address the future of μ-ARPES and nano-ARPES itself. Following its successful debut in nanoARPES at MAESTRO where a capillary optic provided a compelling compromise between spatial resolution and flux[25], there are short term plans for adoption of this technology at other μ-ARPES facilities such as I05 at the Diamond synchrotron to supplement Fresnel zone plate-based focusing which in the author's experience often offers too little flux to study materials/states with relatively low cross-section. In the long term, it should be noted that all of the synchrotrons hosting μ-ARPES facilities are planning upgrades to become "fourth generation" sources[202] with so-called diffraction-limited performance. This would dramatically reduce the dimension of the source and so enhance the brightness. For established μ-ARPES facilities, this will provide further ease of focusing the excitation beam and may rebalance the compromise from zone plates. Accessing nm-scale beam spots will have knockdown improvements of the energy and angular resolution. Nonetheless, the ultimate benefits of this upgrade will be limited as ARPES is intrinsically limited by space-charge effects[11], where the cloud of photoemitted electrons interacts with itself which must scale with the photoemission rate. Beyond synchrotron-based μ-ARPES are developments of laser-based facilities where the draw of studying 2D materials has justified improvements in the beam spot size[96] and collection schemes[23]. Further refinements in this field will enable additional techniques such as time-resolved ARPES to probe excited states.

BIBLIOGRAPHY

1. Hüfner, S., Schmidt, S. & Reinert, F. Photoelectron spectroscopy - An overview. in *Nuclear Instruments and Methods in Physics Research, Section A: Accelerators, Spectrometers, Detectors and Associated Equipment* vol. 547 8–23 (2005).
2. Fadley, C. S. Atomic-level characterization of materials with core- and valence-level photoemission: Basic phenomena and future directions. *Surface and Interface Analysis* vol. 40 1579–1605 (2008).
3. Walsh, A., Sokol, A. A., Buckeridge, J., Scanlon, D. O. & Catlow, C. R. A. Oxidation states and ionicity. *Nat. Mater.* **17**, 958–964 (2018).
4. Damascelli, A. *Probing the Low-Energy Electronic Structure of Complex Systems by ARPES*. (2003).
5. Hsieh, D. *et al.* A topological Dirac insulator in a quantum spin Hall phase. *Nature* **452**, 970–974 (2008).
6. Hasan, M. Z. & Kane, C. L. Colloquium: Topological insulators. *Rev. Mod. Phys.* **82**, 3045–3067 (2010).
7. Damascelli, A. Probing the Electronic Structure of Complex Systems by ARPES. *Phys. Scr.* **T109**, 61 (2004).
8. Aebi, P., Osterwalder, J., Fasel, R., Naumović, D. & Schlapbach, L. Fermi surface mapping with photoelectrons at UV energies. *Surf. Sci.* **307–309**, 917–921 (1994).
9. Hansson, G. V., Uhrberg, R. I. G. & Flodstrom, S. A. Electronic structure of the Si(111) 7x7 surface studied by angle-resolved photoemission spectroscopy.*Journal of vacuum science & technology* vol. 16 1287–1289 (1979).
10. DA30-L - Scienta Omicron. https://scientaomicron.com/en/Components/Electron-Analysers/DA30-L.
11. Rotenberg, E. & Bostwick, A. microARPES and nanoARPES at diffraction-limited light sources: opportunities and performance gains. *J. Synchrotron Radiat.* **21**, 1048–1056 (2014).
12. Caroli, C., Lederer-Rozenblatt, D., Roulet, B. & Saint-James, D. Inelastic effects in photoemission: Microscopic formulation and qualitative discussion. *Phys. Rev. B* **8**, 4552–4569 (1973).
13. Feibelman, P. J. & Eastman, D. E. Photoemission spectroscopy-Correspondence between quantum theory and experimental phenomenology. *Phys. Rev. B* **10**, 4932–4947 (1974).
14. Potthoff, M., Lachnitt, J., Nolting, W. & Braun, J. One-Step Model of Photoemission for Nonlocal Potentials. *Phys. status solidi* **203**, 441–457 (1997).
15. Berglund, C. N. & Spicer, W. E. Photoemission studies of copper and silver: Theory. *Phys. Rev.* **136**, A1030 (1964).
16. Seah, M. P. & Dench, W. A. Quantitative electron spectroscopy of surfaces: A standard data base for electron inelastic mean free paths in solids. *Surf. Interface Anal.* **1**, 2–11 (1979).
17. 4.2: Why is UHV required for surface studies ? - Chemistry LibreTexts. https://chem.libretexts.org/Bookshelves/Physical_and_Theoretical_Chemistry_Textbook_Maps/Book%3A_Surface_Science_(Nix)/04%3A_UHV_and_Effects_of_Gas_Pressure/4.02%3A_Why_is_UHV_required_for_surface_studies_%3F.
18. Ovcharenko, R., Dedkov, Y. & Voloshina, E. Adsorption of NO2 on WSe2: DFT and photoelectron spectroscopy studies. *J. Phys. Condens. Matter* **28**, 364003 (2016).

19. Mucha-Kruczyński, M. *et al.* Characterization of graphene through anisotropy of constant-energy maps in angle-resolved photoemission. **77**, 195403 (2008).
20. Kaminski, A. & Fretwell, H. M. On the extraction of the self-energy from angle-resolved photoemission spectroscopy. *New J. Phys.* **7**, 98 (2005).
21. Kiss, T. *et al.* Photoemission spectroscopic evidence of gap anisotropy in an f-electron superconductor. *Phys. Rev. Lett.* **94**, 057001 (2005).
22. Koralek, J. D. *et al.* Laser based angle-resolved photoemission, the sudden approximation, and quasiparticle-like spectral peaks in Bi2Sr2CaCu2O8+Î. *Phys. Rev. Lett.* **96**, 017005 (2006).
23. Madéo, J. *et al.* Directly visualizing the momentum-forbidden dark excitons and their dynamics in atomically thin semiconductors. *Science (80-.).* **370**, 1199–1204 (2020).
24. Dudin, P. *et al.* Angle-resolved photoemission spectroscopy and imaging with a submicrometre probe at the SPECTROMICROSCOPY-3.2L beamline of Elettra. *J. Synchrotron Radiat.* **17**, 445–450 (2010).
25. Koch, R. J. *et al.* Nano focusing of soft X-rays by a new capillary mirror optic. *Synchrotron Radiat. News* **31**, 50–52 (2018).
26. Raeker, T. Physical Adsorption: Forces and Phenomena (Bruch, L.W.; Cole, Milton W.; Zaremba, Eugene). *J. Chem. Educ.* **75**, 1557 (1998).
27. Dash 1923-, J. G. (Jay G. *Films on solid surfaces : the physics and chemistry of physical adsorption / J. G. Dash*. (Academic Press, 1975).
28. Peierls, R. E. Bemerkungen uber umwandlungstemperaturen. *Helv. Phys. Acta.* **7**, 81–83 (1934).
29. Mermin, N. D. Crystalline Order in Two Dimensions. *Phys. Rev.* **176**, 250–254 (1968).
30. Mermin, N. D. & Wagner, H. Absence of Ferromagnetism or Antiferromagnetism in One- or Two-Dimensional Isotropic Heisenberg Models. *Phys. Rev. Lett.* **17**, 1133–1136 (1966).
31. Nelson, D.R. & Peliti, L. Fluctuations in membranes with crystalline and hexatic order. *J. Phys. Fr.* **48**, 1085–1092 (1987).
32. Le Doussal, P. & Radzihovsky, L. Self-consistent theory of polymerized membranes. *Phys. Rev. Lett.* **69**, 1209–1212 (1992).
33. Oshima, C. & Nagashima, A. Ultra-thin epitaxial films of graphite and hexagonal boron nitride on solid surfaces. *J. Phys. Condens. Matter* **9**, 1–20 (1997).
34. Forbeaux, I., Themlin, J.-M. & Debever, J.-M. Heteroepitaxial graphite on $6H\ensuremath{-}\mathrm{SiC}(0001):$ Interface formation through conduction-band electronic structure. *Phys. Rev. B* **58**, 16396–16406 (1998).
35. Novoselov, K. S. *et al.* Electric Field Effect in Atomically Thin Carbon Films. *Science (80-.).* **306**, 666–669 (2004).
36. Khan, K. *et al.* Recent developments in emerging two-dimensional materials and their applications. *J. Mater. Chem. C* **8**, 387–440 (2020).
37. Wallace, P. R. The band theory of graphite. *Phys. Rev.* **71**, 622–634 (1947).
38. Novoselov, K. S. *et al.* Two-dimensional gas of massless Dirac fermions in graphene. *Nature* **438**, 197–200 (2005).
39. Bostwick, A., Ohta, T., Seyller, T., Horn, K. & Rotenberg, E. Quasiparticle dynamics in graphene. *Nat. Phys.* **3**, 36–40 (2007).
40. Efetov, D. K. *et al.* Specular interband Andreev reflections at van der Waals interfaces between graphene and NbSe2. *Nat. Phys.* **12**, 328–332 (2016).

41. Cao, Y. *et al.* Unconventional superconductivity in magic-angle graphene superlattices. *Nature* **556**, 43–50 (2018).
42. Bistritzer, R. & MacDonald, A. H. Moiré bands in twisted double-layer graphene. *Proc. Natl. Acad. Sci. U. S. A.* **108**, 12233–12237 (2011).
43. Tomarken, S. L. *et al.* Correlated insulator behaviour at half-filling in magic-angle graphene superlattices. *Nature* **556**, 80–84 (2018).
44. Cao, Y. *et al.* Magic-angle graphene superlattices: a new platform for unconventional superconductivity. *Nature* **556**, 43–50 (2018).
45. Zomer, P. J., Guimarães, M. H. D., Brant, J. C., Tombros, N. & Van Wees, B. J. Fast pick up technique for high quality heterostructures of bilayer graphene and hexagonal boron nitride. *Appl. Phys. Lett.* **105**, 013101 (2014).
46. Britnell, L. *et al.* Electron tunneling through ultrathin boron nitride crystalline barriers. *Nano Lett.* **12**, 1707–1710 (2012).
47. Veyrat, L. *et al. Helical quantum Hall phase in graphene on SrTiO 3*. (2019).
48. Grosso, G. *et al.* Tunable and high-purity room temperature single-photon emission from atomic defects in hexagonal boron nitride. *Nat. Commun.* **8**, 1–8 (2017).
49. Wang, L. *et al.* New Generation of Moiré Superlattices in Doubly Aligned hBN/Graphene/hBN Heterostructures. *Nano Lett.* **19**, 2371–2376 (2019).
50. Woods, C. R. *et al.* Charge-polarized interfacial superlattices in marginally twisted hexagonal boron nitride. *Nat. Commun.* **12**, 1–7 (2021).
51. Chhowalla, M. *et al.* The chemistry of two-dimensional layered transition metal dichalcogenide nanosheets. *Nature Chemistry* vol. 5 263–275 (2013).
52. Manzeli, S., Ovchinnikov, D., Pasquier, D., Yazyev, O. V. & Kis, A. 2D transition metal dichalcogenides. *Nature Reviews Materials* vol. 2 17033 (2017).
53. Fei, Z. *et al.* Ferroelectric switching of a two-dimensional metal. *Nature* **560**, 336–339 (2018).
54. Lu, J. *et al.* Full superconducting dome of strong Ising protection in gated monolayer WS2. *Proc. Natl. Acad. Sci. U. S. A.* **115**, 3551–3556 (2018).
55. Shi, W. *et al.* Superconductivity Series in Transition Metal Dichalcogenides by Ionic Gating. *Sci. Rep.* **5**, 12534 (2015).
56. Yoffe, A. D. Layer Compounds. *Annu. Rev. Mater. Sci.* **3**, 147–170 (1973).
57. Mattheiss, L. F. Band structures of transition-metal-dichalcogenide layer compounds. *Phys. Rev. B* **8**, 3719–3740 (1973).
58. Coehoorn, R. *et al.* Electronic structure of MoSe2, MoS2, and WSe2. I. Band-structure calculations and photoelectron spectroscopy. *Phys. Rev. B* **35**, 6195–6202 (1987).
59. Coehoorn, R., Haas, C. & De Groot, R. A. Electronic structure of MoSe2, MoS2, and WSe2. II. The nature of the optical band gaps. *Phys. Rev. B* **35**, 6203–6206 (1987).
60. Kuc, A., Zibouche, N. & Heine, T. Influence of quantum confinement on the electronic structure of the transition metal sulfide TS2. *Phys. Rev. B - Condens. Matter Mater. Phys.* **83**, 245213 (2011).
61. Mak, K. F., Lee, C., Hone, J., Shan, J. & Heinz, T. F. Atomically thin MoS2: A new direct-gap semiconductor. *Phys. Rev. Lett.* **105**, 136805 (2010).
62. Xiao, D., Liu, G. Bin, Feng, W., Xu, X. & Yao, W. Coupled spin and valley physics in monolayers of MoS 2 and other group-VI dichalcogenides. *Phys. Rev. Lett.* **108**, 196802 (2012).
63. Zheng, Z. *et al.* Unconventional ferroelectricity in moiré heterostructures. *Nature* **588**, 71–

76 (2020).
64. Seyler, K. L. *et al.* Signatures of moiré-trapped valley excitons in MoSe2/WSe2 heterobilayers. *Nature* **567**, 66–70 (2019).
65. Mamy, R., Boufelja, A. & Carricaburu, B. Angle Resolved Photoemission and Electronic Band Structure of MoS2. *Phys. status solidi* **141**, 467–473 (1987).
66. Wilson, J. A. & Yoffe, A. D. The transition metal dichalcogenides discussion and interpretation of the observed optical, electrical and structural properties. *Adv. Phys.* **18**, 193–335 (1969).
67. Zhu, Z. Y., Cheng, Y. C. & Schwingenschlögl, U. Giant spin-orbit-induced spin splitting in two-dimensional transition-metal dichalcogenide semiconductors. *Phys. Rev. B - Condens. Matter Mater. Phys.* **84**, 153402 (2011).
68. Ramasubramaniam, A. Large excitonic effects in monolayers of molybdenum and tungsten dichalcogenides. *Phys. Rev. B - Condens. Matter Mater. Phys.* **86**, 115409 (2012).
69. Liu, G.-B., Xiao, D., Yao, Y., Xu, X. & Yao, W. Electronic structures and theoretical modelling of two-dimensional group-VIB transition metal dichalcogenides. *Chem. Soc. Rev.* **44**, 2643–2663 (2015).
70. Qiu, D. Y., Da Jornada, F. H. & Louie, S. G. Optical spectrum of MoS2: Many-body effects and diversity of exciton states. *Phys. Rev. Lett.* **111**, 216805 (2013).
71. Shi, H., Pan, H., Zhang, Y. W. & Yakobson, B. I. Quasiparticle band structures and optical properties of strained monolayer MoS2 and WS2. *Phys. Rev. B - Condens. Matter Mater. Phys.* **87**, 155304 (2013).
72. Liang, Y., Huang, S., Soklaski, R. & Yang, L. Quasiparticle band-edge energy and band offsets of monolayer of molybdenum and tungsten chalcogenides. *Appl. Phys. Lett.* **103**, 042106 (2013).
73. Huang, Y. L. *et al.* Bandgap tunability at single-layer molybdenum disulphide grain boundaries. *Nat. Commun.* **6**, 1–8 (2015).
74. Ugeda, M. M. *et al.* Giant bandgap renormalization and excitonic effects in a monolayer transition metal dichalcogenide semiconductor. *Nat. Mater.* **13**, 1091–1095 (2014).
75. Zhang, C., Johnson, A., Hsu, C. L., Li, L. J. & Shih, C. K. Direct imaging of band profile in single layer MoS2 on graphite: Quasiparticle energy gap, metallic edge states, and edge band bending. *Nano Lett.* **14**, 2443–2447 (2014).
76. Zhang, C. *et al.* Probing Critical Point Energies of Transition Metal Dichalcogenides: Surprising Indirect Gap of Single Layer WSe 2. *Nano Lett.* **15**, 6494–6500 (2015).
77. Feenstra, R. M. A prospective: Quantitative scanning tunneling spectroscopy of semiconductor surfaces. *Surface Science* vol. 603 2841–2844 (2009).
78. Eknapakul, T. *et al.* Electronic structure of a quasi-freestanding MoS2 monolayer. *Nano Lett.* **14**, 1312–1316 (2014).
79. Zhang, Y. *et al.* Direct observation of the transition from indirect to direct bandgap in atomically thin epitaxial MoSe2. *Nat. Nanotechnol.* **9**, 111–115 (2013).
80. Coy Diaz, H. *et al.* Direct observation of interlayer hybridization and dirac relativistic carriers in Graphene/MoS2 van der waals heterostructures. *Nano Lett.* **15**, 1135–1140 (2015).
81. Jin, W. *et al.* Direct measurement of the thickness-dependent electronic band structure of MoS2 using angle-resolved photoemission spectroscopy. *Phys. Rev. Lett.* **111**, 1–5 (2013).
82. Yeh, P. C. *et al.* Layer-dependent electronic structure of an atomically heavy two-

dimensional dichalcogenide. *Phys. Rev. B - Condens. Matter Mater. Phys.* **91**, 041407 (2015).
83. Riley, J. M. *et al.* Direct observation of spin-polarized bulk bands in an inversion-symmetric semiconductor. *Nat. Phys.* **10**, 835–839 (2014).
84. Rivera, P. *et al.* Valley-polarized exciton dynamics in a 2D semiconductor heterostructure. *Science (80-.).* **351**, 688–691 (2016).
85. Schaibley, J. R. *et al.* Directional interlayer spin-valley transfer in two-dimensional heterostructures. *Nat. Commun.* **7**, 1–6 (2016).
86. Qian, X., Liu, J., Fu, L. & Li, J. Quantum spin hall effect in two - Dimensional transition metal dichalcogenides. *Science (80-.).* **346**, 1344–1347 (2014).
87. Eda, G. *et al.* Coherent atomic and electronic heterostructures of single-layer MoS 2. *ACS Nano* **6**, 7311–7317 (2012).
88. Ali, M. N. *et al.* Large, non-saturating magnetoresistance in WTe2. *Nature* **514**, 205–208 (2014).
89. Ma, Q. *et al.* Observation of the nonlinear Hall effect under time-reversal-symmetric conditions. *Nature* **565**, 337–342 (2019).
90. Wang, H. & Qian, X. Ferroelectric nonlinear anomalous Hall effect in few-layer WTe2. *npj Comput. Mater.* **5**, 1–8 (2019).
91. Fei, Z. *et al.* Edge conduction in monolayer WTe 2. *Nat. Phys.* **13**, 677–682 (2017).
92. Wu, S. *et al.* Observation of the quantum spin Hall effect up to 100 kelvin in a monolayer crystal. *Science (80-.).* **359**, 76–79 (2018).
93. Fu, L. & Kane, C. L. Superconducting proximity effect and majorana fermions at the surface of a topological insulator. *Phys. Rev. Lett.* **100**, 096407 (2008).
94. Choe, D. H., Sung, H. J. & Chang, K. J. Understanding topological phase transition in monolayer transition metal dichalcogenides. *Phys. Rev. B* **93**, 125109 (2016).
95. Tang, S. *et al.* Quantum spin Hall state in monolayer 1T'-WTe2. *Nat. Phys.* **13**, 683–687 (2017).
96. Cucchi, I. *et al.* Microfocus Laser–Angle-Resolved Photoemission on Encapsulated Mono-, Bi-, and Few-Layer 1T′-WTe 2. *Nano Lett.* **19**, 554–560 (2019).
97. Sajadi, E. *et al.* Gate-induced superconductivity in a monolayer topological insulator. *Science (80-.).* **362**, 922–925 (2018).
98. Jia, Y. *et al.* Evidence for a Monolayer Excitonic Insulator. *arXiv* (2020).
99. Rivera, P. Interlayer Valley Excitons in Two-Dimensional Semiconductor Heterostructures. *Dr. thesis* (2018).
100. Gorbachev, R. V. *et al.* Hunting for Monolayer Boron Nitride: Optical and Raman Signatures. *Small* **7**, 465–468 (2011).
101. Huang, Y. *et al.* Reliable Exfoliation of Large-Area High-Quality Flakes of Graphene and Other Two-Dimensional Materials. *ACS Nano* **9**, 10612–10620 (2015).
102. Ovchinnikov, D. *et al.* Intertwined Topological and Magnetic Orders in Atomically Thin Chern Insulator $MnBi_2Te_4$. *Nano Lett.* acs.nanolett.0c05117 (2021) doi:10.1021/acs.nanolett.0c05117.
103. Wilson, N. R. *et al.* Determination of band offsets, hybridization, and exciton binding in 2D semiconductor heterostructures. *Sci. Adv.* **3**, e1601832 (2017).
104. Desai, S. B. *et al.* Gold-Mediated Exfoliation of Ultralarge Optoelectronically-Perfect Monolayers. *Adv. Mater.* **28**, 4053–4058 (2016).
105. Eichfeld, S. M. *et al.* Highly scalable, atomically thin WSe2grown via metal-organic

chemical vapor deposition. *ACS Nano* **9**, 2080–2087 (2015).
106. Li, X. *et al.* Large-area synthesis of high-quality and uniform graphene films on copper foils. *Science (80-.).* **324**, 1312 (2009).
107. Wang, L. *et al.* Epitaxial growth of a 100-square-centimetre single-crystal hexagonal boron nitride monolayer on copper. *Nature* **570**, 91–95 (2019).
108. Clark, G. *et al.* Vapor-transport growth of high optical quality WSe2 monolayers. *APL Mater.* **2**, 101101 (2014).
109. Huang, C. *et al.* Lateral heterojunctions within monolayer MoSe2–WSe2 semiconductors. *Nat. Mater.* **13**, 1096–1101 (2014).
110. Phase Imaging. https://parksystems.com/park-spm-modes/91-standard-imaging-mode/221-phase-imaging-phase-detection-microscopy-pdm.
111. Ross, J. S. *et al.* Electrical control of neutral and charged excitons in a monolayer semiconductor. *Nat. Commun.* **4**, 1474 (2013).
112. Malard, L. M., Alencar, T. V., Barboza, A. P. M., Mak, K. F. & De Paula, A. M. Observation of intense second harmonic generation from MoS2 atomic crystals. *Phys. Rev. B - Condens. Matter Mater. Phys.* **87**, 201401 (2013).
113. Seyler, K. L. Probing valley and magnetic photoexcitations in 2D crystals and their heterostructures. (2018).
114. Lepetit, L., Chériaux, G. & Joffre, M. Linear techniques of phase measurement by femtosecond spectral interferometry for applications in spectroscopy. *J. Opt. Soc. Am. B* **12**, 2467 (1995).
115. Veenstra, K., Petukhov, A., de Boer, A. & Rasing, T. Phase-sensitive detection technique for surface nonlinear optics. *Phys. Rev. B - Condens. Matter Mater. Phys.* **58**, R16020–R16023 (1998).
116. Wilson, P. T., Jiang, Y., Aktsipetrov, O. A., Mishina, E. D. & Downer, M. C. Frequency-domain interferometric second-harmonic spectroscopy. *Opt. Lett.* **24**, 496 (1999).
117. Son, S. *et al.* Strongly adhesive dry transfer technique for van der Waals heterostructure. *2D Mater.* **7**, 041005 (2020).
118. Lisi, S. *et al.* Observation of flat bands in twisted bilayer graphene. *Nature Physics* 1–5 (2020) doi:10.1038/s41567-020-01041-x.
119. McGilly, L. J. *et al.* Visualization of moiré superlattices. *Nat. Nanotechnol.* **15**, 580–584 (2020).
120. Kim, K. *et al.* Van der Waals Heterostructures with High Accuracy Rotational Alignment. *Nano Lett.* **16**, 1989–1995 (2016).
121. Li, H. *et al.* Electrode-Free Anodic Oxidation Nanolithography of Low-Dimensional Materials. *Nano Lett.* **18**, 8011–8015 (2018).
122. Harnagea, C., Alexe,) M, Hesse, D. & Pignolet, A. Contact resonances in voltage-modulated force microscopy. (2003) doi:10.1063/1.1592307.
123. Yankowitz, M. *et al.* Emergence of superlattice Dirac points in graphene on hexagonal boron nitride. *Nat. Phys.* **8**, 382–386 (2012).
124. Morell, E. S., Correa, J. D., Vargas, P., Pacheco, M. & Barticevic, Z. Flat Bands in Slightly Twisted Bilayer Graphene. 1–6 (2010) doi:10.1103/PhysRevB.82.121407.
125. Britnell, L. *et al.* Strong light-matter interactions in heterostructures of atomically thin films. *Science (80-.).* **340**, 1311–1314 (2013).
126. Cheng, R. *et al.* Electroluminescence and photocurrent generation from atomically sharp WSe2/MoS2 heterojunction p-n diodes. *Nano Lett.* **14**, 5590–5597 (2014).

127. Furchi, M. M., Pospischil, A., Libisch, F., Burgdörfer, J. & Mueller, T. Photovoltaic effect in an electrically tunable Van der Waals heterojunction. *Nano Lett.* **14**, 4785–4791 (2014).
128. Lee, C.-H. *et al.* Atomically thin p–n junctions with van der Waals heterointerfaces. *Nat. Nanotechnol.* **9**, 676–681 (2014).
129. Withers, F. *et al.* Light-emitting diodes by band-structure engineering in van der Waals heterostructures. *Nat. Mater.* **14**, 301–306 (2015).
130. Hong, X. *et al.* Ultrafast charge transfer in atomically thin MoS2/WS2 heterostructures. *Nat. Nanotechnol.* **9**, 682–686 (2014).
131. Rivera, P. *et al.* Observation of long-lived interlayer excitons in monolayer MoSe2-WSe2 heterostructures. *Nat. Commun.* **6**, 6242 (2015).
132. Yu, H., Wang, Y., Tong, Q., Xu, X. & Yao, W. Anomalous Light Cones and Valley Optical Selection Rules of Interlayer Excitons in Twisted Heterobilayers. *Phys. Rev. Lett.* **115**, 187002 (2015).
133. Huang, C. *et al.* Lateral heterojunctions within monolayer MoSe2-WSe2 semiconductors. *Nat. Mater.* **13**, 1096–1101 (2014).
134. Ohta, T. Controlling the Electronic Structure of Bilayer Graphene. *Science (80-.).* **313**, 951–954 (2006).
135. Kim, K. S. *et al.* Coexisting massive and massless Dirac fermions in symmetry-broken bilayer graphene. *Nat. Mater.* **12**, 887–892 (2013).
136. Latzke, D. W. *et al.* Electronic structure, spin-orbit coupling, and interlayer interaction in bulk MoS2 and WS2. *Phys. Rev. B - Condens. Matter Mater. Phys.* **91**, 235202 (2015).
137. Yuan, H. *et al.* Evolution of the Valley Position in Bulk Transition-Metal Chalcogenides and Their Monolayer Limit. *Nano Lett.* **16**, 4738–4745 (2016).
138. Wilson, N. R. *et al.* Band parameters and hybridization in 2D semiconductor heterostructures from photoemission spectroscopy. (2016) doi:10.1126/sciadv.1601832.
139. Tanabe, I. *et al.* Band structure characterization of WS2 grown by chemical vapor deposition. *Appl. Phys. Lett.* **108**, 252103 (2016).
140. Kretinin, A. V. *et al.* Electronic properties of graphene encapsulated with different two-dimensional atomic crystals. *Nano Lett.* **14**, 3270–3276 (2014).
141. Kormányos, A. *et al.* k · p theory for two-dimensional transition metal dichalcogenide semiconductors. *2D Mater.* **2**, 022001 (2015).
142. Komsa, H.-P. & Krasheninnikov, A. V. Electronic structures and optical properties of realistic transition metal dichalcogenide heterostructures from first principles. *Phys. Rev. B* **88**, 085318 (2013).
143. Kang, J., Tongay, S., Zhou, J., Li, J. & Wu, J. Band offsets and heterostructures of two-dimensional semiconductors. *Appl. Phys. Lett.* **102**, 012111 (2013).
144. Kumar, N. *et al.* Second harmonic microscopy of monolayer MoS2. *Phys. Rev. B - Condens. Matter Mater. Phys.* **87**, 161403 (2013).
145. Li, Y. *et al.* Probing symmetry properties of few-layer MoS2 and h-BN by optical second-harmonic generation. *Nano Lett.* **13**, 3329–3333 (2013).
146. Woods, C. R. *et al.* Commensurate–incommensurate transition in graphene on hexagonal boron nitride. *Nat. Phys.* **10**, 451–456 (2014).
147. Constantinescu, G. C. & Hine, N. D. M. Energy landscape and band-structure tuning in realistic MoS_2 heterostructures. *Phys. Rev. B* **91**, 195416 (2015).
148. Chiu, M. *et al.* Determination of band alignment in the single-layer MoS2/WSe2 heterojunction. *Nat. Commun.* **6**, 7666 (2015).

149. He, K. *et al.* Tightly Bound Excitons in Monolayer WSe2. *Phys. Rev. Lett.* **113**, 026803 (2014).
150. Chernikov, A. *et al.* Exciton binding energy and nonhydrogenic Rydberg series in monolayer WS2. *Phys. Rev. Lett.* **113**, 076802 (2014).
151. Wang, G. *et al.* Giant Enhancement of the Optical Second-Harmonic Emission of WSe2 Monolayers by Laser Excitation at Exciton Resonances. *Phys. Rev. Lett.* **114**, 097403 (2015).
152. Klots, A. R. *et al.* Probing excitonic states in suspended two-dimensional semiconductors by photocurrent spectroscopy. *Sci. Rep.* **4**, 6608 (2014).
153. Ye, Z. *et al.* Probing excitonic dark states in single-layer tungsten disulphide. *Nature* **513**, 214–218 (2014).
154. Zhu, B., Chen, X. & Cui, X. Exciton Binding Energy of Monolayer WS2. *Sci. Rep.* **5**, 9218 (2015).
155. Ulstrup, S. *et al. Spin and Valley Control of Free Carriers in Single-Layer WS 2*. (2016).
156. Nguyen, P. V. *et al.* Visualizing electrostatic gating effects in two-dimensional heterostructures. *Nature* **572**, 220–223 (2019).
157. Chen, G. *et al.* Evidence of a gate-tunable Mott insulator in a trilayer graphene moiré superlattice. *Nat. Phys.* **15**, 237–241 (2019).
158. Nguyen, P. V. *et al.* Visualizing electrostatic gating effects in two-dimensional heterostructures. (2019).
159. Yu, Y.-J. *et al.* Tuning the Graphene Work Function by Electric Field Effect. *Nano Lett.* **9**, 3430–3434 (2009).
160. Kormányos, A. *et al.* k·p theory for two-dimensional transition metal dichalcogenide semiconductors. *2D Mater.* **2**, 022001 (2015).
161. Late, D. J., Liu, B., Ramakrishna Matte, H. S. S., Dravid, V. P. & Rao, C. N. R. Hysteresis in Single-Layer MoS 2 Field Effect Transistors. (2012) doi:10.1021/nn301572c.
162. Fang, H. *et al.* High-Performance Single Layered WSe 2 p-FETs with Chemically Doped Contacts. *Nano Lett.* **12**, 3788–3792 (2012).
163. Huang, J.-K. *et al.* Large-Area Synthesis of Highly Crystalline WSe 2 Monolayers and Device Applications. *ACS Nano* **8**, 923–930 (2014).
164. Li, Y. *et al.* Measurement of the optical dielectric function of monolayer transition-metal dichalcogenides: MoS 2 , Mo S e 2 , WS 2 , and WS e 2. *Phys. Rev. B* **90**, 205422 (2014).
165. Kim, K. *et al.* Band Alignment in WSe $_2$ –Graphene Heterostructures. *ACS Nano* **9**, 4527–4532 (2015).
166. Wu, F., Lovorn, T. & Macdonald, A. H. Topological Exciton Bands in Moiré Heterojunctions. *Phys. Rev. Lett.* **118**, 1–6 (2017).
167. Tran, K. *et al.* Evidence for moiré excitons in van der Waals heterostructures. *Nature* **567**, 71–75 (2019).
168. That's Amore - Wikipedia. https://en.wikipedia.org/wiki/That%27s_Amore.
169. Amorim, B. General theoretical description of angle-resolved photoemission spectroscopy of van der Waals structures. *Phys. Rev. B* **97**, 1–15 (2018).
170. Ruiz-Tijerina, D. A. & Fal'ko, V. I. Interlayer hybridization and moiré superlattice minibands for electrons and excitons in heterobilayers of transition-metal dichalcogenides. *Phys. Rev. B* **99**, 125424 (2019).
171. Starodub, E. *et al.* In-plane orientation effects on the electronic structure, stability, and Raman scattering of monolayer graphene on Ir(111). *Phys. Rev. B - Condens. Matter*

Mater. Phys. **83**, 1–9 (2011).
172. Ulstrup, S. *et al.* Direct observation of minibands in twisted heterobilayers. (2019).
173. Schoenhense, G. *et al.* Momentum-Transfer Model of Valence-Band Photoelectron Diffraction. 1–24 (2018).
174. Winkelmann, A. *et al.* Momentum-resolved photoelectron interference in crystal surface barrier scattering. *Phys. Rev. B - Condens. Matter Mater. Phys.* **86**, 1–5 (2012).
175. Zaporozhchenko-Zymaková, A. *et al.* Momentum-resolved photoelectron absorption in surface barrier scattering on Ir(111) and graphene/Ir(111). *Phys. Rev. B* **96**, 1–7 (2017).
176. Pletikosić, I. *et al.* Dirac cones and minigaps for graphene on Ir(111). *Phys. Rev. Lett.* **102**, 1–4 (2009).
177. Bostwick, A. *et al.* Symmetry breaking in few layer graphene films. *New J. Phys.* **9**, (2007).
178. Moritz, W. *et al.* Structure determination of the coincidence phase of graphene on Ru(0001). *Phys. Rev. Lett.* **104**, 13–16 (2010).
179. Hämäläinen, S. K. *et al.* Structure and local variations of the graphene moiré on Ir(111). *Phys. Rev. B - Condens. Matter Mater. Phys.* **88**, 1–6 (2013).
180. Menteş, T. O., Zamborlini, G., Sala, A. & Locatelli, A. Cathode lens spectromicroscopy: Methodology and applications. *Beilstein J. Nanotechnol.* **5**, 1873–1886 (2014).
181. Wallbank, J. R., Fal'ko, V. & Mucha-Kruczynski, M. Moir´ e miniband features in the angle-resolved photoemission spectra of graphene/ h BN heterostructures. *Phys. Rev. B - Condens. Matter Mater. Phys.* **93**, 1–9 (2016).
182. Jin, C. *et al.* Observation of moiré excitons in WSe2/WS2 heterostructure superlattices. *Nature* **567**, 76–80 (2019).
183. Xie, S. *et al.* Direct observation of distinct minibands in moiré superlattices. *arXiv* **2**, 1–18 (2020).
184. Wang, Z. *et al.* Composite super-moiré lattices in double-aligned graphene heterostructures. *Sci. Adv.* **5**, eaay8897 (2019).
185. Laturia, A., Van de Put, M. L. & Vandenberghe, W. G. Dielectric properties of hexagonal boron nitride and transition metal dichalcogenides: from monolayer to bulk. *npj 2D Mater. Appl.* **2**, 6 (2018).
186. Weston, A. *et al.* Atomic reconstruction in twisted bilayers of transition metal dichalcogenides. *Nat. Nanotechnol.* **15**, 592–597 (2020).
187. Huang, B. *et al.* Layer-dependent ferromagnetism in a van der Waals crystal down to the monolayer limit. *Nature* **546**, 270–273 (2017).
188. Sivadas, N., Okamoto, S., Xu, X., Fennie, C. J. & Xiao, D. Stacking-Dependent Magnetism in Bilayer CrI 3. *Nano Lett.* **18**, 7658–7664 (2018).
189. Chen, W. *et al.* Direct observation of van der Waals stacking–dependent interlayer magnetism. *Science (80-.).* **366**, 983–987 (2019).
190. Zheng, F. *et al.* On the Quantum Spin Hall Gap of Monolayer 1T′-WTe $_2$. *Adv. Mater.* **28**, 4845–4851 (2016).
191. Song, Y. H. *et al.* Observation of Coulomb gap in the quantum spin Hall candidate single-layer 1T'-WTe2. *Nat. Commun.* **9**, 1–6 (2018).
192. Kane, C. L. & Mele, E. J. Quantum Spin hall effect in graphene. *Phys. Rev. Lett.* **95**, 1–4 (2005).
193. Hackl, R., Meissner, W. & Felix Baumberger, I. Laser ARPES investigation of the semi-metallic transition metal dichalcogenides WTe 2 and MoTe 2. (2016).

194. Eyers, A. *et al.* Characterization of symmetry properties of Pt(111) electron bands by means of angle-, energy-, and spin-resolved photoemission with circularly polarized synchrotron radiation. *Phys. Rev. Lett.* **52**, 1559–1562 (1984).
195. Schüler, M. *et al.* Local Berry curvature signatures in dichroic angle-resolved photoelectron spectroscopy from two-dimensional materials. *Sci. Adv.* **6**, eaay2730 (2020).
196. Xu, S. Y. *et al.* Electrically switchable Berry curvature dipole in the monolayer topological insulator WTe 2. *Nature Physics* vol. 14 900–906 (2018).
197. Zhang, Q. *et al.* Lifshitz Transitions Induced by Temperature and Surface Doping in Type-II Weyl Semimetal Candidate T $_d$ -WTe $_2$. *Phys. status solidi - Rapid Res. Lett.* **11**, 1700209 (2017).
198. Hoesch, M. *et al.* A facility for the analysis of the electronic structures of solids and their surfaces by synchrotron radiation photoelectron spectroscopy. *Rev. Sci. Instrum.* **88**, (2017).
199. May, A. F. *et al.* Ferromagnetism Near Room Temperature in the Cleavable van der Waals Crystal Fe 5 GeTe 2. *ACS Nano* **13**, 4436–4442 (2019).
200. Hwangbo, K. *et al.* Highly anisotropic excitons and multiple phonon bound states in a van der Waals antiferromagnetic insulator. *Nat. Nanotechnol.* 1–6 (2021) doi:10.1038/s41565-021-00873-9.
201. He, M. *et al.* Symmetry breaking in twisted double bilayer graphene. *Nat. Phys.* **17**, 26–30 (2021).
202. History of Synchrotron Radiation Sources. https://xdb.lbl.gov/Section2/Sec_2-2.html.
203. McKay, F. *et al.* Scalable growth and characterization of monolayer WSe$_{2}$. *Bull. Am. Phys. Soc.* **Volume 62**, **Number 4**, (2017).

APPENDIX – NOTES ON DFT

Linear scaling DFT calculations were performed for twisted $MoSe_2$-on-WSe_2 heterobilayers. The details for these calculations are reproduced with minor edits from the author's original work as listed in Chapter 2.

Misaligned (rotated) MX_2 layers form coincidence cells too large for the capabilities of plane-wave DFT. Instead, linear-scaling DFT was used to gain insight into the effects of hybridization on band edge energies for incommensurate structures. Full methodological details are below. We have previously shown that the energy landscape for twisted MX_2 heterostructures is roughly independent of twist angle, and similarly the hybridization induced shifts at Γ are consistent in magnitude. For this reason, we considered the angle which resulted in the smallest supercell size; a simulation cell containing 873 atoms (432 for WSe_2, 441 for $MoSe_2$) for layers rotated by 8.21°, with strain < 1% (in the $MoSe_2$ layer). To observe the band structure effects of each layer in the presence of the other, we have calculated the unfolded spectral function, which was projected selectively on each of the component layers.

Comparison between the band structures of the independent monolayers and the unfolded spectral-functions of the corresponding layers in the heterostructure shows low-spectral weight band intrusions from one monolayer into the other upon stacking. Moreover, the valence band maximum (VBM) at Γ of WSe_2 is raised by 202 meV, while the $MoSe_2$ VBM is lowered by 67 meV giving an increase in separation of ~ 250 meV. The experimental results show qualitatively similar behavior, with the bands shifting in the same direction and with a similar magnitude of increase in separation (experimentally ~ 100 meV) to the DFT predictions. Note that currently the linear scaling DFT approach adopted here does not include spin-orbit interactions – these are not expected to significantly alter the band structure at Γ but do change the band structure at K.

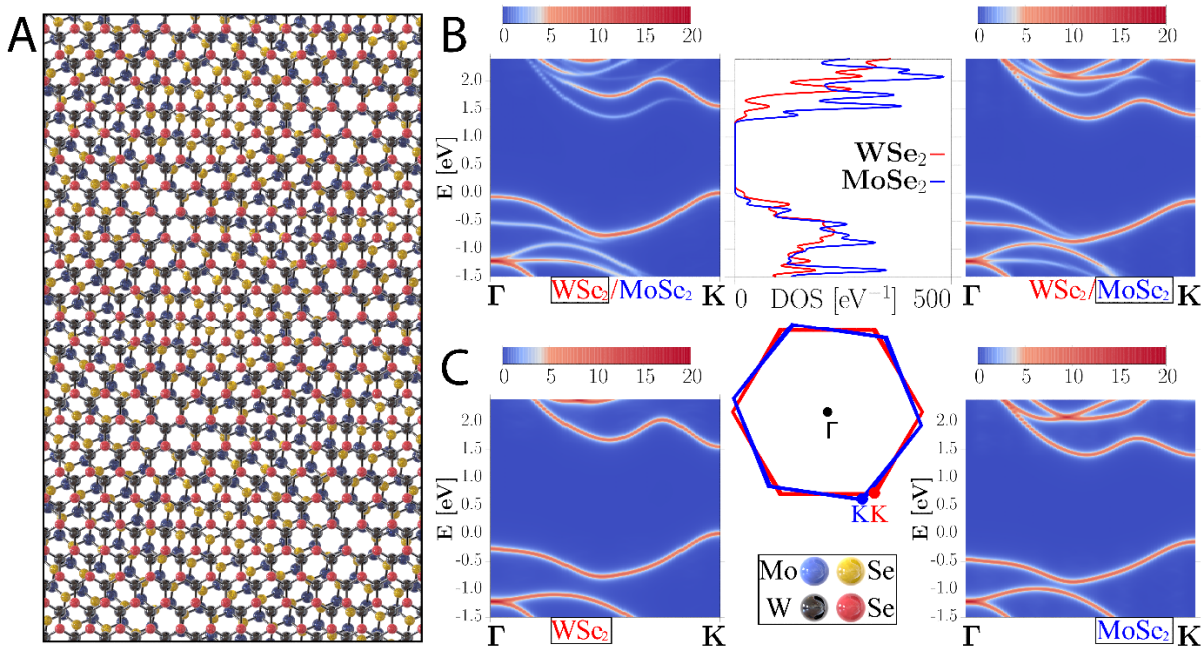

Linear-scaling DFT predictions of the band structure of the twisted $MoSe_2$-on-WSe_2 interface. A, Atomic model of $MoSe_2/WSe_2$ heterostructure with a twist angle of 8.21°. B, Unfolded spectral function of the twisted $MoSe_2/WSe_2$ heterostructure (A), projected on the WSe_2 monolayer (left) and $MoSe_2$ layer (right). The center inset shows the density of states (DoS) projected onto the WSe_2 and $MoSe_2$ layers from the heterointerface. C, The spectral-function representation of the independent monolayers for WSe_2 (left) and $MoSe_2$ (right). The color scales for B and C are arbitrary, and reflect the effective DoS per supercell as projected onto the reduced Brillouin zone of the respective monolayer. The energy reference is the energy of the valence band maximum (VBM) at K in the heterostructure.

Plane-wave DFT: for calculations involving individual materials and aligned heterostructures, the Quantum Espresso plane-wave DFT package was used. The ultrasoft atomic datasets of Garrity et al were used for structural calculations, and the optB88-vdW functional was employed, due to its previous success in describing interlayer interactions in 2D materials. The structures were optimized until forces were smaller than 10^{-4} Ry / Bohr for monolayers, and 5×10^{-4} Ry / Bohr for bilayers and bulk, while stresses were required to be smaller than 0.05 GPa. Subsequently, the band structures were calculated using the high-accuracy fully-relativistic PAW

potentials of Dal Corso, such that spin-orbit interaction was included. We used a 12x12 in-plane k-point sampling grid (with 4 out-of-plane k-points for the bulk), an 800 eV plane-wave energy cutoff, and an 8000 eV charge density cutoff. The simulation cell height was 30.0 Å, to avoid interaction between periodic images. All these parameters were determined to be sufficient for very good convergence of structural and electronic properties.

Linear-scaling DFT: we utilized the ONETEP code, which uses an efficiently-parallelized linear-scaling formalism based around representation of the single-electron density matrix via in-situ optimized local orbitals and sparse matrices. Once again we used the optB88-vdW functional and a kinetic-energy cutoff of 800 eV. ONETEP does not currently have the ability to include spin-orbit coupling, the projector-augmented wave (PAW) method was employed, with atomic datasets exactly equivalent to the ultra-soft pseudopotential (USPP) datasets used for the geometry optimizations in the plane-wave DFT calculations described above. The Mo and W atoms both contained 14 valence electrons ($4s^2,4p^6,4d^5,5s^1$ for Mo, $5s^2,5p^6,5d^4,6s^2$ for W), while S and Se contained only 6 valence electrons ($3s^2,3p^4$ for S, $4s^2,4p^4$ for Se).

ONETEP uses a nested-loop optimization scheme in which an outer loop optimizes the form of the local orbitals, while an inner loop optimizes the density matrix for fixed local orbitals. The flexibility provided by in-situ optimization means that it is possible to use relatively small number of local orbitals and retain systematically controllable accuracy equivalent to the plane-wave approach. In this case we used 13 non-orthogonal Wannier functions (NGWFs) for W and Mo (10 for the valence electrons, 3 allowing for additional polarization) and 9 for S and Se (4 for the valence electrons, 5 for additional variational freedom). All NGWFs were chosen to have a large cut-off radius (13.0 bohr), and the convergence criterion was that the root mean square of the NGWF gradient be smaller than 2×10^{-6}. For each NGWF optimization step, 8 self-consistent

density-kernel iterations were performed. Truncation of the density kernel was not necessary for the system sizes employed. Geometry optimization was performed by relaxing the internal atomic coordinates until the forces were below 0.1 eV / Å. The supercell was constructed by first determining the coincidence cells of the over-lapping rotated monolayers, allowing a maximum of 1% strain. Spectral functions were calculated by unfolding supercell eigenstates into the primitive cells of each layer, as described in previous work.

Electronic structure calculations including spin-orbit interaction from Chapter 3 were made using the Quantum Espresso DFT package[41]. Structures were first optimized until forces were smaller than 10^{-4} Ry / Bohr. Geometry optimizations and band structure calculations were performed with an 18×18 in-plane k-point grid with 140 Ry plane-wave energy cut off. To avoid interaction between periodic images, the vacuum spacing was 25.0 Å. We used norm-conserving fully relativistic pseudopotentials[42] from PseudoDojo[43], where the semi-core 4d, 5s and 5p states for W are retained as valence electrons. This results in a lattice constant of 3.32 Å for all three structures. We used the results from calculations with the PBE functional as a starting point for G_0W_0 calculations which utilized the Yambo code[44], with the Godby–Needs plasmon pole approximation[45]. We used 300 bands, 500 bands and 700 bands for the mono-layer, bilayer and trilayer WSe_2, respectively, for the self-energy and dynamical dielectric screening. In order to treat the divergence of the Coulomb interaction during the self-energy calculation, the random integration method[46] was used, with 3×10^6 random q-points and 100 random G vectors.

VITA

Paul was born in Seattle, Washington to Trong and Viet Nguyen, South Vietnamese immigrants who came to the US in 1990 through the Humanitarian Operation ('HO') subprogram of the United Nations High Commission for Refugees' Orderly Departure Program. There, they worked tirelessly, literally day and night, to support their diminutive son and shelter him from the new poverty they had found themselves in. Paul went through the Seattle Public School system's Spectrum, and Advanced Placement programs before applying (5 minutes past the deadline) at 16 to the Academy program of the University of Washington's Robinson Center. It was a golden, somehow sweltering early Spring day when he opened that bulky acceptance letter. It marked the beginning of a long career at the UW: first as an Acad 7.0 and Mary Gates Honors scholar; then as a 10-for-10 grad-program-rejected unpaid Bachelor researcher; and then as 10-for-10 grad-program-accepted doctoral student serving a brief seven-or-so year stint in the group of Prof. David H. "Hey, you" Cobden. Along the way he found a new name, lost a hat, killed a friend on stage a few times, studied abroad in Giessen, Germany, became a plumber, and wrote this thesis.